UNIVERSITY OF CALIFORNIA,
IRVINE

Nonlinear Rocket-Engine Longitudinal Combustion Instability

DISSERTATION

submitted in partial satisfaction of the requirements
for the degree of

DOCTOR OF PHILOSOPHY

in Mechanical and Aerospace Engineering

by

Tuan Minh Nguyen

Dissertation Committee:
Professor William A. Sirignano, Chair
Professor Said Elghobashi
Professor Derek Dunn-Rankin

2018

DEDICATION

To my parents and Tuyet Minh.

TABLE OF CONTENTS

LIST OF FIGURES

LIST OF TABLES

LIST OF ALGORITHMS

LIST OF SYMBOLS

Acronyms

CFD Computational Fluid Dynamics

CFPV Compressible Flamlet Progress Variable

CVRC Continuously Variable Resonance Combustor

DDES Delayed Detached Eddy Simulation

DES Detached Eddy Simulation

FPV Flamelet Progress Variable

HRR Heat Release Rate

LCM Laminar Closure Model

LEM Linear Eddy Mixing

LES Large Eddy Simulation

PDF Probability Density Function

RANS Reynolds-Averaged Navier-Stokes

Greek Symbols

χ Scalar Dissipation Rate

γ Specific heat coefficient ratio

λ Coefficient of thermal conductivity

μ Dynamic viscosity coefficient

ω Turbulence dissipation frequency

ϕ An arbitrary scalar

τ Viscous stress tensor

Roman Symbols

C	Progress Variable, upper case
c	Speed of sound, lower case
C_p	Specific heat coefficient at constant pressure
h	Total enthalpy
k	Turbulence kinetic energy
M	Mach number
P	Probability Density Function, upper case
p	Pressure,lower case
r	Radial vector
t	Time
u	Axial velocity
v	radial velocity
x	Axial/arbitrary spatial vector
Z''^2	Mixture fraction variance
E	Total energy
e	Total thermal energy
Pr	Prandtl number
Sc	Schmidt number
Z	Mixture Fraction

Superscripts

$\bar{}$	Reynolds averaged
$\tilde{}$	Density-weighted Favre averaged
R	Reynold quantity

Subscripts

f	Flamelet quantities
i	Radial indices

j	Axial indices
t	Turbulent quantity

Other Symbols

$\mathcal{F}$	Inviscid fluxes
$\mathcal{G}$	Viscous fluxes
$\mathcal{H}$	Divergence fluxes
$\mathcal{Q}$	Conserved variables
$\mathcal{S}$	Source terms
C_χ	Proportionality constant between turbulence and scalar time scales

ACKNOWLEDGMENTS

I would like to first and foremost thank my advisor, Professor William A. Sirignano, for his guidance and support through all these years. His drives for scientific research and work ethics are truly second to none, which inspire me to be a better student and researcher every day.

Dr. Pavel Popov of the University of Illinois at Urbana-Champaign, is appreciated for his guidance and advice as I was learning the rope in CFD.

I would also like to thank Professors Said Elghobashi and Derek Dunn-Rankin for taking part in my dissertation committee. Your valuable inputs have improved the quality of this dissertation.

I would like to express my gratitude to James Lewis and Rayomand Gundevia for their support and friendship through all of these trying years. I also want to acknowledge my labmates and friends in the department for all the unforgettable memories, especially during the 2015 Princeton summer school. You have made this arduous journey a lot more enjoyable.

I would like to thank my family, particularly my parents for their unconditional love and support. Even though they never get to finish high school, it is them who taught me the value of higher education. My most profound gratitude is to Tuyet Minh, as being with her always brighten my day. Without her love, none of this would be possible.

This research has been supported by the U.S. Air Force Office of Scientific Research under grant FA9550-15-1-0033, with Dr. Mitat Birkan as the Program Manager.

CURRICULUM VITAE

Tuan Minh Nguyen

EDUCATION

Doctor of Philosophy in Mechanical and Aerospace Engineering **2018**
University of California, Irvine *Irvine, CA*

Master of Science in Mechanical Engineering **2012**
Temple University *Philadelphia, PA*

Bachelor of Science in Mechanical and Aerospace Engineering **2010**
University at Buffalo, The State University of New York *Buffalo, NY*

RESEARCH EXPERIENCE

Graduate Research Assistant **2012–2018**
University of California, Irvine *Irvine, California*

Graduate Research Assistant **2011–2012**
Temple University *Philadelphia, PA*

Thesis: Modeling of the Thermo-mechanical Behaviors of
Nitinol Actuator for Smart Needle Application
Advisor: Professor Parsaoran Hutapea.

TEACHING EXPERIENCE

Teaching Assistant **2013–2017**
University of California, Irvine *Irvine, CA*

Teaching Assistant **2010–2012**
Temple University *Philadelphia, PA*

REFEREED JOURNAL PUBLICATIONS

Longitudinal Combustion Instability in a Rocket Engine with a Single Coaxial Injector **2018**
Journal of Propulsion and Power, Vol. 34, No. 2, pp. 354-373

The Impacts of Three Flamelet Burning Regimes in Nonlinear Combustion Dynamics **2018**
Combustion and Flame, Accepted

REFEREED CONFERENCE PUBLICATIONS

Driving Mechanisms of Liquid-Propellant Rocket Longitudinal Combustion Instability **Jan 2017**
55th AIAA Aerospace Sciences Meeting, Grapevine, Texas

Spontaneous and Triggered Longitudinal Combustion Instability in a Rocket Engine **July 2018**
54th, AIAA/SAE/ASEE Joint Propulsion Conference, Cincinnati, Ohio

ABSTRACT OF THE DISSERTATION

Nonlinear Rocket-Engine Longitudinal Combustion Instability

By

Tuan Minh Nguyen

Doctor of Philosophy in Mechanical and Aerospace Engineering

University of California, Irvine, 2018

Professor William A. Sirignano, Chair

With recent improvements in computer architecture, there are renewed interests in studying combustion instability in rocket engine via Computational Fluid Dynamics (CFD) simulations. Most existing numerical simulations are computationally expensive, with each simulation taking weeks to months to perform. The first objective of this dissertation is to develop a computationally inexpensive numerical solver. The solver, written in an axisymmetric formulation, is used to study longitudinal combustion instability in a single-injector rocket engine. For different stability domains, the results generated by the solver show good agreements with both experimental results and expensive 3D simulations. Compared to other axisymmetric solvers, the developed solver is at least an order of magnitude faster while using a more detailed chemical mechanism. Because of the canonical configuration of the rocket engine, fundamental understandings of the self-excited instability mechanisms under various stability domains are identified. Increasing the pressure oscillation leads to increase in mixing; making the flame inside the combustion chamber more compact. Pressure-Heat Release Rate coupling location plays a crucial role in driving the instability.

Subsequently, the flame dynamics under various oscillatory conditions are examined. Significant local extinctions and reignitions occur in the unstable cases compared to the stable cases. The complex chemical mechanism is proven to play an essential role in predicting

the correct oscillation amplitude. Partially premixed flames are found in the combustion chamber.

In the last chapter, for an unstable oscillation, wall heat loss and chamber modifications was found to provide stabilizing effects. The stabilized chamber is then triggered using different types of disturbances with various durations. In some cases, a limit cycle behavior with much larger pressure oscillations than the initial conditions is observed. This triggered instability of the longitudinal mode in this dissertation is a novel contribution to the field.

Chapter 1

Introduction

1.1 Combustion Instability Overview

Combustion instability is an acoustical phenomenon in which a propulsion system excites and sustains an unstable pressure oscillation. It is found in most major high-power propulsion systems that propel space shuttles, missiles, and airplanes. These systems have high energy release rate in volumes with relatively low losses, which in turn reinforce acoustical oscillations to very high amplitudes. In many cases, these oscillations can cause undesirable effects on thrust resulting in catastrophic failures.

In one form or another, combustion instability has been continuously studied since its discovery. The emphasis naturally has shifted depending on the systems that exhibit these behaviors. In the United States, elimination of high-frequency resonance burning (a term widely accepted in the past) in small tactical solid rocket engines was the primary research focus during World War II. Installations of baffles, resonance rods, or modifications of the geometry solved the problems.

During the development of the Apollo program in the 1960s, combustion instabilities found in the F1 liquid-propellant rockets became significant issues because of the astronauts on board the rockets. Similar to the solution for solid rockets, installations of baffles stabilized the engine. A comprehensive compilation of the F1 engine combustion instabilities can be found in [1].

Combustion instabilities have also been found in jet-engine afterburners [2]. These systems exhibit high-frequency transverse modes similar to oscillations found in liquid rockets. With the modifications of geometry, especially the development of high bypass engines, these transverse modes are replaced by lower frequency longitudinal vibrations. Transverse combustion instabilities found in liquid-fueled ramjets were minimized by more compact designs, which in turn causes longitudinal oscillations with lower frequencies.

Longitudinal instability, for specific designs, has much lower oscillation frequencies than its transverse counterpart. However, the installation of baffles cannot eliminate the problem. Therefore, this study seek to understand the mechanisms of longitudinal combustion instability and explore different stabilizing effects. The outline for subsequent sections of this is as followed. Preliminary concepts are first described. A literature review, specifically on liquid rocket engines, is presented. Objectives of this dissertation are then given.

1.2 Preliminary concepts

Culick [3] noted two types of acoustical combustion instability: driven and self-excited. Driven combustion instability is found mostly in the solid-propellant rocket engine. The instability occurs in which vortex shedding drives kinematic waves of vorticity or entropy to some point of acoustical reflection. The reflected wave then, in turn, causes more noise (vortex shedding). These instabilities have smaller amplitude compared to the self-excited

type. Self-excited instabilities, on the other hand, are not limited by the energy of initiation; and can be found mostly in liquid-propellant rockets. Two types of self-excited instabilities can occur: linear and nonlinear behavior. Linear behavior refers to spontaneous instability. In this case, an oscillation is excited and grows to unstable high amplitude from normal noise level. Nonlinear behavior refers to any instabilities triggered by unusual conditions such as irregular flow rates, or large acoustic disturbances. These disturbances need to have sufficient magnitude to overcome the required threshold [4]. While the classifications refer to two different kinds of instabilities, both exhibit nonlinear behaviors once they are excited.

Another essential concept is the stable and unstable limit cycle. Based on perturbation theory, an unstable limit cycle provides a threshold (disturbance magnitude) below which the initial disturbance decays with time [5]. On the other hand, if the initial disturbance is above the unstable limit cycle, it will grow to a stable limit cycle. Figure 1.1 illustrates the concept of limit cycle behavior. In all of these cases, the initial pressure is marked at the point (0,200). In figure 1.1a, when the disturbance is small enough, the pressure returns to its initial pressure (yellow circle in the middle). However, if the disturbance is large enough, the pressure reaches a stable limit cycle with peak-to-peak amplitude comparable to the initial pressure. Additionally, figure 1.1(b) shows an unconditionally unstable system in which any disturbance will grow to a limit cycle. Figure 1.1(c) shows an unconditionally stable system in which any disturbance regardless of magnitude will decay with time. Therefore, a non-linear analysis of combustion instabilities should address two issues: conditions for the existence & stability of the limit cycles, and the conditions in which a linearly stable system become unstable (triggering).

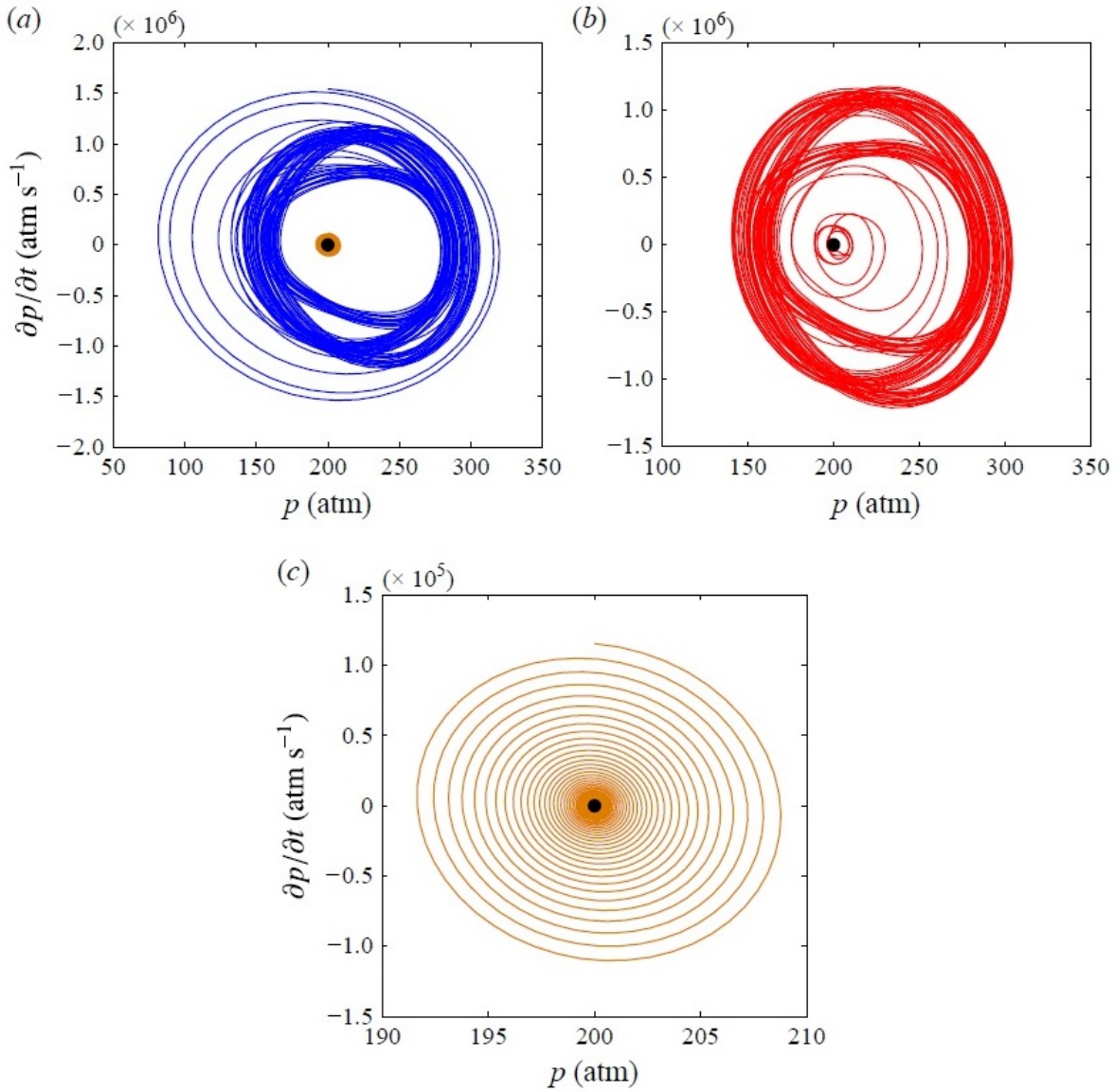

Figure 1.1: Phase plot of pressure disturbance vs initial pressure for (a) unstable limit cycle behavior,(b) unconditionally unstable and (c) unconditionally stable [6]

1.3 Literature Review

1.3.1 Early Analytical and Numerical Research

In the 1950s and 1960s, linear behaviors received significant attention. A comprehensive compilation of works edited by Harrje and Reardon [7] provide a complete picture into the early 1970s. Prominent theoretical work on longitudinal mode was addressed by Crocco and Cheng [8, 9]. These works laid the foundations to describe the combustion response and reinforcement of acoustic oscillations within liquid propellant rocket engine using sensitive time lag theory. The two parameters (n,τ) were introduced where n is the pressure index of interaction and τ represents the pressure sensitivity to the time lag [8]. The authors determined that for a specific discrete range of values of τ at a particular natural frequency (mode), a system becomes unstable if it has an n value that is greater than a specified minimum limit. Based on this conclusion, the effect of longitudinal oscillations on mass, momentum, and energy exchanged between phases were established. The authors also demonstrated the independence of the two parameters n and τ from the oscillation frequency, and thus concluded that a detailed description of the unsteady combustion process can be avoided.

Another major research area during this period is to study the wave dynamics within the combustion chamber. Reardon et al. [10] and Crocco and Sirignano [11], as a continuation of Tsien's work on the acoustical reflection in the nozzle [12], extended the analysis to a 3D linear oscillation in the nozzle. Sirignano [13] was the first to show that longitudinal combustion instabilities exhibit unstable and stable limits cycle oscillations (as explained in the section above). Sirignano and Crocco [5] extended this theory to include shock wave formation. These early theoretical predictions of triggering instabilities, however, did not predict the stable limit cycle having higher amplitude than the unstable limit cycle. This oversight could be corrected if the analysis of the amplitude parameters were extended beyond the third-order terms [4]. Mitchell et al. [14] later improved the analysis for longitudinal modes

to predict both the unstable and stable limit cycles. The theoretical prediction was then extended for the transverse mode by Zinn [15], and for both transverse and longitudinal modes by Crocco and Mitchell [16]. While these early research revealed significant characteristics of the nonlinear combustion instability, due to the complexity of their mathematical analysis, their applications in numerical simulations were very limited. Zinn and Powell [17], while still using n and τ for limit cycle analysis, introduced the modified Galerkin method into their work. Based on the technique, they were able to reduce the governing equations into ordinary differential equations (ODEs) that can be numerically simulated. Therefore, transient behavior of the process can be captured. However, Galerkin's solution depends heavily on the chosen sets of fundamental equations, which can only satisfy simple boundary conditions. The solutions obtained by Galerkin's method, therefore, can only be used for some particular situations. It is a well-established concept that the environment within the combustion chamber has infinite degrees of freedom. However, the chamber boundary conditions only allow solutions at discrete modal frequencies [2]. Based on this principle, Awad and Culick [18], Yang et al. [19] and Culick [3, 20] utilized the technique of eigenfunction expansion to reduce the governing equations to a set of nonlinear ODEs. Both methods described above require prior knowledge of the relevant modes of oscillation, which encounters significant difficulties when complex systems are concerned.

There are several operating conditions of propellants in liquid rockets: sub-critical, trans-critical and super-critical. Over the past few decades, the driving mechanism of combustion instability for sub-critical and trans-critical operating conditions were extensively studied [21–26]. In these conditions, propellants can exist both as liquids and gas at different points of the flow. Tong and Sirignano [25] examined the effects of oscillating gas pressure and velocity on droplet vaporization rates during combustion instabilities. The authors found that when droplet vaporization is the controlling phenomenon, acoustic oscillation in the combustion chamber can be sustained. Delplanque and Sirignano [26] studied the response of a liquid oxygen droplet to oscillatory ambient conditions over a wide range of frequencies.

They concluded that droplets under gasification process could drive combustion instabilities in the longitudinal mode under some simplifying assumptions. On the other hand, in super-critical conditions, propellants no longer have the distinct phases, which presents different physical phenomenon.

1.3.2 Experimental Research

The experimental investigations also play vital roles in understanding physical phenomena of combustion instabilities. From full-scale testing during the development of F1 engines [1], to sub-scaled systems [27, 28], combustion instability in the liquid-rocket engine has been extensively studied. However, few experiments were conducted with computational verification in mind. A series of longitudinal combustion instability experiments conducted at Purdue University provides beneficial information for numerical simulation [29–32]. By only testing a model combustion chamber with a single injector, these experiments provide the ability to capture detailed measurements of the mixing and reactions occurring in the injector flow field. Moreover, careful injector-combustion chamber acoustical design was taken into consideration so that the system can sustain and amplify any resulting small pressure disturbance (rumbling noise) [29].

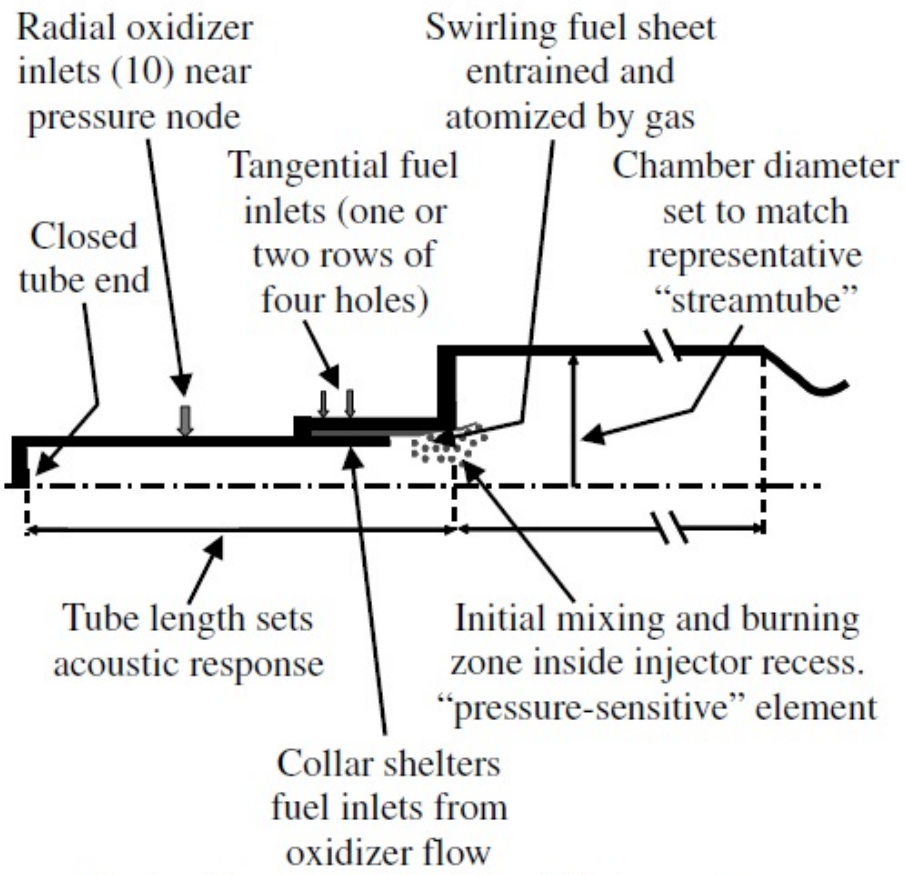

Figure 1.2: Experimental configuration for single-swirl-injector experiments conducted at Purdue University [29]

There are two iterations or series of experiments. In the first iteration shown in figure 1.2, liquid JP-8 fuel was injected through swirl injectors. Oxidizer was decomposed hydrogen peroxide. The gaseous oxidizer consisted of 42% oxygen and 58% water vapor by weight with a temperature of 1029K. There were ten experiments conducted in this series. The authors studied different lengths of the combustion chamber. The chamber length was varied discretely from 25.4 cm to 88.9 cm. The shortest length of the chamber (25.4 cm) behaved unconditionally stable. The remaining chamber length exhibits unstable behaviors with pressure oscillation frequencies varies from 1184 to 1721 Hz for the first chamber mode. These experiments served as as good test cases for numerical simulations of combustion

instability because no external forcing functions are required to trigger instability.

Smith et al. [33] studied the effect of back-step height on the combustion instability based on the unconditionally stable case. However, due to the difficulties associated with modeling the JP-8 liquid fuel, the computations had to use gaseous kerosene as a substitute. Additionally, the author had to neglect the vaporizations and atomizations of the droplets, which are essential in the combustion dynamics [23]. Therefore, the experimental and computations results are not in good agreement.

Several modifications were made in the second iteration of these experiments to make the results more computational friendly [32].

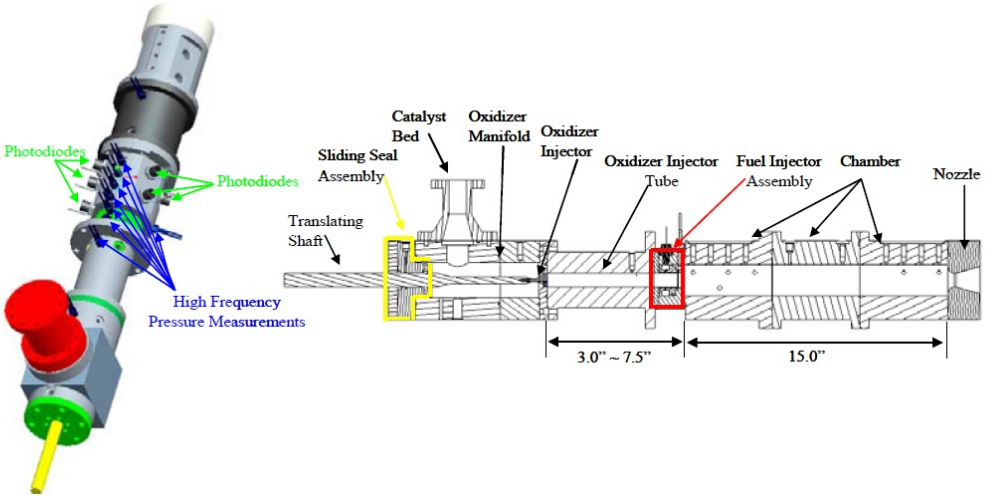

Figure 1.3: Experimental configuration for the second iteration of single-injector experiments conducted at Purdue University [31]

The oxidizer used in these experiments are the same as the previous iteration. Three fuels were initially considered: methane, hydrogen, and ethylene [30]. Methane was subsequently chosen as the main fuel [32]. The fuel is now injected axially, thus, minimizing the difficulties associated with modeling the swirling injection. The chamber was kept at a constant length of 40 cm (including the nozzle) while the oxidizer injector post length was varied. The experiments in this iteration is called Continuously Variable Resonance Combustor (CVRC).

The longest injector length (19 cm) was found to be stable but under the bifurcation condition. The medium injector length (14 cm) was the most unstable while the shortest injector length (9 cm) was marginally stable. In the most unstable case (14-cm oxidizer post), the experimental mean chamber pressure is roughly 14 MPa with a peak-to-peak amplitude of 7 atm. The fuel injection temperature is 300 K. The oxidizer inlet temperature is 1030 K. Therefore, the thermodynamic properties of most reactants are above the critical values except for hydrogen, as shown in table 1.1. However, Huo and Yang [34] showed that, for supercritical combustion of oxygen/hydrogen mixtures, the ideal-gas-law assumption has a negligible effect on the flame structure. Therefore, difficulties regarding modeling transcritical and supercritical propellants are minimized. The CVRC experiments serve as the basis for this dissertation.

Table 1.1: Critical properties of different reactants

Reactants	T_{cr} (K)	P_{cr} (atm)
CH_4	190.6	45.6
O_2	154.6	49.8
H_2	33.2	12.8
H_2O	647	217.75
CO_2	304.18	72.83
CO	134.45	34.98

1.3.3 Computational Research

With recent advancements in computer architectures, there are renewed interests in studying both transverse and longitudinal combustion instability via high-fidelity numerical simulations. The literature on these works is abundant [35–38]. For brevity purposes, the following literature review only concentrates on the CVRC computational results. Srinivasan et al.

[39] studied flame dynamics of different stability domains using a LES turbulence model coupled with the Linear Eddy Mixing (LEM) model. Comparing different oxidizer post lengths, the authors found different stability domains that are consistent with the experiments. They concluded that acoustic interactions with the flow field lead to subtle changes in the vorticity (and mixing dynamics) between these cases. Premixed and non-premixed burnings are found to coexist within the chamber. Garby et al. [40] studied both axisymmetric and fully 3D flame stabilization mechanism for the 12-cm oxidizer post using a LES method coupled with a Dynamic Flame Thickened (DFT) chemistry model. They demonstrated that while the axisymmetric flame simulation qualitatively captures the unstable behavior, it underpredicts the oscillation magnitudes compared to both 3D and experimental results. Harvazinski et al. [41] studied the effects of grid resolution and dimensionality on the ability to predict combustion instability using both axisymmetric and 3D simulations using Detached Eddy Simulations (DES) with Laminar Closure Model (LCM) for chemistry. They performed three different simulations: one 3D and two axisymmetric with two different grid sizes. Similar to Garby et al., the 3D results match the experimental data very well. However, their axisymmetric simulations under-predict the oscillation magnitudes by $50\% - 60\%$. Harvazinski et al. [42] performed 3D simulations using a detailed chemistry mechanism (GRI-Mech 1.2). The same oscillation magnitudes were observed compared to 3D calculations with global chemistry mechanisms. On the other hand, Sardeshmukh et al. [43] showed that by using the same detailed chemical mechanism as Harvazinski et al. (GRI-Mech 1.2), their DES axisymmetric simulation could capture much larger oscillation amplitude ($80\% - 90\%$ of the experimental results) compared to axisymmetric calculations using global mechanisms. In all studies, the simulations over-predicted the oscillations frequency. All of the authors postulated that by using the adiabatic wall boundary condition, the flames in these simulations are hotter compared to the experiments, thus leading to a rise in mean chamber pressure and the speed of sound. A common conclusion among these works is that to predict the oscillation amplitude correctly, either 3D simulations with simplified chemical mechanisms

or axisymmetric calculations with detailed chemistry must be used. Therefore, the associated computational costs in these works are prohibitively expensive. Extensive parametric studies using these solvers are, thus, not feasible.

1.3.4 Research Objectives

Based on the literature survey, the first objective of this dissertation is to develop a new high-fidelity computationally inexpensive solver. The new solver has the following details:

1. The new solver is written in an axisymmetric compressible formulation. As shown by Garby et al. [40], the axisymmetric flame length is significantly longer than the 3D results due to the effect of imposing the zero-gradient turbulent boundary condition on the axis of symmetry. The lack of vortex stretching and tilting in axisymmetric calculations also means turbulence structures generated by axisymmetric simulations are different than those of 3D simulations. These effects lead to different mixing and burning characteristics between the axisymmetric and the 3D calculations. However, as shown in various calculations [39, 40], the primary instability characteristics of the CVRC experiments occur in the longitudinal direction. Therefore, the neglect of the third direction with regard to capturing the wave dynamics is justified.

2. A hybrid RAN/LES model is used. As shown in various axisymmetric calculations of the CVRC experiments [43, 44], the DES turbulence model can qualitatively capture the correct physics. Near a wall, the model behaves the same as a RANS model. Far away from the wall, the turbulent viscosity values decrease significantly compared to a traditional RANS model, allowing it to behave as a sub-grid model just like LES [45]. The RANS feature of DES alleviates the main difficulty associated with LES, where either a wall model or extremely fine grids must be used near the walls. DES is, therefore, a less expensive treatment of turbulence compared to LES.

3. Because of the axisymmetric formulation of the solver, detailed chemical mechanisms must be used to capture the correct instability behavior. The flamelet approach is chosen in this work. First introduced by Peters [46], it assumes that the chemical time scales are shorter than the turbulence time scales in the energy-containing eddies so the flame can be approximated as one-dimensional. Therefore, turbulent flames are collections of laminar flame elements embedded in and interacting with the turbulent flow field. Because of these assumptions, the flame is uncoupled from the turbulent flow field and solved independently of the primary CFD calculations. Detailed chemical mechanisms, thus, can be incorporated while retaining low computational cost. The current solver implements a flamelet model called the Compressible Flamelet Progress Variable (CFPV).

The developed solver computational results are used to benchmark against both experimental and numerical results in chapter 3. In chapter 4, the major instability mechanisms in the CVRC experiments are identified. In chapter 5, flame dynamics under different instability domains are examined. Chapter 6 explores the effects of wall heat loss and geometric modifications on the instability as well as the possibility of triggering. Finally, chapter 7 present a summary and major conclusions of this work.

Chapter 2

Computational Framework

The governing equations presented below are written in axisymmetric form. Similar to most turbulent combustion solvers, all variables are Favre-averaged (˜superscript). The density and pressure are Reynolds-averaged (¯ superscript) For convenience in expressing the numerical scheme in sections 2.1, 2.2.1, 2.3.2, any equations presented below can be written in vector form as follows

$$\frac{\partial \mathcal{Q}}{\partial t} + \frac{\partial \mathcal{F}_x}{\partial x} + \frac{\partial \mathcal{F}_r}{\partial r} + \frac{\mathcal{H}^I}{r} = \frac{\partial \mathcal{G}_x}{\partial x} + \frac{\partial \mathcal{G}_r}{\partial r} + \frac{\mathcal{H}^V}{r} + \mathcal{S} \tag{2.1}$$

where $\mathcal{Q}$ is the vector of conserved variables. $\mathcal{F}_x$, $\mathcal{F}_r$ are the inviscid mass fluxes in the x and r directions, respectively. Similarly, $\mathcal{G}_x$, $\mathcal{G}_r$ are the viscous mass fluxes in the x and r directions. $\mathcal{H}^I$, $\mathcal{G}^V$ are the inviscid, and viscous divergence terms that arise from the axisymmetric assumption. $\mathcal{S}$ is the source term.

2.1 Governing Equations

In this section, the Navier-Stokes equations are presented. The conserved variables for the main flow equations are

$$\mathcal{Q} = (\bar{\rho}, \bar{\rho}\tilde{u}, \bar{\rho}\tilde{v}, \bar{\rho}\tilde{E})^T \tag{2.2}$$

where $\bar{\rho}, \tilde{u}, \tilde{v}, \tilde{E}$ are the density, axial & radial velocities, and total energy per unit mass, respectively. The total energy is defined as the summation of the kinetic and thermal energies of all the species

$$\tilde{E} = \frac{1}{2}\left(\tilde{u}^2 + \tilde{v}^2\right) + k + \tilde{e} \tag{2.3}$$

where k is the turbulence kinetic energy and $\tilde{e}$ is the total thermal energy.

The inviscid fluxes and divergence terms are defined as

$$\mathcal{F}_x = \begin{pmatrix} \bar{\rho}\tilde{u} \\ \bar{\rho}\tilde{u}\tilde{u} + \bar{p} \\ \bar{\rho}\tilde{u}\tilde{v} \\ (\bar{\rho}\tilde{E} + \bar{p})\tilde{u} \end{pmatrix}, \qquad \mathcal{F}_r = \begin{pmatrix} \bar{\rho}\tilde{v} \\ \bar{\rho}\tilde{u}\tilde{v} \\ \bar{\rho}\tilde{v}\tilde{v} + \bar{p} \\ (\bar{\rho}\tilde{E} + \bar{p})\tilde{v} \end{pmatrix}, \qquad \mathcal{H}^I = \begin{pmatrix} \bar{\rho}\tilde{v} \\ \bar{\rho}\tilde{v}\tilde{u} \\ \bar{\rho}\tilde{v}\tilde{v} \\ (\bar{\rho}\tilde{E} + \bar{p})\tilde{v} \end{pmatrix} \tag{2.4}$$

where $\bar{p}$ is the Favre-Averaged pressure.

Similarly, the viscous fluxes and their corresponding divergence terms are

$$\mathcal{G}_x = \begin{pmatrix} 0 \\ \tau_{xx}^m + \tau_{xx}^R \\ \tau_{rx}^m + \tau_{rx}^R \\ \tilde{u}(\tau_{xx}^m + \tau_{xx}^R) + \tilde{v}(\tau_{rx}^m + \tau_{rx}^R) + q_x + q_{x,k} \end{pmatrix}, \quad \mathcal{G}_r = \begin{pmatrix} 0 \\ \tau_{rx}^m + \tau_{rx}^R \\ \tau_{rr}^m + \tau_{rr}^R \\ \tilde{u}(\tau_{rx}^m + \tau_{rx}^R) + \tilde{v}(\tau_{rr}^m + \tau_{rr}^R) + q_r + q_{r,k} \end{pmatrix},$$

$$\mathcal{H}^V = \begin{pmatrix} 0 \\ \tau_{rx}^m + \tau_{rx}^R \\ (\tau_{rr}^m + \tau_{rr}^R) - (\tau_{\theta\theta}^m + \tau_{\theta\theta}^R) \\ \tilde{u}(\tau_{rx}^m + \tau_{rx}^R) + \tilde{v}(\tau_{rr}^m + \tau_{rr}^R) + q_r + q_{r,k} \end{pmatrix} \tag{2.5}$$

where $q_{x,k}, q_{r,k}$ are the top terms of axial ($\mathcal{G}_x$) and radial ($\mathcal{G}_r$) viscous fluxes in equation 2.10. In equation 2.5, q_x, q_r are the heat fluxes defined as follows

$$q_x = \left(\frac{\lambda}{C_p} + \frac{\mu_t}{Pr_t}\right)\frac{\partial \tilde{h}}{\partial x}, \qquad q_r = \left(\frac{\lambda}{C_p} + \frac{\mu_t}{Pr_t}\right)\frac{\partial \tilde{h}}{\partial r} \tag{2.6}$$

where λ is the heat conduction coefficient and C_p is the constant specific heat. μ_t is the turbulent viscosity. Pr_t is the turbulent Prandtl number, which has a constant value of 0.9 in this dissertation.

Using Stokes hypothesis, the total viscous stress tensors, which include both the molecular

(τ_{ij}^m) and Reynolds (τ_{ij}^R) stresses, are

$$\begin{aligned}
\tau_{xx}^m + \tau_{xx}^R &= \left(\mu + \mu_t\right)\left[\frac{4}{3}\frac{\partial \tilde{u}}{\partial x} - \frac{2}{3}\left(\frac{\tilde{v}}{r} + \frac{\partial \tilde{v}}{\partial r}\right)\right] - \frac{2}{3}\bar{\rho}k \\
\tau_{rx}^m + \tau_{rx}^R &= \left(\mu + \mu_t\right)\left[\frac{\partial \tilde{u}}{\partial r} + \frac{\partial \tilde{v}}{\partial x}\right] \\
\tau_{rr}^m + \tau_{rr}^R &= \left(\mu + \mu_t\right)\left[\frac{4}{3}\frac{\partial \tilde{v}}{\partial r} - \frac{2}{3}\left(\frac{\tilde{v}}{r} + \frac{\partial \tilde{u}}{\partial x}\right)\right] - \frac{2}{3}\bar{\rho}k \\
\tau_{\theta\theta}^m + \tau_{\theta\theta}^R &= \left(\mu + \mu_t\right)\left[\frac{4}{3}\frac{\tilde{v}}{r} - \frac{2}{3}\left(\frac{\partial \tilde{v}}{\partial r} + \frac{\partial \tilde{u}}{\partial x}\right)\right] - \frac{2}{3}
\end{aligned} \tag{2.7}$$

where μ is the molecular viscosity. The source term ($\mathcal{S}$) is 0 for the main flow equation.

2.2 Turbulence Model

2.2.1 RANS model

The first turbulence model considered in this dissertation is the 2006 two-equation Wilcox k-ω model, where k is the turbulence kinetic energy and ω is the inverse time scale of the large scale motion. The conserved scalars are in these equations are

$$\mathcal{Q} = (\bar{\rho}k, \bar{\rho}\omega)^T \tag{2.8}$$

The inviscid fluxes and divergence terms are defined as

$$\mathcal{F}_x = \begin{pmatrix} \bar{\rho}\tilde{u}k \\ \bar{\rho}\tilde{u}\omega \end{pmatrix}, \qquad \mathcal{F}_r = \begin{pmatrix} \bar{\rho}\tilde{v}k \\ \bar{\rho}\tilde{v}\omega \end{pmatrix}, \qquad \mathcal{H}^I = \begin{pmatrix} \bar{\rho}\tilde{v}k \\ \bar{\rho}\tilde{v}\omega \end{pmatrix} \tag{2.9}$$

The viscous fluxes and their corresponding divergence terms are

$$\mathcal{G}_x = \begin{pmatrix} \left(\mu + \sigma_k \frac{\bar{\rho}k}{\omega}\right)\frac{\partial k}{\partial x} \\ \left(\mu + \sigma_\omega \frac{\bar{\rho}k}{\omega}\right)\frac{\partial \omega}{\partial x} \end{pmatrix}, \quad \mathcal{G}_r = \begin{pmatrix} \left(\mu + \sigma_k \frac{\bar{\rho}k}{\omega}\right)\frac{\partial k}{\partial r} \\ \left(\mu + \sigma_\omega \frac{\bar{\rho}k}{\omega}\right)\frac{\partial \omega}{\partial r} \end{pmatrix}, \mathcal{H}^V = \begin{pmatrix} \left(\mu + \sigma_k \frac{\bar{\rho}k}{\omega}\right)\frac{\partial k}{\partial r} \\ \left(\mu + \sigma_\omega \frac{\bar{\rho}k}{\omega}\right)\frac{\partial \omega}{\partial r} \end{pmatrix} \tag{2.10}$$

The source terms are

$$\mathcal{S} = \begin{pmatrix} P_k - \beta^* \bar{\rho}\omega k \\ \frac{\gamma\omega}{k}P_k - \beta\bar{\rho}\omega^2 + \frac{\bar{\rho}\sigma_d}{\omega}\left[\frac{\partial k}{\partial x}\frac{\partial \omega}{\partial x} + \frac{\partial k}{\partial r}\frac{\partial \omega}{\partial r}\right] \end{pmatrix} \tag{2.11}$$

where P_k is the production rate of the turbulent kinetic energy

$$P_k = \tau_{xx}\frac{\partial \tilde{u}}{\partial x} + \tau_{rr}\frac{\partial \tilde{v}}{\partial r} + \tau_{rx}\left(\frac{\partial \tilde{u}}{\partial x} + \frac{\partial \tilde{v}}{\partial r}\right) + \tau_{\theta\theta}\frac{\tilde{v}}{r} \tag{2.12}$$

A less nonlinear form of equation 2.12, as derived by Liu and Zheng [47], is implemented in the solver. The turbulent viscosity is

$$\mu_t = \frac{\bar{\rho}k}{\tilde{\omega}} \tag{2.13}$$

where

$$\tilde{\omega} = \max\left(\omega, C_{lim}\sqrt{\frac{2\bar{S}_{ij}\bar{S}_{ij}}{\beta^*}}\right), \quad \bar{S}_{ij} = S_{ij} - \frac{1}{3}\frac{\partial \tilde{u}_k}{\partial x_k}\delta_{ij}, \quad S_{ij} = \frac{1}{2}\left(\frac{\partial u_i}{\partial x_j} + \frac{\partial u_j}{\partial x_i}\right) \tag{2.14}$$

where S_{ij} is the mean strain-rate tensor. For an axisymmetric flow, the zero-trace mean strain-rate tensor ($\bar{S}_{ij}$) has the form of

$$\bar{S}_{ij} = \begin{bmatrix} \frac{1}{3}(2\frac{\partial \tilde{v}}{\partial r} - (\frac{\tilde{v}}{r} + \frac{\partial \tilde{u}}{\partial x})) & 0 & \frac{1}{2}(\frac{\partial \tilde{v}}{\partial x} + \frac{\partial \tilde{u}}{\partial r}) \\ 0 & \frac{1}{3}(2\frac{\tilde{v}}{r} - (\frac{\partial \tilde{v}}{\partial r} + \frac{\partial \tilde{u}}{\partial x})) & 0 \\ \frac{1}{2}(\frac{\partial \tilde{v}}{\partial x} + \frac{\partial \tilde{u}}{\partial r}) & 0 & \frac{1}{3}(2\frac{\partial \tilde{u}}{\partial x} - (\frac{\partial \tilde{v}}{\partial r} + \frac{\tilde{v}}{r})) \end{bmatrix} \tag{2.15}$$

Finally, the modeling constants are given in table 2.1.

Table 2.1: Turbulence Modeling Constants.

γ	β^*	β	σ_k	σ_ω	C_{lim}
0.52	0.09	0.0708	0.6	0.5	0.875

with

$$\sigma_d = \begin{cases} 0, & \text{if } \frac{\partial k}{\partial x_j}\frac{\partial \omega}{\partial x_j} \leq 0 \\ \frac{1}{8}, & \text{if } \frac{\partial k}{\partial x_j}\frac{\partial \omega}{\partial x_j} > 0 \end{cases} \tag{2.16}$$

2.2.2 Delayed Detached Eddy Simulation

As shown in Appendix A, the RANS model cannot be used to predict the instability that occurs in the CVRC experiment. Therefore, a second approach is considered in this work. The approach is called the Detached Eddy Simulation (DES), first proposed by Spalart et al. [45] for the one-equation Spalart-Allmaras turbulence model. Strelets [48] expanded the concept to Menter's Shear Stress Transport (SST) k-ω model. In the DES approach, the transport equations of both k and ω are still solved. However, the dissipation term in the k equation is modified so that the computed turbulent viscosity does not capture any grid-resolved turbulent scales. Thus, the DES method acts as a hybrid RANS/LES approach that incorporates aspects of both turbulence models. The dissipation term in equation 2.11 (the second term) is replaced by using the following mathematical definition

$$\frac{\bar{\rho}k^{3/2}}{L_T^*} \simeq \beta^* \bar{\rho}\omega k \tag{2.17}$$

The corrected turbulent length scale is defined as

$$L_T^* = min(L_T, C_{DES} L_{GRID}) \tag{2.18}$$

where C_{DES} is a modeling constant. L_T and L_{GRID} are the turbulent and grid length scales

$$L_T = \frac{k^{1/2}}{(\beta^* \omega)}, \qquad L_{GRID} = L_T - F_D(L_T - \Delta) \tag{2.19}$$

where Δ is the largest grid dimension for the cell. In the traditional DES approach, F_D has a value of unity, This formulation creates grid arbitrariness because the smallest grid sizes of the mixing shear layer and of the walls are the same in the current computational setup. Therefore, to further limit this issue, F_D is defined as [49]

$$F_D = 1 - tanh\left[\left(1.5\frac{L_T}{d}\right)^3\right] \tag{2.20}$$

where d is the distance away from any wall. This approach is called Delayed Detached Eddy Simulation (DDES) and used for all the simulations in this work.

2.3 Combustion Model

In most turbulent combustion applications, the finite-rate chemistry models are used. These approaches solve the Filtered/Favre-averaged species transport equations such as 2.21

$$\frac{\partial \bar{\rho} \tilde{Y}_L}{\partial t} + \frac{\partial \bar{\rho} \tilde{v}_j \tilde{Y}_L}{\partial x_j} = \frac{\partial}{\partial x_j}\left[\bar{\rho} \mathcal{D}_L \frac{\partial \tilde{Y}_L}{\partial x_j}\right] + \tilde{\dot{\omega}}_L \tag{2.21}$$

where Y_l and $\mathcal{D}_L$ are the mass fraction and mass diffusivity of species L. The mass reaction rate per unit volume ($\tilde{\dot{\omega}}_L$) requires a closure model. Different approaches have been taken to address this problem. In the simplest approach called Laminar Closure Model (LCM),

which solves the Arrhenius law as

$$\tilde{\dot{\omega}}_L = A\tilde{T}^b exp\bigg(- \frac{E_a}{R\tilde{T}}\bigg)\tilde{X}_f^m \tilde{X}_o^n \tag{2.22}$$

where $\tilde{X}_f$ and $\tilde{X}_o$ are the filtered mole fractions of the fuel and oxidizer, respectively. The approach is widely used in the CVRC computational solver by Harvazinski et al. [41], Sardeshmukh et al. [43]. This model introduces major errors because the reaction rates are obtained using the mean instead of the instantaneous quantities. In the Eddy Dissipation Model [50], the reaction source terms are calculated based on turbulence quantities and different constants. In the Thickened Flame Model approach, the flames are artificially thickened to be resolved on the numerical grids by multiplying the diffusion and dividing the reaction terms of equation 2.21 by a thickening factor [51, 52]. Another approach is the Linear Eddy Mixing (LEM) model [35, 39], in which the relevant advection-diffusion-reaction couplings are resolved using a low-dimensional representation of turbulent advection. As the number of the chemical species increases, the solutions to their transport equations are required. Therefore, in these models, incorporating any realistic detailed-chemical mechanism involving tens of species and hundreds of reactions presents a difficult challenge due to the enormous computational cost. Additionally, the nonlinearity of species reaction source terms due to Arrhenius law (equation 2.22) and the wide range of chemical time scales associated with these schemes make the resulting species transport equations very stiff and difficult to solve. Therefore, most of these models are limited to either one- or two-step chemical mechanisms involving 4-5 species. The transported Probability Density Function (PDF) [53, 54] is arguably the best closure model for chemistry-turbulence interaction; as it does not require any additional models for the chemical source term. However, because of the high dimensionality of its argument, the model requires Monte-Carlo simulations of at least 30-50 notional particles in a cell. The PDF simulations are, thus, usually very computationally expensive even with a simple chemistry model [53].

As previously mentioned in chapter 1, an alternative model to the above methods is the flamelet method. The flamelet approach has been applied successfully to turbulent premixed flames [55–58] as well as non-premixed flames [59, 60]. The original Flamelet Progress Variable approach was developed by Pierce and Moin [61] for incompressible (constant pressure) flow. Pecnik et al. [62] later extended this approach to compressible flow. The CFPV has been applied successfully to supersonic and hypersonic combustion [62–64]. Pecnik et al. [62] simulated supersonic combustions in the Hyshot II Scramjet engine using a RANS turbulence model with the CPFV combustion model. Saghafian *et al.* [63, 64] simulated combustion of a jet in a supersonic crossflow and the HiFiRE Scramjet engine using a LES model with the same CFPV model. It is important to note that in the compressible limit, neglecting the transient pressure effect in the flamelet formulation (equation 2.61) poses a theoretical inconsistency. However, in this dissertation, both the time and length scales of the pressure oscillation in the chamber are much larger than those of the flamelets. Thus, a quasi-steady pressure assumption, in which the $\partial p/\partial t$ in the flamelet formulation, at any point during the pressure oscillation cycle might be justified.

2.3.1 Flamelet Library Generation

In any flamelet approach, the laminar flamelet solutions are first solved using the flamelet equations [46]. In a RANS-based turbulence solver, transport equations of the mean quantities are solved. Therefore, the laminar flamelet solutions are convoluted with assumed probability density functions (PDF) of independent scalars such as mean mixture fraction $\tilde{Z}$, and the mean variance $\widetilde{Z''^2}$. The β Probability Density Function (PDF) is assumed for the mixture fraction. The Dirac delta PDF is assumed for both the progress variable and pressure. The Favre-averaged thermo-chemical quantities ($\tilde{\psi}_i$) at each pressure value are

pre-processed as lookup libraries using the convolution

$$\tilde{\psi}_i(\tilde{Z}, \widetilde{Z''^2}, \tilde{C}, \bar{p}) = \int_0^p \int_0^C \int_0^1 \psi_i(Z, C, p)\beta(Z, Z''^2)\delta(C)\delta(p)dZdCdp \tag{2.23}$$

The β PDF has the form of

$$\tilde{P}(Z, Z''^2) = \frac{Z^{\alpha-1}(1-Z)^{\beta-1}}{\Gamma(\alpha)\Gamma(\beta)}\Gamma(\alpha+\beta) \tag{2.24}$$

where Γ is the gamma function. The shape functions α and β are related to the mixture fraction and its variance by

$$\alpha = Z\gamma, \qquad \beta = (1-Z)\gamma, \qquad \gamma = \frac{Z(1-Z)}{Z''^2} - 1 \geq 0 \tag{2.25}$$

2.3.2 Transport Equations

During the CFD computation, the transport equations for the scalars $\tilde{Z}, \widetilde{Z^2}, and \tilde{C}$ are solved. The mean mixture fraction squared ($\widetilde{Z^2}$) is related to the mean mixture fraction and the mean variance as

$$\widetilde{Z^2} = \tilde{Z}^2 + \widetilde{Z''^2}$$

At each time step, the local values of these scalars along with the pressure allow quick retrieval of flow properties such as local compositions, temperature, specific heat (c_p), enthalpy, and thermal diffusivity using pre-tabulated flamelet libraries. The flamelet transport equations, written in vector form, for these scalars are given as

$$\mathcal{Q} = (\bar{\rho}\tilde{Z}, \bar{\rho}\widetilde{Z^2}, \bar{\rho}\tilde{C})^T \tag{2.26}$$

The inviscid fluxes and divergence terms are defined as

$$\mathcal{F}_x = \begin{pmatrix} \bar{\rho}\tilde{u}\tilde{\tilde{Z}} \\ \bar{\rho}\tilde{u}\widetilde{Z^2} \\ \bar{\rho}\tilde{u}\tilde{C} \end{pmatrix}, \qquad \mathcal{F}_r = \begin{pmatrix} \bar{\rho}\tilde{v}\tilde{\tilde{Z}} \\ \bar{\rho}\tilde{v}\widetilde{Z^2} \\ \bar{\rho}\tilde{v}\tilde{C} \end{pmatrix}, \qquad \mathcal{H}^I = \begin{pmatrix} \bar{\rho}\tilde{v}\tilde{\tilde{Z}} \\ \bar{\rho}\tilde{v}\widetilde{Z^2} \\ \bar{\rho}\tilde{v}\tilde{C} \end{pmatrix} \tag{2.27}$$

With Lewis number equals to one, the viscous fluxes and their corresponding divergence terms are

$$\mathcal{G}_x = \begin{pmatrix} \left(\frac{\lambda}{C_p} + \frac{\mu_t}{Sc_t}\right)\frac{\partial\tilde{\tilde{Z}}}{\partial x} \\ \left(\frac{\lambda}{C_p} + \frac{\mu_t}{Sc_t}\right)\frac{\partial\widetilde{Z^2}}{\partial x} \\ \left(\frac{\lambda}{C_p} + \frac{\mu_t}{Sc_t}\right)\frac{\partial\tilde{C}}{\partial x} \end{pmatrix}, \quad \mathcal{G}_r = \begin{pmatrix} \left(\frac{\lambda}{C_p} + \frac{\mu_t}{Sc_t}\right)\frac{\partial\tilde{\tilde{Z}}}{\partial r} \\ \left(\frac{\lambda}{C_p} + \frac{\mu_t}{Sc_t}\right)\frac{\partial\widetilde{Z^2}}{\partial r} \\ \left(\frac{\lambda}{C_p} + \frac{\mu_t}{Sc_t}\right)\frac{\partial\tilde{C}}{\partial r} \end{pmatrix}, \mathcal{H}^V = \begin{pmatrix} \left(\frac{\lambda}{C_p} + \frac{\mu_t}{Sc_t}\right)\frac{\partial\tilde{\tilde{Z}}}{\partial r} \\ \left(\frac{\lambda}{C_p} + \frac{\mu_t}{Sc_t}\right)\frac{\partial\widetilde{Z^2}}{\partial r} \\ \left(\frac{\lambda}{C_p} + \frac{\mu_t}{Sc_t}\right)\frac{\partial\tilde{C}}{\partial r} \end{pmatrix} \tag{2.28}$$

The source terms are

$$\mathcal{S} = \begin{pmatrix} 0 \\ -\bar{\rho}C_x\omega(\widetilde{Z^2} - \tilde{Z}^2) \\ +\tilde{\dot{\omega}}_C \end{pmatrix} \tag{2.29}$$

where C_x has a constant value of 2.0 [62].

2.3.3 Mean Temperature and Pressure Calculation

At the end of each time step, the local values of the Favre-averaged thermal energy ($\tilde{e}$) can be different from the thermal energy (e_f) computed from the turbulent flamelet transport equations. However, the local compositions are the same for both quantities. Following Pecnik et al. [62], for a given $\tilde{e}$ value computed from the Navier-Stokes equations, an expansion

around the thermal energy of the flamelet solutions has the form

$$\tilde{e} = e_f + \int_{T_f}^{\tilde{T}} c_v(T)dT = e_f + \int_{T_f}^{\tilde{T}} \frac{R_f}{\gamma(T)-1}dT \tag{2.30}$$

where the subscript "f" denotes the values of the flamelet solution. The specific heat ratio (γ) can be expressed as

$$\gamma(\tilde{T}) = \gamma_f + a_\gamma(\tilde{T} - T_f) \tag{2.31}$$

where a_γ is the local linear expansion coefficient, tabulated during the pre-processing step as a flamelet library.

Integrating equation (2.30) and solving for $\tilde{T}$ we get

$$\tilde{T} = T_f + \frac{\gamma_f - 1}{a_\gamma}\Big(\exp(a_\gamma(\tilde{e} - e_f)/R_f) - 1\Big) \tag{2.32}$$

Finally, the ideal gas law is assumed for the equation of state

$$\bar{p} = \bar{\rho}\bar{R}\tilde{T} \tag{2.33}$$

where $\bar{R}$ is the specific gas constant that depends on the composition of the flow and $\tilde{T}$ is the temperature. Equation (2.32), together with the ideal gas law, illustrate the nonlinear coupling between the flame and the acoustical field.

2.4 Numerical Implementations

2.4.1 Spatial and Time Integration Schemes

Because of the complex geometry of the CVRC experiments, the code must be written as a multi-block solver. Figure 2.1 shows an example of the computational domain used in this dissertation. The computational domain consists of four horizontal blocks. At the interfaces between the blocks, the lower boundary of the top block coincides with the upper boundary of the bottom block.

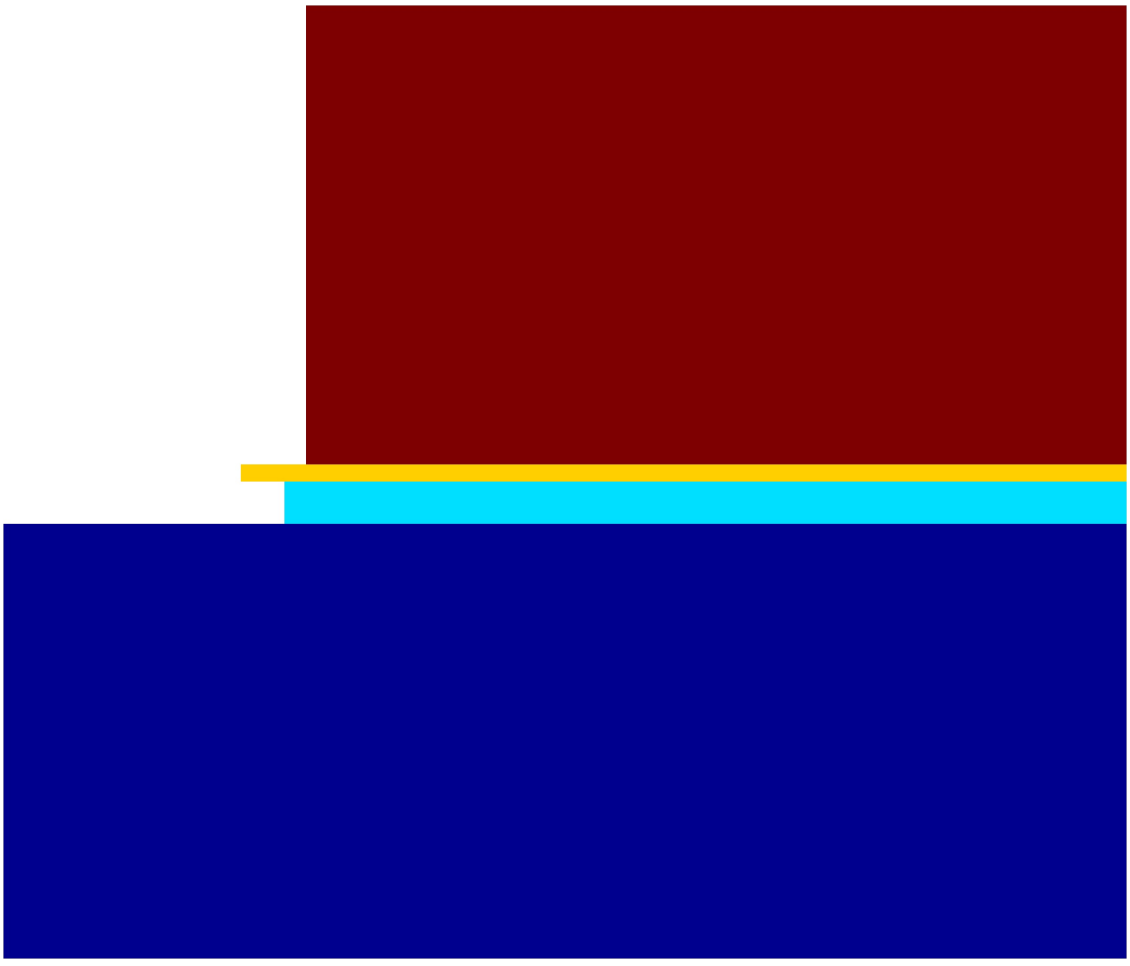

Figure 2.1: Computational blocks for the current solver.

Figure 2.2 represents the spatial discretization of any computational block. The four red

lines surround the block represent the internal nodes of the blocks surrounding it. These lines also represent ghost nodes to apply the boundary conditions. In figure 2.2, the vertical axis corresponds to the r-axis, the horizontal axis corresponds to the x-axis; where a (x,r) point has an index (j,i). Even though the computational grid shown here is uniform, the finite-difference discretization presented in this section is for a general nonuniform Cartesian mesh. For clarity purposes, the finite-difference scheme presented below is for the radial direction only. Extension to the axial or any other direction is straightforward.

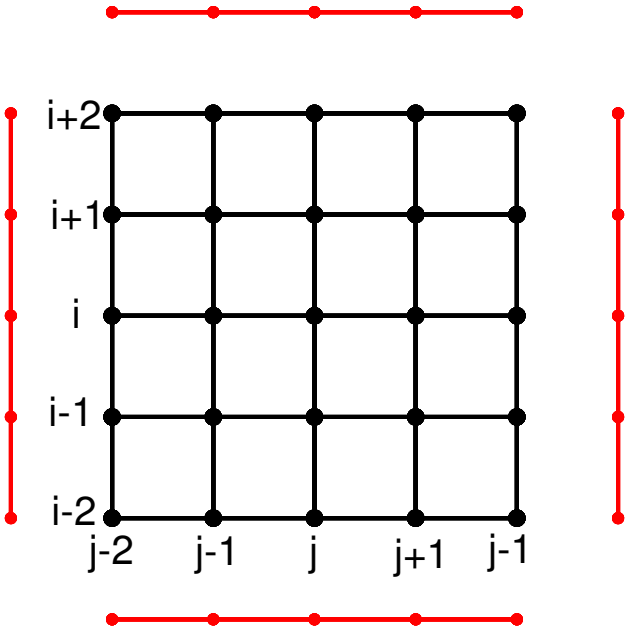

Figure 2.2: Computational grid for the current solver.

Following equation 2.1, the gradient of the inviscid fluxes in either direction is estimated using central differencing as

$$\left(\frac{\partial \mathcal{F}}{\partial r}\right)_{i,j} = \frac{\mathcal{F}_{i+1,j} - \mathcal{F}_{i-1,j}}{\Delta r^+ + \Delta r^-}, \qquad \Delta r^+ = r_{i+1} - r_i, \qquad \Delta r^- = r_i - r_{i-1} \tag{2.34}$$

For a reacting flow solver using a nonuniform grid, the discretization of the viscous fluxes is very cumbersome because of the nonuniform flow properties. For brevity purposes, we assume the viscous fluxes in the energy equation only consist of the heat fluxes in equation

2.6. Thus, their discretization in any direction is

$$\begin{aligned}\left(\frac{\partial \mathcal{G}}{\partial r}\right)_{i,j} &= \left(\frac{\partial q}{\partial r}\right)_{i,j} = \frac{1}{\Delta r^-}\Big[q_{i,j} - q_{i-1,j}\Big] \\ &= \frac{1}{\Delta r^-}\left[\left(\frac{\lambda}{C_p} + \frac{\mu_t}{Pr_t}\right)_{i,j}\frac{\tilde{h}_{i+1,j} - \tilde{h}_{i,j}}{\Delta r^+} - \left(\frac{\lambda}{C_p} + \frac{\mu_t}{Pr_t}\right)_{i-1,j}\frac{\tilde{h}_{i,j} - \tilde{h}_{i-1,j}}{\Delta r^+}\right]\end{aligned} \tag{2.35}$$

It is well known that the discretization of the inviscid fluxes using central differencing leads to numerical instability [65], especially in the regions where shock waves occur. Therefore, the Jameson-Schmidt-Turkel's hybrid second and fourth order artificial dissipation terms are added. In any direction, the dissipation terms have the form of

$$d_{i+1/2,j} = d^{(2)}_{i+1/2,j} + d^{(4)}_{i+1/2,j} \tag{2.36}$$

where the superscripts (2) and (4) represent their respective order (second and fourth). The second-order dissipation term has the form

$$d^{(2)}_{i+1/2,j} = \epsilon^{(2)}_{i+1/2,j}\lambda_{i+1/2,j}(\mathcal{Q}_{i+1,j} - \mathcal{Q}_{i,j}). \tag{2.37}$$

where $\lambda_{i+1/2}$ is the maximum one-dimensional wave speed and should not be confused with the coefficient of thermal conductivity.

$$\lambda_{i+1/2,j} = max\Big(|v_{i,j}| + c_{i,j}, |v_{i+1,j}| + c_{i+1,j}\Big) \tag{2.38}$$

and u is the flow velocity and c is acoustical wave speed. Similarly, the fourth-order dissipation term has the form

$$d^{(4)}_{i+1/2,j} = -\epsilon^{(4)}_{i+1/2,j}\lambda_{i+1/2,j}(\mathcal{Q}_{i+2,j} - 3\mathcal{Q}_{i+1,j} + 3\mathcal{Q}_{i,j} - \mathcal{Q}_{i-1,j}). \tag{2.39}$$

where the second- and fourth-order switching functions have the forms of

$$\epsilon^{(2)}_{i+1/2,j} = \kappa^{(2)} max(\nu_{i-1,j}, \nu_{i,j}, \nu_{i+1,j}, \nu_{i+2,j}). \tag{2.40}$$

and

$$\epsilon^{(4)}_{i+1/2,j} = max\left[0, \kappa^{(4)} - \epsilon^{2}_{i+1/2,j}\right]. \tag{2.41}$$

where the coefficients $\kappa^{(4)}$ and $\kappa^{(2)}$ are taken as 1/32 and 1/2, respectively. The pressure sensor has the form

$$\nu_j = \frac{|\bar{p}_{i-1,j} - 2\bar{p}_{i,j} + \bar{p}_{i+1,j}|}{|\bar{p}_{i-1,j} + 2\bar{p}_{i,j} + \bar{p}_{i+1,j}|} \tag{2.42}$$

The gradient of the dissipation terms are calculated as

$$\left(\frac{\partial d}{\partial r}\right)_{i,j} = \frac{d_{i+1/2,j} - d_{i-1/2,j}}{0.5(\Delta r^{+} + \Delta r^{-})} \tag{2.43}$$

The solver utilize a fourth order Runge-Kutta time integration scheme. In this method, the diffusive flux is only evaluated one time at the beginning of the time step. This technique is proven to save computational cost while maintaining the overall order of accuracy of the scheme [65]. The time integration scheme, together with the spatial discretization scheme

presented in equations (2.34-2.42), is described as follows

$$
\begin{aligned}
\mathcal{Q}_{i,j}^{(1)} &= \mathcal{Q}_{i,j}^{(n)} \\
\mathcal{Q}_{i,j}^{(2)} &= \mathcal{Q}_{i,j}^{(n)} + \frac{\Delta t}{4}\Bigg[- \left(\frac{\partial \mathcal{F}}{\partial x}\right)_{i,j}^{(1)} - \left(\frac{\partial \mathcal{F}}{\partial r}\right)_{i,j}^{(1)} + \left(\frac{\partial \mathcal{G}}{\partial x}\right)_{i,j}^{(1)} + \left(\frac{\partial \mathcal{G}}{\partial r}\right)_{i,j}^{(1)} + \frac{(\mathcal{H}^V)_{i,j}^{(1)} - (\mathcal{H}^I)_{i,j}^{(1)}}{r} + S_{i,j}^{(1)} \Bigg] \\
\mathcal{Q}_{i,j}^{(3)} &= \mathcal{Q}_{i,j}^{(n)} + \frac{\Delta t}{3}\Bigg[- \left(\frac{\partial \mathcal{F}}{\partial x}\right)_{i,j}^{(2)} - \left(\frac{\partial \mathcal{F}}{\partial r}\right)_{i,j}^{(2)} + \left(\frac{\partial \mathcal{G}}{\partial x}\right)_{i,j}^{(1)} + \left(\frac{\partial \mathcal{G}}{\partial r}\right)_{i,j}^{(1)} + \frac{(\mathcal{H}^V)_{i,j}^{(1)} - (\mathcal{H}^I)_{i,j}^{(2)}}{r} + S_{i,j}^{(2)} \Bigg] \\
\mathcal{Q}_{i,j}^{(4)} &= \mathcal{Q}_{i,j}^{(n)} + \frac{\Delta t}{2}\Bigg[- \left(\frac{\partial \mathcal{F}}{\partial x}\right)_{i,j}^{(3)} - \left(\frac{\partial \mathcal{F}}{\partial r}\right)_{i,j}^{(3)} + \left(\frac{\partial \mathcal{G}}{\partial x}\right)_{i,j}^{(1)} + \left(\frac{\partial \mathcal{G}}{\partial r}\right)_{i,j}^{(1)} + \frac{(\mathcal{H}^V)_{i,j}^{(1)} - (\mathcal{H}^I)_{i,j}^{(3)}}{r} + S_{i,j}^{(3)} \Bigg] \\
\mathcal{Q}_{i,j}^{(n+1)} &= \mathcal{Q}_{i,j}^{(n)} + \Delta t\Bigg[- \left(\frac{\partial \mathcal{F}}{\partial x}\right)_{i,j}^{(4)} - \left(\frac{\partial \mathcal{F}}{\partial r}\right)_{i,j}^{(4)} + \left(\frac{\partial \mathcal{G}}{\partial x}\right)_{i,j}^{(1)} + \left(\frac{\partial \mathcal{G}}{\partial r}\right)_{i,j}^{(1)} + \frac{(\mathcal{H}^V)_{i,j}^{(1)} - (\mathcal{H}^I)_{i,j}^{(4)}}{r} + S_{i,j}^{(4)} \Bigg] \\
\mathcal{Q}_{i,j}^{(n+1)} &= \mathcal{Q}_{i,j}^{(n+1)} + \Delta t\Bigg[\left(\frac{\partial d}{\partial x}\right)_{i,j}^{(n+1)} + \left(\frac{\partial d}{\partial r}\right)_{i,j}^{(n+1)} \Bigg]
\end{aligned}
\tag{2.44}
$$

Because the Runge-Kutta method is an explicit time integration scheme, it is restricted by the Courant-Friedrichs-Lewis (CFL) number. At the beginning of a time step, the maximum time step equals

$$
\begin{aligned}
\Delta t_x &= \frac{(\Delta x^+)}{|\tilde{u}| + c + 4\mu_t/(\Delta x)^+} \\
\Delta t_r &= \frac{(\Delta x^+)}{|\tilde{v}| + c + 4\mu_t/(\Delta r)^+} \\
\Delta t &= \sigma_{CFL}\ min\Bigg(\Delta t_x, \Delta t_r\Bigg)
\end{aligned}
\tag{2.45}
$$

where c is the local speed of sound and σ_{CFL} is the CFL number. In most second-order explicit schemes such as the Lax-Wendroff or MacCormack, the maximum CFL number cannot exceed unity. However, the current time integration scheme allows a theoretical CFL number of 1.8. In this dissertation, all simulations have a CFL value of 1.5.

2.4.2 Boundary Conditions

The solver uses four types of boundary conditions: inlet, outlet, wall, and centerline. Figure 3.1 shows the locations where these boundary conditions are applied.

Inlet

The CVRC experiment has a choked oxidizer inlet, forcing the early computations [41, 66] to use a complex geometry with choked slots to capture the correct instability behavior. However, Srinivasan et al. [39], Garby et al. [40] later demonstrated that a subsonic constant mass flow rate boundary condition captured the correct instability behavior without modeling the inlet choked slots. The boundary condition was implemented using the Navier-Stokes Characteristic Boundary Conditions (NSCBC) [67] method. Therefore, this method is applied in this dissertation for both of the propellant inlets. The approach is derived using one-dimensional characteristic analysis on the coordinate normal to the boundary (e.g., axial coordinate for the vertical inlets). Neglecting the viscous effects, the following characteristic analysis is only applied to the non-reacting parabolic parts (inviscid fluxes) of the Navier-Stokes equations. The inviscid fluxes of the Navier-Stokes equations in section 2.1 are repeated here as

$$\frac{\partial \mathcal{Q}}{\partial t} + \frac{\partial \mathcal{F}_x}{\partial x} + \frac{\partial \mathcal{F}_r}{\partial r} + \frac{\mathcal{H}^I}{r} = 0 \tag{2.46}$$

Define a vector Q contains primitive variables such as

$$Q = (\bar{\rho}, \tilde{u}, \tilde{v}, \bar{p})^T \tag{2.47}$$

Consider a characteristic analysis in the axial direction by transforming equation 2.46 into primitive variables, we get

$$\frac{\partial Q}{\partial t} + A\frac{\partial Q}{\partial x} + B\frac{\partial Q}{\partial r} + C = 0 \tag{2.48}$$

where matrices A, B, and C are defined as

$$A_{ij} = \left(\frac{\partial \mathcal{Q}_i}{\partial Q_j}\right)^{-1}\frac{\partial \mathcal{F}_{x,i}}{\partial Q_j}, \qquad B = \left(\frac{\partial \mathcal{Q}_i}{\partial Q_j}\right)^{-1}\frac{\partial \mathcal{F}_{r,i}}{\partial Q_j}, \qquad C = \left(\frac{\partial \mathcal{Q}_i}{\partial Q_j}\right)^{-1}\mathcal{H}^I \tag{2.49}$$

Equation 2.49 is the basis for the characteristic analysis. For a vertical boundary, the characteristic analysis is performed by finding the eigenvalues (wave speed) and the eigenvectors (wave amplitude) of matrix A. The same analysis of matrix B should be done for the radial direction. Rewriting the inviscid fluxes of the Navier-Stokes equations, we get

$$\frac{\partial \bar{\rho}}{\partial t} + d_1 + \frac{\partial(\bar{\rho}\tilde{v})}{\partial r} + \frac{(\bar{\rho}\tilde{v})}{r} = 0 \tag{2.50}$$

$$\frac{\partial(\bar{\rho}\tilde{u})}{\partial t} + d_1\tilde{u} + \bar{\rho}d_3 + \frac{\partial(\bar{\rho}\tilde{u}\tilde{v})}{\partial r} + \frac{(\bar{\rho}\tilde{u}\tilde{v})}{r} = 0 \tag{2.51}$$

$$\frac{\partial(\bar{\rho}\tilde{v})}{\partial t} + d_1\tilde{v} + \bar{\rho}d_4 + \frac{\partial(\bar{\rho}\tilde{v}\tilde{v})}{\partial r} + \frac{(\bar{\rho}\tilde{v}\tilde{v})}{r} + \frac{\partial \bar{p}}{\partial r} = 0 \tag{2.52}$$

$$\frac{\partial(\bar{\rho}\tilde{E})}{\partial t} + \frac{1}{2}\left(\tilde{u}^2 + \tilde{v}^2\right)d_1 + \frac{d_2}{\gamma - 1} + \bar{\rho}\tilde{u}d_3 + \bar{\rho}\tilde{v}d_4 + \frac{\partial(\tilde{v}(\bar{\rho}\tilde{E} + \bar{p}))}{\partial r} + \frac{\tilde{v}(\bar{\rho}\tilde{E} + \bar{p})}{r} = 0 \tag{2.53}$$

where the vector d_i is given as

$$d = \begin{pmatrix} d_1 \\ d_2 \\ d_3 \\ d_4 \end{pmatrix} = \begin{pmatrix} \frac{1}{c^2}\left[L_2 + \frac{1}{2}(L_4 + L_1)\right] \\ \frac{1}{2}(L_4 + L_1) \\ \frac{1}{2\rho c}(L_4 - L1) \\ L_3 \end{pmatrix} \tag{2.54}$$

where L_i are the wave amplitudes at the boundary and defined as

$$L_1 = (\tilde{u} - c)\left(\frac{\partial \bar{p}}{\partial x} - \bar{\rho} c \frac{\partial \tilde{u}}{\partial x}\right) \tag{2.55a}$$

$$L_2 = \tilde{u}\left(c^2 \frac{\partial \bar{\rho}}{\partial x} - \frac{\partial \bar{p}}{\partial x}\right) \tag{2.55b}$$

$$L_3 = \tilde{u} \frac{\partial \tilde{v}}{\partial x} \tag{2.55c}$$

$$L_4 = (\tilde{u} + c)\left(\frac{\partial \bar{p}}{\partial x} + \bar{\rho} c \frac{\partial \tilde{u}}{\partial x}\right) \tag{2.55d}$$

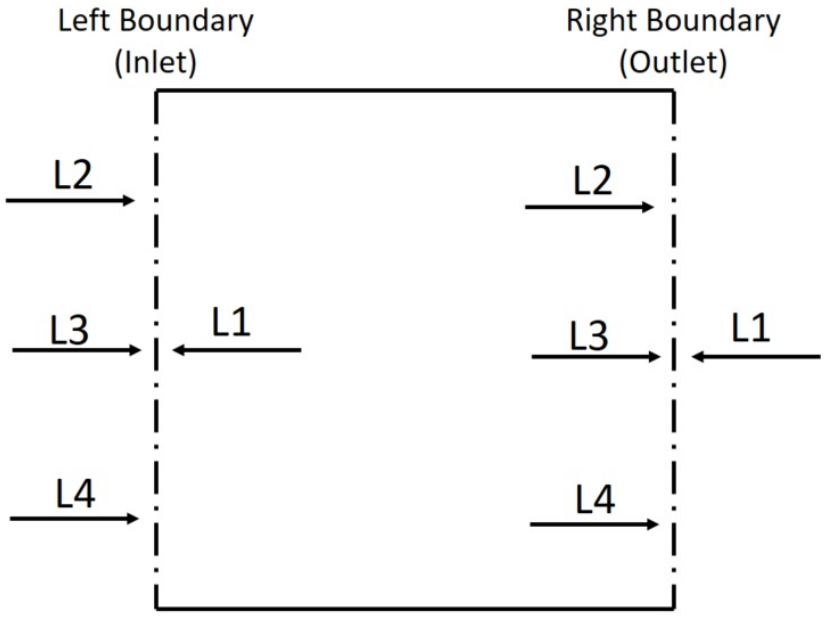

Figure 2.3: Illustration of different waves crossing vertical boundaries for subsonic flow in axisymmetric formulation.

Figure 2.3 shows the problems with the treatment of the boundary conditions in compressible flow. For a subsonic inlet, there are 3 incoming waves from outside of the computational domain while there is only one wave leaving the domain. One can treat the wave(s) leaving the domain with one-sided differencing. However, we cannot accurately predict the amplitude of the incoming waves simply using an extrapolation method. Poinsot and Lele [67] proposed that based on the physical conditions imposed on a boundary, we can estimate the incoming

wave amplitudes using Local One-Dimensional Inviscid (LODI) relations. LODI relations can only be viewed as compatibility equations to the physical conditions to produce a well-posed solution. The following conditions are imposed at the inlet:

1. Transient axial mass flux behavior is described.
2. Constant inflow temperature.
3. No swirling (zero radial velocity).
4. Constant composition.

These conditions lead to the following equations at the inlet [67]

$$L_4 = \frac{1}{(M\gamma + 1)}\left((M\gamma - 1)L_1 + 2\frac{\partial \bar{\rho}\tilde{u}}{\partial t}\right) \tag{2.56}$$

$$L_2 = 0.5(\gamma - 1)(L_4 + L_1) \tag{2.57}$$

where M is the local Mach number at the inlet. For a constant mass flow rate, the $\partial \bar{\rho}\tilde{u}/\partial t$ term in equation 2.56 becomes zero. For a case with triggering, a sinusoidal function is used. The solution procedure for the inlet is now described as follows

1. Calculate L_1 from equation 2.55
2. Calculate L_4 and L_2 from equations 2.56 and 2.57.
3. Calculate d_1 from equation 2.54
4. Solve for $\bar{\rho}$ using equation 2.50
5. Solve for $\tilde{u}$ from the imposed mass flow rate.
6. Impose the temperature and radial velocity.
7. Calculate the total energy from equation 2.3

Outlet

There are two types of exit boundary condition used in this dissertation. In most simulations, a short-choked-nozzle [68] outlet boundary condition is used in place of an actual convergent-divergent nozzle. Assuming the longitudinal dimension of the choked nozzle much smaller than the relevant acoustic wavelength, Crocco and Sirignano [68] derived the following relation

$$\frac{1}{M_x}\left[1+\frac{\gamma-1}{2}(M_x^2+M_r^2)\right]^{(\gamma+1)/(2(\gamma-1))} = \frac{A_c}{A_t}\left(\frac{\gamma+1}{2}\right)^{(\gamma+1)/(2(\gamma-1))} \tag{2.58}$$

Rearranging equation 2.58 gives

$$F(M_x,M_r) = \left[1+\frac{\gamma-1}{2}(M_x^2+M_r^2)\right]^{(\gamma+1)/(2(\gamma-1))} - M_x\frac{A_c}{A_t}\left(\frac{\gamma+1}{2}\right)^{(\gamma+1)/(2(\gamma-1))} \tag{2.59}$$

where M_x and M_r are the Mach number in the axial and radial directions, respectively. A_c/A_t is the entrance-to-throat area ratio, which has a value of 5 for the CVRC geometry. Assuming a constant γ value of 1.14, figure 2.4 plots the variable F in equation 2.59 as a function of M_x at various discreet values of M_r. Assuming $M_r = 0$, a solution is found at $M_x = 0.12$. There is a negligible difference in the solution for M_r values between 0 and 0.25. Therefore, the exit axial Mach number is kept constant at 0.12 for most simulations. Zero Lagrangian derivatives are applied to other primitive variables such as density, radial velocity. A constant pressure boundary condition is also implemented in this dissertation.

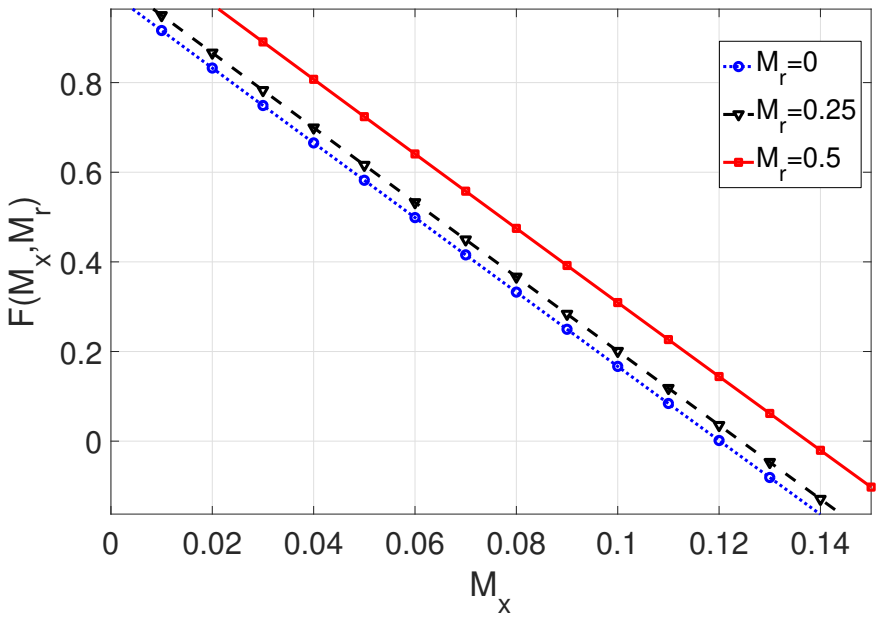

Figure 2.4: Solutions to the choked nozzle relation at various radial Mach numbers.

Walls and Centerline/Axis of Symmetry

No-slip walls are enforced in all simulations. Additionally, the walls are impermeable, which means the normal gradient across any wall of all scalars equals zero. In most simulations, adiabatic boundary condition in which the normal heat flux across the wall is also set to zero. In particular cases, heat loss across the main combustion chamber wall is simulated by imposing a constant mean temperature ($\tilde{T}$) at the wall. The solution procedure to this special boundary condition is described in chapter section 6. For axisymmetric simulations, zero gradients are imposed on all quantities except radial velocity across the centerline. Additionally, the radial velocity is set to zero at the centerline.

2.4.3 Initial Conditions

The initial conditions are modeled to enhance ignition and establish the operating condition quickly. At time t=0, the flow in the computational domain is filled with quiescent hot

products (T=2700K). The hot products ensure that the cold reactants can simultaneously combust. A hyperbolic tangent ramp function in the form of

$$\dot{m} = \frac{\dot{m}_i}{2}\left[tanh\Big(2k_0(t-t_0)\Big)+1\right] \tag{2.60}$$

gives a sufficiently slow transition for the injection of the propellants into the computational domain, where t has a unit of ms. k_0 and t_0 are constants and taken as 0.1 and 2.5 ms, respectively. $\dot{m}_i$ is either the steady-state fuel or oxidizer mass flow rate. The duration of injection is 4 ms. After the reactants are fully injected, the mass flow rates are kept constant.

2.4.4 Sampling data

Figure 2.5 shows the time history of a typical simulation. The explicit time integration scheme and the multi-scale nature of the problem results in the maximum time step being an order of magnitude larger than the minimum time step. If the flow fields are simply output by specifying the number of time steps (e.g., saving the results after every 1000 timesteps), the resulting data are non-uniformly sampled. Interpolation of any signal from non-uniform to uniform sampling cannot preserve the phase of the original signal. Another approach is to take the smallest time step in the simulation. However, as shown in figure 2.5, doing so would increase the number of time steps required by at least an order of magnitude.

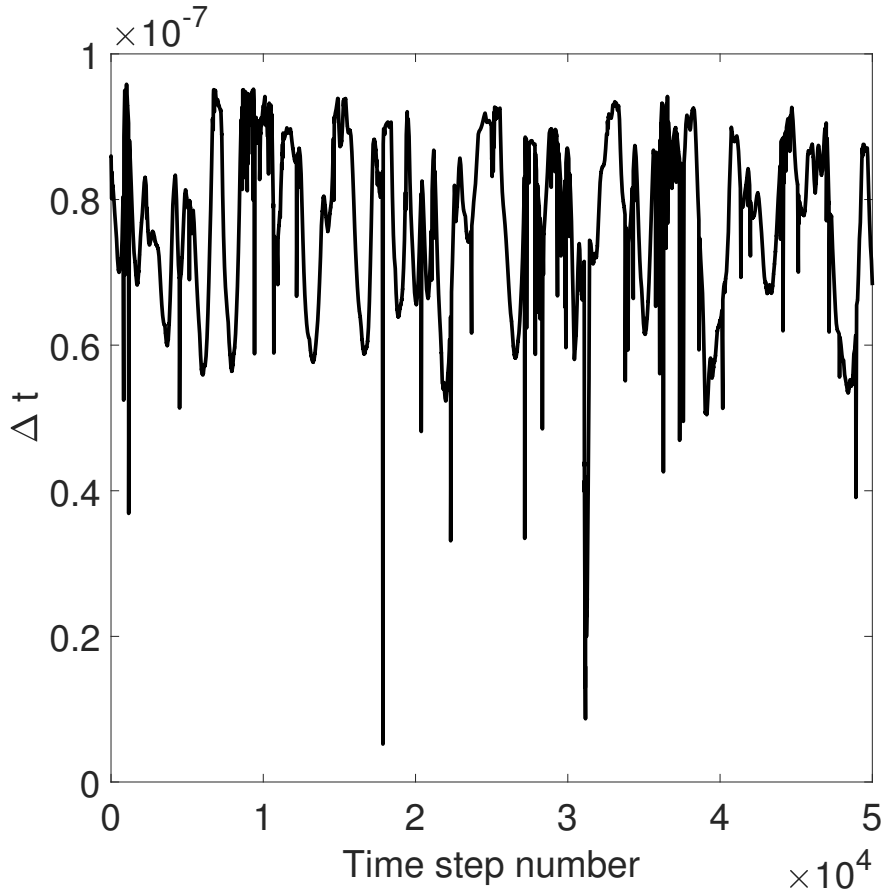

Figure 2.5: Simulation time step size as a function of the number of time step taken.

A new approach is thus developed. This approach allows the solver to advance in time efficiently while sampling the data at the desired frequency. The new algorithm significantly improves the post-processing process. For a specific sampling time (t_s) that is larger than the maximum time step allowed, the following algorithm is used

Algorithm 1 Sampling data algorithm.

```
1: procedure SIMULATION(tend,ts)   ▷ Inputs: tend and ts are simulation and sampling times
2:     tf=0                        ▷ Initialized the overall physical flow time.
3:     while tf¡tend do            ▷ Start the simulation
4:         t=0                     ▷ Reset the data loop time.
5:         while (t < ts) do       ▷ Start data loop
6:             Find Δt             ▷ Use equation 2.45
7:             tn = t + Δt
8:             if Δt < (ts − tn) then
9:                 Δt = Δt
10:            else if Δt > (ts − tn) then
11:                Δt = (ts − tn)
12:            end if
13:            Compute the fluxes
14:            Advance in time     ▷ Equation 2.44
15:            t = t + Δt          ▷ Data loop time
16:            tf = tf + Δt        ▷ Physical flow time
17:        end while               ▷ End data loop
18:        Save the data
19:    end while                   ▷ End overall simulation
20: end procedure
```

2.4.5 Solution Procedure

The coupling of the flamelet model with the CFD necessitates outlining the solution procedure. There are two main steps to the solution procedure

1. Flamelet libraries (Lookup Tables) Generation

2. The flamelet libraries are used as inputs in the main CFD computations.

Flamelet Library Generation

In the first step, flamelet libraries must be generated from the laminar flamelet solutions. The laminar flamelet solutions are obtained using the FlameMaster code [69]. A 72-reaction detailed mechanism with 27 species (neglecting nitrogen) is used [70]. The flame solutions are obtained by solving the steady-state counterflow diffusion flame in the mixture fraction space using

$$-\frac{\rho\chi}{2}\frac{\partial^2\psi_i}{\partial Z^2} = \dot{\omega}_i \tag{2.61}$$

where ψ_i can be any scalar quantities such as species mass fractions and temperature. For a detailed mechanism, Z is the mixture fraction defined by Bilger [46]. Figure 2.6 show typical fully burning flamelet solutions obtained in this dissertation.

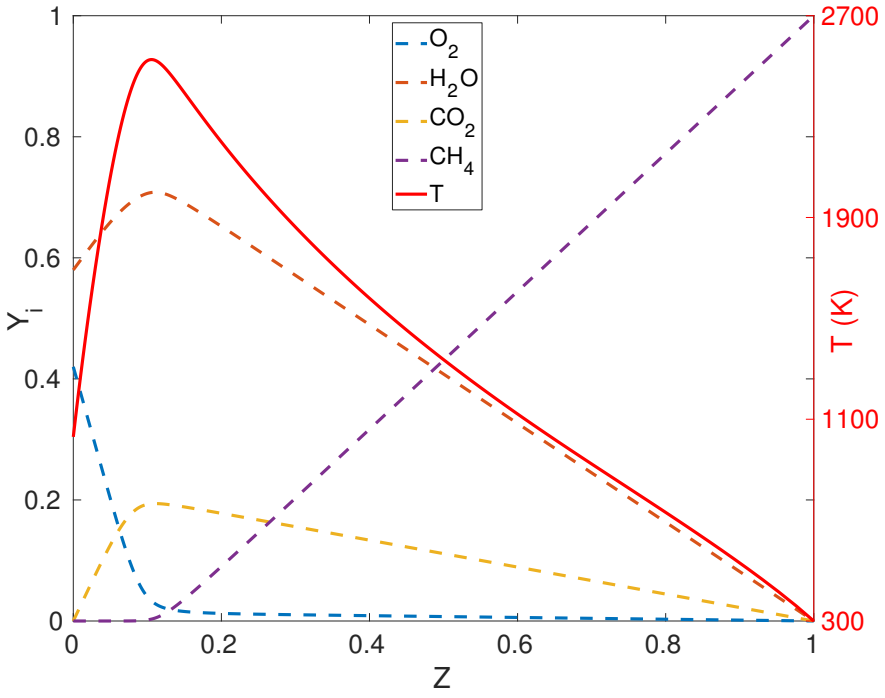

Figure 2.6: Flamelet solutions of major species mass fraction and temperature at specific progress variable and pressure values.

Using equation 2.23, for a specific progress variable and pressure, the above temperature solution is convoluted, resulting in a single flamelet library for temperature, as shown in figure 2.7. The progress variable (C) is defined as the total mass fraction of H_2 and CO_2 in this dissertation. The progress variable distinguishes between different flamelet solutions, from purely mixing ($C = 0$) to fully stable burning solution ($C = C_{max}$).

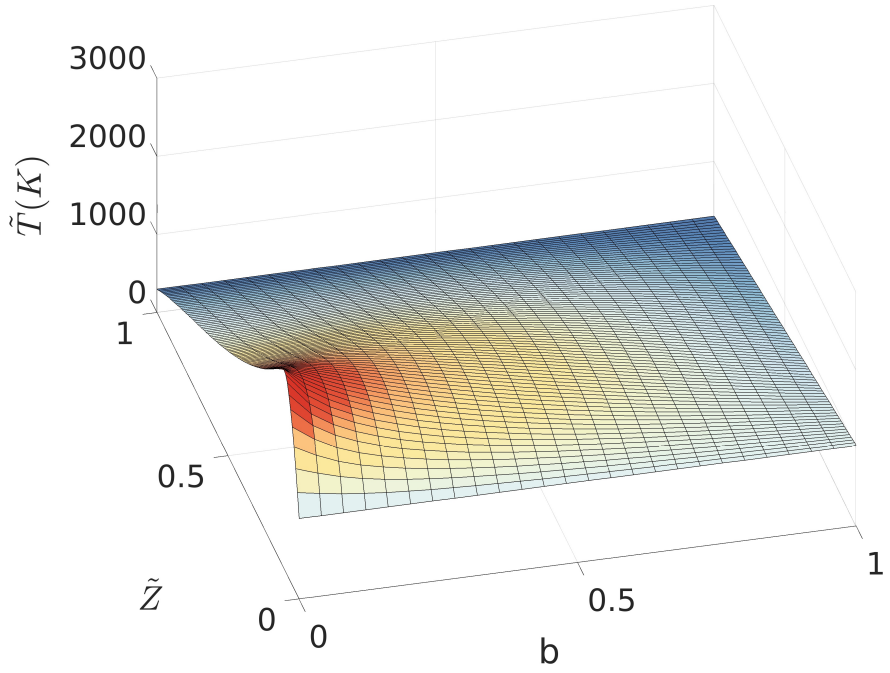

Figure 2.7: Single flamelet library.

The flamelet library shown in figure 2.7 is parametrized by the mean mixture fraction ($\tilde{Z}$) on the x-axis and the normalized variance, defined as

$$b = \frac{\widetilde{Z^2} - \tilde{Z}^2}{\tilde{Z} - \tilde{Z}^2} \tag{2.62}$$

Additional flamelet libraries for all the progress variables at various pressures are also generated. Therefore, the entire flamelet library of temperature is a four-dimensional array. The pressure ranges from 1 to 30 atm for each flamelet library, sufficiently covering even the most unstable cases. All the thermo-chemical quantities are also tabulated as flamelet libraries.

2.4.6 Main CFD Computation

A schematic of the solution procedure of the CFD computation is shown in figure 2.8. There are 9 transport equations used in the main CFD computation: 4 Navier-Stokes equations

(section 2.1), 2 turbulence model equations (section 2.2.1), and 3 combustion model equations 2.3. From known conditions at time n, the solution will be advanced to time n+1. The code updates all of these conserved variables at the same time to ensure strong coupling. The step of finding all the flamelet related quantities can be summarized as follows. Each quantity such as $(T_f^{n+1}, e_f^{n+1}, a_f^{n+1}, R_f^{n+1})$ has its corresponding pretabulated flamelet libraries (four-dimensional arrays). At each grid point in the computational domain, using the values of $\tilde{Z}^{n+1}, \widetilde{Z^2}^{n+1}, \tilde{C}^{n+1}, \bar{p}^n$, each quantity is computed from interpolation using its respective flamelet library.

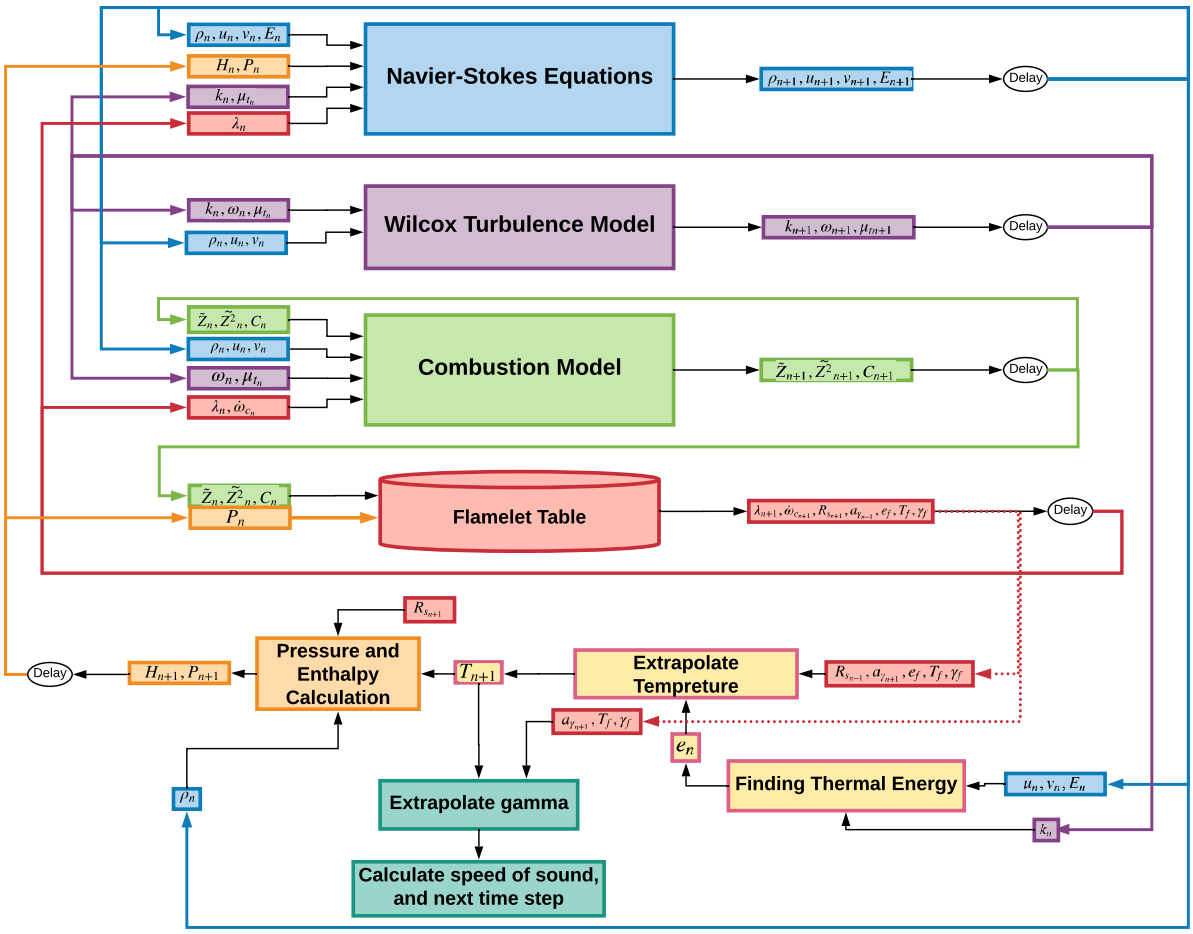

Figure 2.8: Solution procedure of the current solver.

Chapter 3

Computational Validations

3.1 Simulation Details

Figure 3.1 shows the computational domain as well as a typical mesh used in this dissertation. Not all grid points, especially around the backstep, are shown for clarity purpose. The red solid lines surround the mesh borders denote the location where the wall boundary conditions are applied. The blue line at the bottom (r= 0 cm) indicates the axis of symmetry. The two solid green vertical lines mark the locations of the propellant injection, with the oxidizer being injected into the center tube. The dash green line marks the outlet, where the short-choked-nozzle boundary condition is applied.

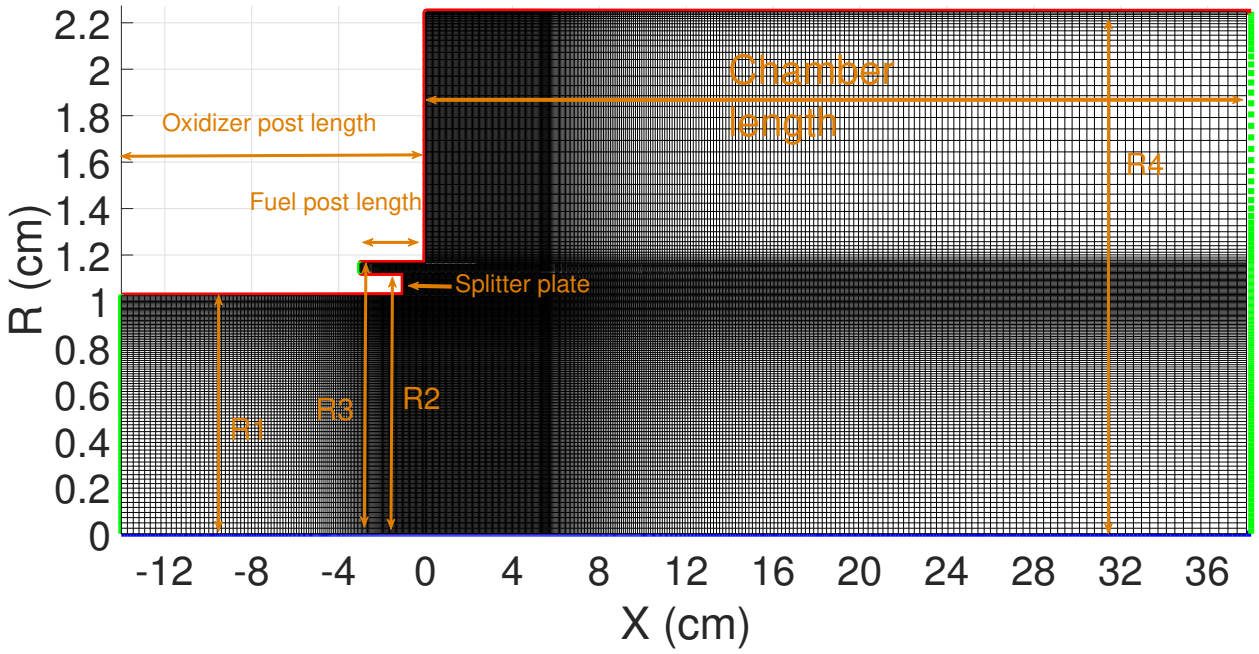

Figure 3.1: Computational domain and mesh used in the current solver. Depending on the case, all dimensions are fixed except for the oxidizer post and chamber lengths. The dimensions are shown for the 14cm case.

Table 3.1 shows the dimensions of the computation domain according to figure 3.1. The last column indicates whether these dimensions are fixed between different cases.

Table 3.1: Dimensions of the computational domain.

Dimension name	**Range of value (cm)**	**Fixed?**
Oxidizer post radius (R1)	1.025	Yes
Fuel post inner radius (R2)	1.125	Yes
Fuel post outer radius (R3)	1.1625	Yes
Chamber radius (R4)	2.25	Yes
Oxidizer post length	9-19	Yes
Fuel post length	3	No
Chamber length	38	Yes
Splitter plate to backstep	1	No

The following details the approach used to generate a high-quality mesh for the current computational domain. In the radial direction, more grid points are placed near all the walls and in the mixing shear layer. In the axial direction, from 2 cm around the upstream of the splitter plate to 5 cm downstream of the chamber back-step, a uniform grid is used. The grid is stretched with factors between 1.03 to 1.05 toward the inlet of the oxidizer post and the exit of the combustion chamber. This means neighboring grid sizes are within 5 % of each other, ensuring a smooth varying mesh. The smallest axial grid size is four times larger than the minimum radial grid size. Harvazinski [66] showed that, by employing a relatively coarse mesh of roughly 55000 cells, axisymmetric simulations can still reasonably capture the correct unstable behaviors of the CVRC experiments while under-predicting the oscillation magnitudes by a factor of 2 or more. Therefore, to efficiently evaluate the ability of the newly written code in capturing the correct physics, the mesh size of roughly 60000 grid points are used for all the cases presented in chapters 3-4.

In the CVRC experiment, the combustion chamber has a fixed length of 38 cm. As seen from table 3.1, the oxidizer post length can be continuously varied from 19 cm to 9 cm. Three different cases of the CVRC experiment are used to benchmark against our computational results. These cases correspond to various oxidizer post lengths: 9 cm, 12 cm, and 14 cm. In these cases, the short-choked-nozzle boundary condition is applied. The results in this chapter are primarily taken from Nguyen et al. [71]. Additional materials are added for further clarifications.

Initially, the computational domain only contains hot products under quiescent conditions. As previously mentioned, both the fuel and oxidizer is slowly injected into the computational domain with a 4 ms period of injection (section 2.4.3). The fuel is methane with a temperature of 300 K. The oxidizer is decomposed hydrogen peroxide at 1030 K, which consists of 58 % H_2O and 48 % O_2. Unless otherwise stated, the fuel and oxidizer mass flow rates are held constant at 0.027 kg/s and 0.32 kg/s, respectively. The mass oxidizer-to-fuel ratio based on

the inlet flow rates is 11.85. With a stoichiometric oxidizer-to-fuel ratio of 9.52, the flow is globally fuel lean with an equivalence ratio of 0.8.

3.2 Assessment of the Computational Cost

As previously mentioned, a purpose of this work is to develop a computationally efficient numerical tool. Table 3.2 compares the computational cost between this work and other various simulations performed by different groups.

Table 3.2: Computational cost for various simulations of the CVRC experiment.

Institution	**Type**	**Mesh size**	**Number of species**	**Core hours per ms**
UCI	Axisymmetric	6.26E4	27	0.28
CNRS [40]	Axisymmetric	7E5	5	160
Purdue [66]	Axisymmetric	5.5E4	4	53
Purdue [66]	Axisymmetric	2E5	4	480
CNRS [40]	3D	14E6	5	1024
AFRL [72]	3D	4E6	4	11520
AFRL [72]	3D	4E6	31	259200
Georgia Tech. [39]	3D	1.4E6	5	3333

As seen in table 3.2, most of these simulations use either a global one- or two-step chemical mechanism (4-5 species). The same code called General Equation and Mesh Solver (GEMS) is used at both Purdue University and Air Force Research Laboratory (AFRL), which can perform both 3D and axisymmetric simulations [66]. Furthermore, the GEMS solver employs similar turbulence model used in this work, the Wilcox's k-ω based DES model. The simulation performed at the Centre National de la Recherche Scientifique (CNRS) employed the classical Smagorinsky LES turbulence model. Both axisymmetric and 3D simulations were

performed. While the axisymmetric calculations were at least an order of magnitude cheaper than its 3D counterpart, the general conclusion is that only some features of the instability were qualitatively reproduced. Additionally, the axisymmetric calculations under-predict the oscillation amplitude by $20\% - 50\%$.

Table 3.2 shows that our computational cost per ms of physical time is by far the least expensive, even compared to existing axisymmetric calculations. The reasons for such low computational costs can be explained on two fronts. First, the time integration scheme used here is an explicit scheme. The solvers employed at CNRS and Georgia Tech both use variations of the explicit predictor-corrector time integration scheme, which requires the CFL number to be much smaller than unit. The GEMS code, on the other hand, uses a fully implicit scheme, which requires many iterations per time step. Consequently, the computational costs for all the GEMS code simulations are always higher. Second, the turbulent combustion model employed in this work utilized a series of flamelet libraries as preprocessed lookup tables. There are only three transport equations solved for the chemistry regardless of the chemical mechanisms used. In comparison, even the simplest global chemical mechanisms required at least four transport equations (two reactants and two products). Therefore, the associated cost of calculating the flow thermodynamics properties at the end of each time-step is greatly reduced.

3.3 Frequencies and Modeshapes

In this section, Power Spectral Density (PSD) is first applied to identify the dominant frequencies of the longitudinal modes. Spatial mode shape of the first longitudinal mode is then discussed and compared to existing simulation results by Srinivasan et al. [39]. Figure 3.2 shows a typical PSD result obtained in this work.

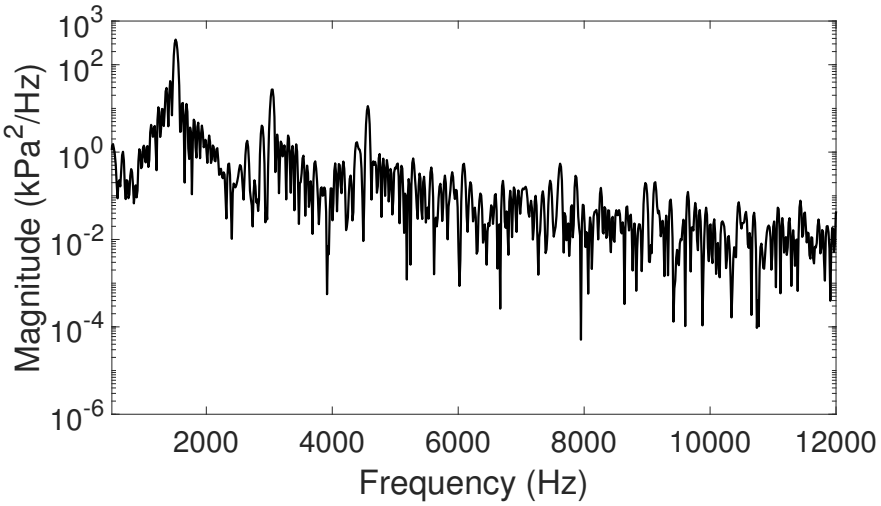

Figure 3.2: PSD responses of the 14-cm post case at x= 37 cm on the combustor wall.

Table 3.3 shows the first three dominant frequencies. The table also presents comparisons with the experimental data as well as the computational results by Srinivasan et al. [39]. For the 12- and 14-cm oxidizer post, our results over-predict the dominant frequencies compared to the experimental results. However, this trend is consistent with existing computational results. For the 9-cm oxidizer post, our results for the first dominant frequency, as well as oscillation amplitude, matches the experimental results extremely well while Srinivasan et al. over-predicted both quantities. It is possible that the higher frequency is predicted because the wave dynamics depends on a sound speed determined on the resolved scale where larger temperatures occur.

Table 3.3: Dominant frequencies on the combustion chamber wall at x=0.37 cm.

Oxidizer Post Length	**First mode (Hz)**	**Second mode (Hz)**	**Third Mode (Hz)**
9 cm - Computation (UCI)	1400	2900	4350
9 cm - Computation (Srinivasan)	1686	2791	3373
9 cm - Experiment	1392	2704	3772
12 cm - Computation (UCI)	1600	2906	4500
12 cm - Computation (Srinivasan)	1613	3268	4881
12 cm - Experiment	1385	2777	4169
14 cm - Computation (UCI)	1520	2880	4440
14 cm - Computation (Srinivasan)	1592	3130	4722
14 cm - Experiment	1331	2655	3986

Figure 3.3 compares the pressure oscillation amplitudes for the three reported cases. The sampling location is on the combustion chamber wall before the entrance of the convergent nozzle ($x = 37\ cm$). The time is zeroed by an arbitrary time t_o after the flow has reached the limit cycle. The x-axis is normalized by the periods of the first mode frequencies identified during the PSD analysis for each case.

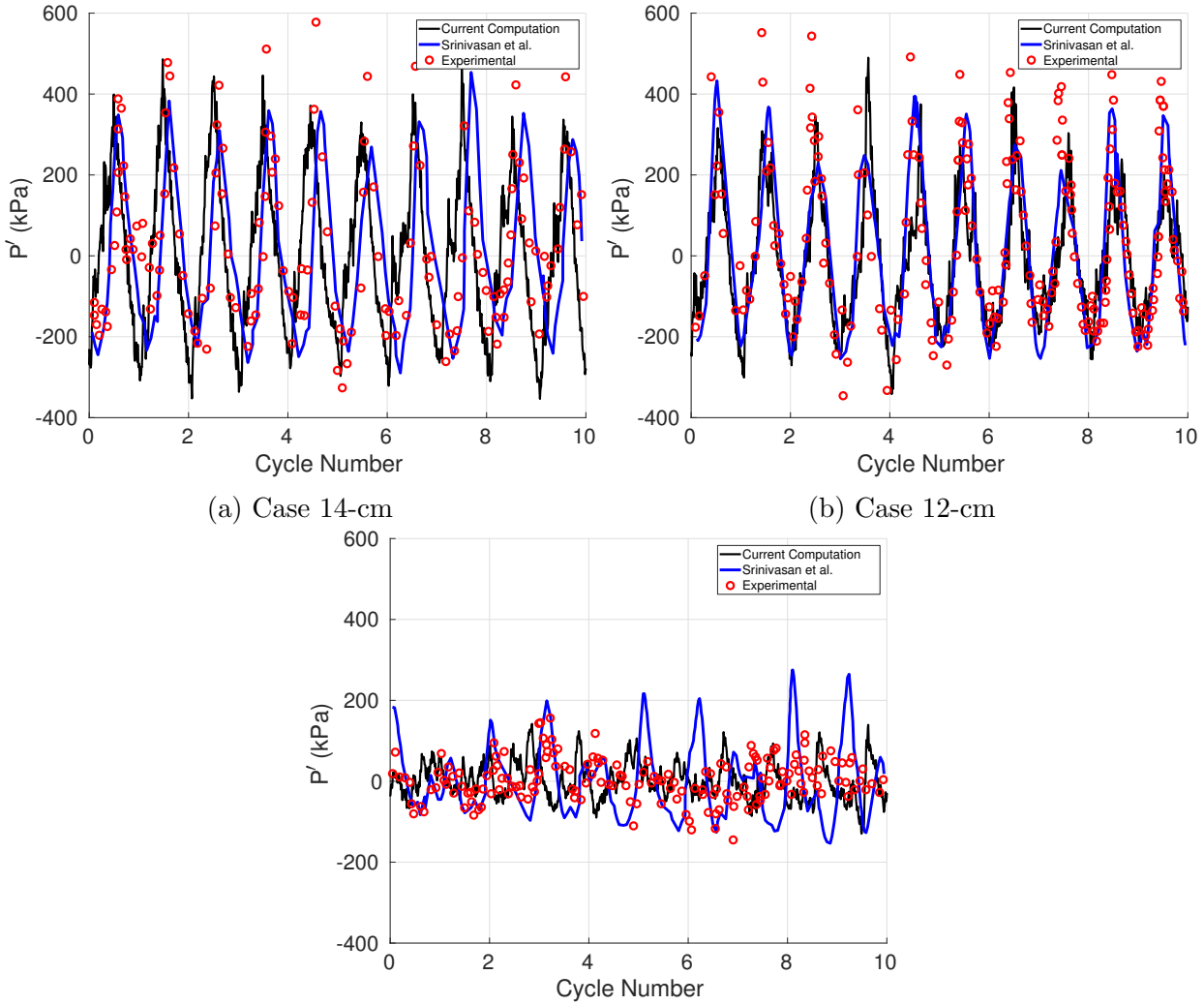

(a) Case 14-cm

(b) Case 12-cm

(c) Case 9-cm

Figure 3.3: Pressure time evolutions comparisons between the current works and 3D calculations of Srinivasan et al. and experimental data [39]. Existing data are obtained using digitizing softwares.

For the 9-cm oxidizer post case, the chamber is observed as semi-stable, with a peak-to-peak pressure oscillation of 200 kPa. For the 12-cm oxidizer post case, the system is unstable with a peak-to-peak amplitude of 450 kPa. The 14-cm post length exhibits similar behavior but with a much larger peak-to-peak amplitude of 600 kPa. In the unstable cases, these results, computed by the current solver, under-predict the pressure oscillation magnitude by $15\% - 20\%$ compared to experimental data. On the other hand, 3D calculations under-

predicted the oscillation magnitude within 10% of the experimental data [39, 40, 72]. Our results, however, predict larger peak-to-peak oscillation amplitudes compared to existing axisymmetric calculations using global chemistry mechanisms [40, 43].

Figure 3.4 compares the first longitudinal mode shape found in the present work as well as the results of Srinivasan et al. [39]. For each axial location at an instance in time, the pressure fields are first volume-averaged along the radial direction. This creates two-dimensional pressure fields as functions of x and t. The transient pressure signals at each axial location are then Fourier-transformed, and the corresponding modulus of the first mode frequency identified in table 3.3 are extracted. For the unstable cases, our results agree with the existing computational results. The correct mode shape found in these cases further validates our usage of the exit boundary condition, as the nozzle entrance should behave as a pressure anti-node.

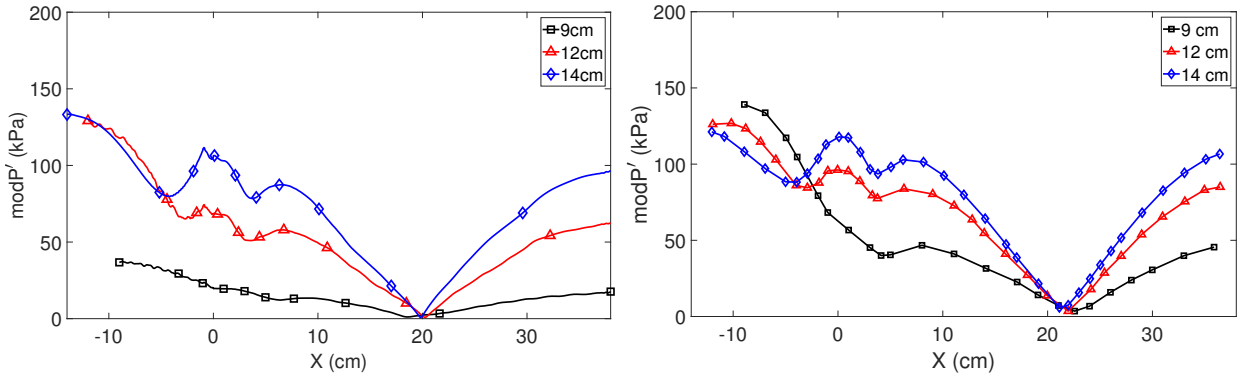

(a) Present work (b) Srinivasan et al. [39]

Figure 3.4: First longitudinal mode shape for all three cases.

Similar to existing simulations, over-predictions of oscillation frequencies in the unstable cases can attribute to the usage of adiabatic boundary conditions, which leads to a much higher mean chamber pressure and increase in the sound speed [39, 40]. Figure 3.5 shows the time-averaged heat release rate for all three cases. For the unstable cases, the flames quickly expand radially downstream of the dump plane. On the other hand, most of the reactions concentrate around the shear layer in the 9-cm oxidizer post case. Therefore, it can be argued

that the adiabatic wall boundary condition has less of an effect in the 9-cm-oxidizer-post case compared to the unstable cases. This phenomenon results in lower mean chamber pressure compared to the unstable cases, in addition to the lower oscillation amplitude.

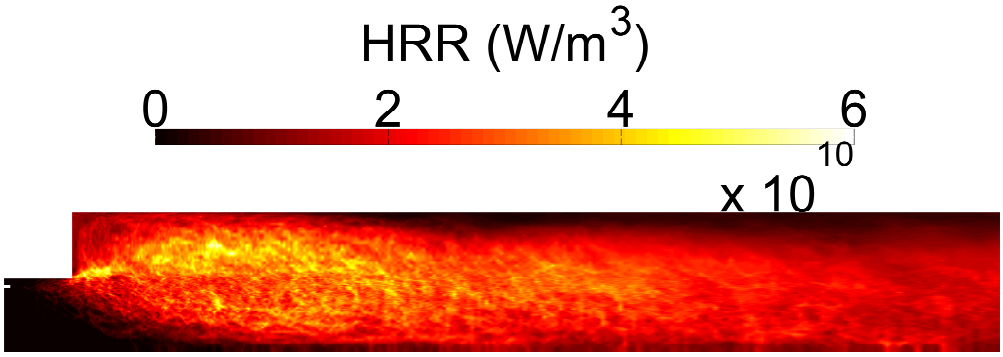

(a) 14-cm post

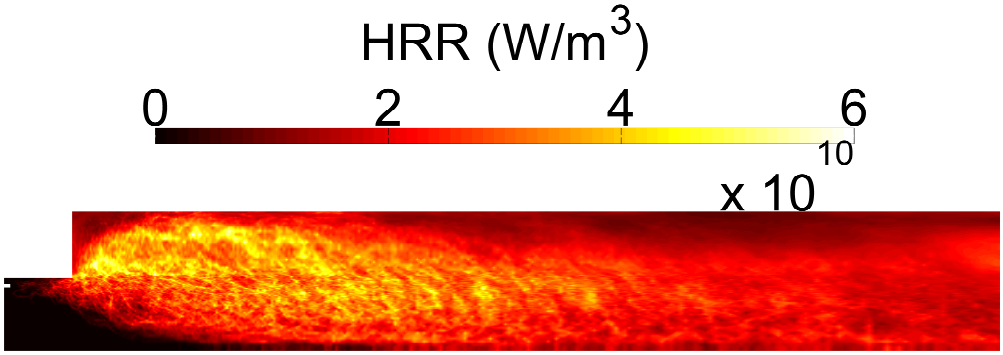

(b) 12-cm post

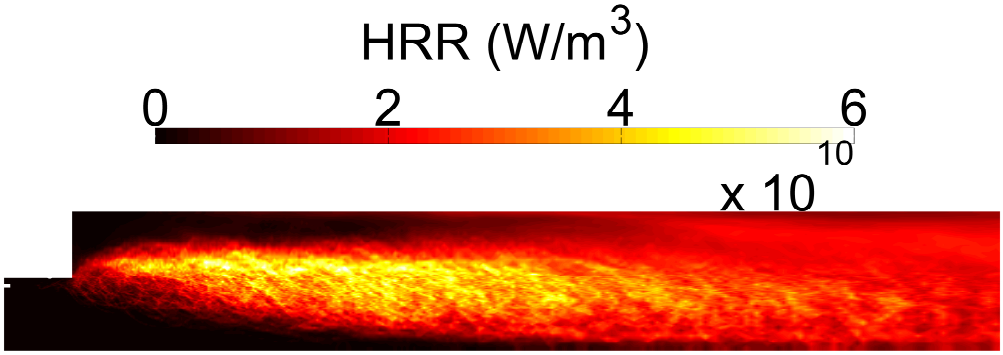

(c) 9-cm post

Figure 3.5: Time-averaged heat release rate for all three cases.

Figure 3.4 also offers a second explanation on why our 9-cm post case matches the experiments very well. In Srinivasan's results, there are clearly half-wave standing waves present in the chamber. There is a pressure node at $x = 20\ cm$. The pressure anti-nodes locate

immediately downstream of the dump plane ($x = 5\ cm - 6\ cm$) and the entrance of the nozzle ($x = 38\ cm$) for all oxidizer post lengths. This means the full traveling pressure wavelength is about $0.64 - 0.66\ m$ for the unstable cases. The volume- and time-averaged sound speed in the chamber for the 14-cm post is around 1080 m/s, leading to a frequency of approximately 1600 Hz. The 10% difference compared to the value reported in table 3.3 is due to the influence of the bulk velocity. In our results for the 9-cm oxidizer post, there is no distinct pressure anti-node downstream of the dump plane. The traveling pressure wave in the chamber then simply reflects at the back-step wall. The full wavelength, in this case, is $0.76\ m$, with the volume- and time-averaged acoustical speed of 1077 m/s. The calculated frequency is consequently around 1417 Hz, which agrees well with the values reported in table 3.3.

3.4 Time-Averaged Behaviors

Figure 3.6 shows the time-averaged temperature and velocity field for all three cases. The entire length of the chamber is shown. The top half of each sub-figures corresponds to the temperature fields while their bottom halves present the axial velocity field. The black iso-lines (T=2000 K) in the temperature figures are used to identify the mean flame length. The recirculation zones are enclosed by black iso-lines (U=0). As seen in figure 3.6, the flame as well as recirculation zones are shorter for the unstable cases (14 cm and 12 cm) compared to the semi-stable cases. The mean flame lengths are 28 cm, 15 cm, and 14.6 cm for the 9-, 12-, and 14-cm cases, respectively. The recirculation lengths are 21.8 cm, 10 cm, and 6.23 cm for the 9-, 12-, and 14-cm cases, respectively. These differences indicate that as the oscillation amplitudes increase, the flame becomes more compact.

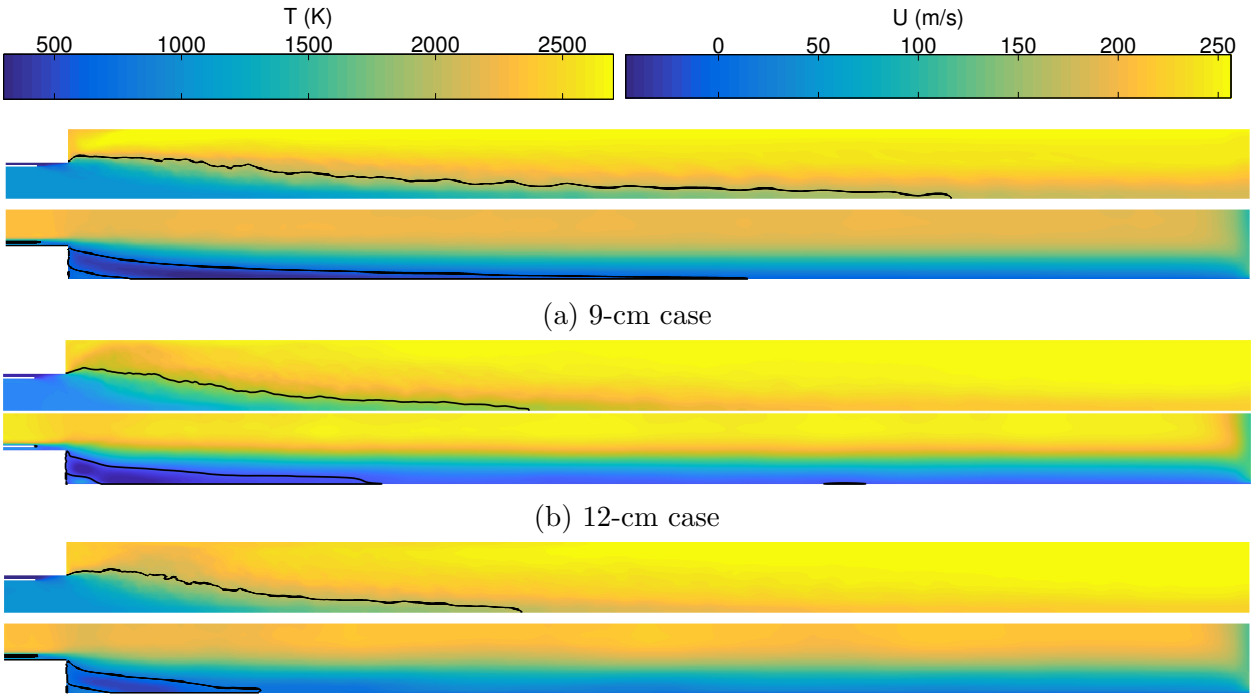

(a) 9-cm case

(b) 12-cm case

(c) 14-cm case

Figure 3.6: Time-averaged temperature and axial velocity for all three cases.

As expected due to lack of transport across the centerline, our axisymmetric simulations predict longer flames than 3D calculations. In an axisymmetric simulation for the 12-cm case, Garby et al. [40] calculated a flame length of 22 cm with peak-to-peak pressure oscillation of 320 kPa. Therefore, the larger pressure oscillation amplitudes in our simulations contribute to increased mixing and thus shorter flames. Further explanations about the mixing characteristics between these cases are presented in chapter 4.

Figure 3.7 compares the time-averaged fuel mass fraction of this present work to those of Srinivasan et al. [39]. The x-axis is normalized by the diameter of oxidizer post. The present results are plotted across the centerline because Srinivasan et al. [39] shows their results for the bottom half of the chamber.

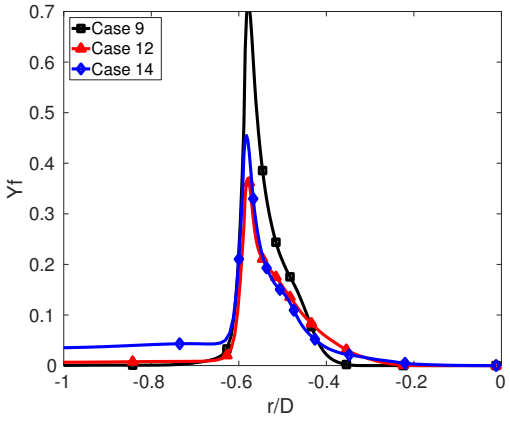

(a) x= 0 cm, present work.

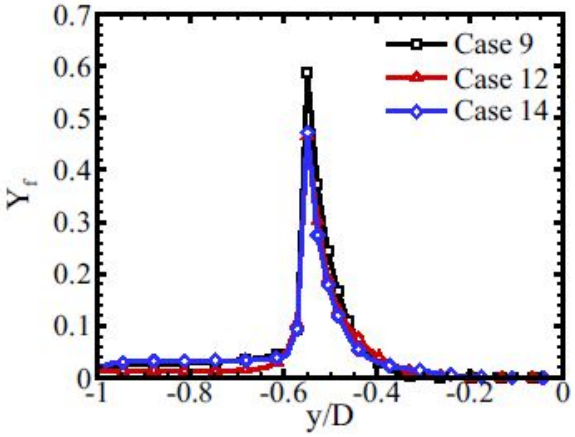

(b) x= 0 cm, existing data.

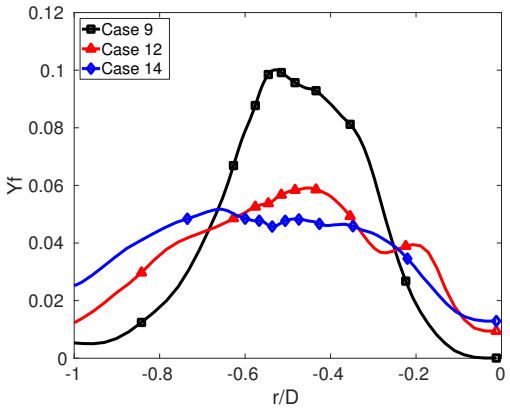

(c) x= 3.08 cm, present work.

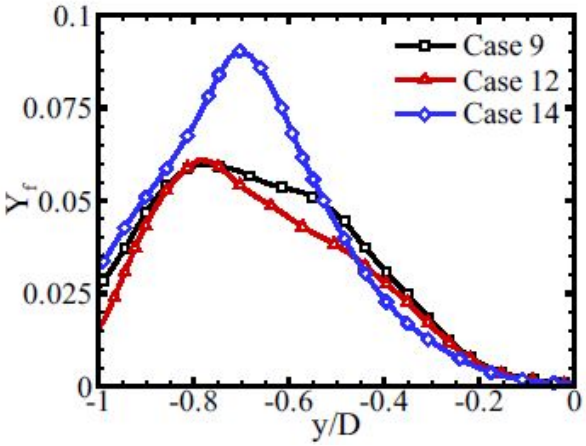

(d) x= 3.08 cm, existing data.

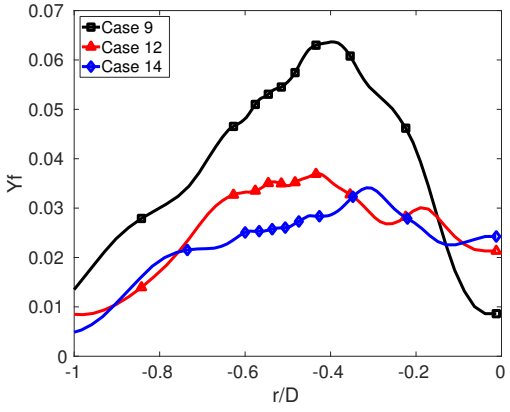

(e) x= 6.15 cm, present work.

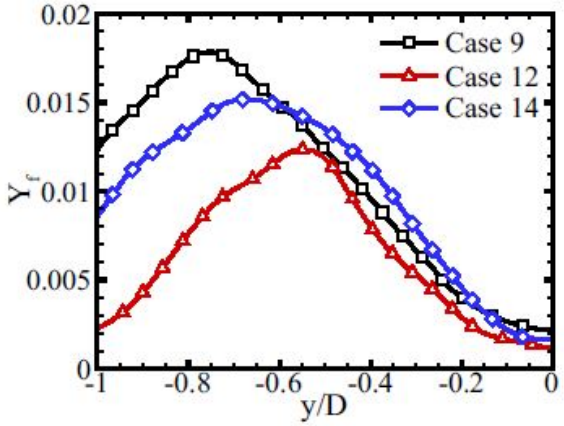

(f) x= 6.15 cm, existing data.

Figure 3.7: Comparison of the time-averaged fuel mass fraction at various axial locations for all cases between the present work (left column) and Srinivasan et al. [39] (right column)

At the dump plane ($x = 0cm$), our results agree well with the 3D calculations for the unstable cases. There is considerably more unburnt fuel entering the combustion chamber in the present calculation for the 9-cm case. Srinivasan's calculations predict much higher oscillation amplitudes. Therefore, the mixedness in their calculations increases and results in more burning. As we move downstream, there is more unburnt fuel in our simulations compared to the 3D calculations, leading to longer flames.

3.5 Concluding Remarks

A code for compressible axisymmetric chemically reacting flow in a rocket combustion chamber is developed. Pressure results are benchmarked against both existing experimental and computational results. The semi-stable case 9C matches experimental results very well. In the unstable cases, all current computations including our work under-predict the pressure oscillation magnitude while over-predicting the oscillation frequency. Existing 3D computations under-predict the oscillation amplitudes by 10% of the experimental data. Existing axisymmetric calculations using global chemical mechanism results under-predict the amplitudes by $40\% - 50\%$ of the experimental data. In our work, the pressure oscillation amplitudes are $15 - 20\%$ smaller than the experimental results. All simulations including our work over-predict the oscillation frequencies because of the adiabatic wall boundary condition. On the other hand, our simulation times are at least 50 times less expensive than existing axisymmetric calculations. Spatial mode decomposition in the first harmonic based on the PSD analysis matches existing 3D results very well for the unstable cases. There are half-wave acoustical standing waves found in the combustion chamber. Time-averaged flow fields reveal longer flame lengths for the unstable case compared to the 3D simulations, but a more compact flame compared to existing axisymmetric simulations.

Chapter 4

Instability Mechanisms

In the CVRC experiments, the choked nozzle behaves acoustically similar to a closed end. Therefore, to understand the flame and vortex dynamics under natural oscillations, an additional case following the CVRC experimental setup but with a constant-pressure exit boundary condition is used. The oxidizer-post length for this constant-pressure case is 14 cm. All other parameters such as fuel and oxidizer mass flow rates are kept the same. Therefore, we will only consider three cases: 9-cm post length with choked nozzle outlet (9C), 14-cm post length with choked nozzle outlet (14C), and 14-cm post length with a constant-pressure outlet (14CP). These cases correspond to three different stability domains: stable (14CP), semi-stable (9C), and high-amplitude unstable (14C). The 12-cm post length with the choked nozzle outlet will not be further analyzed since it exhibits similar behavior to case 14C but at a lower pressure amplitude. They are, however, essential characteristics within an unstable cycle. In this chapter, the vortex dynamics and its mixing characteristics across different stability domains are first examined. Comments about the baroclinic torque are made. The pressure and HRR coupling are discussed using the Rayleigh index. Unsteady dynamics between cases are analyzed.

4.1 Vortex dynamics and mixing

Figure 4.1 compares pressure oscillation amplitudes for all three cases. There is a significant drop in pressure oscillation amplitudes from case 14C to 14CP. Case 14CP is qualitatively more stable than case 9C.

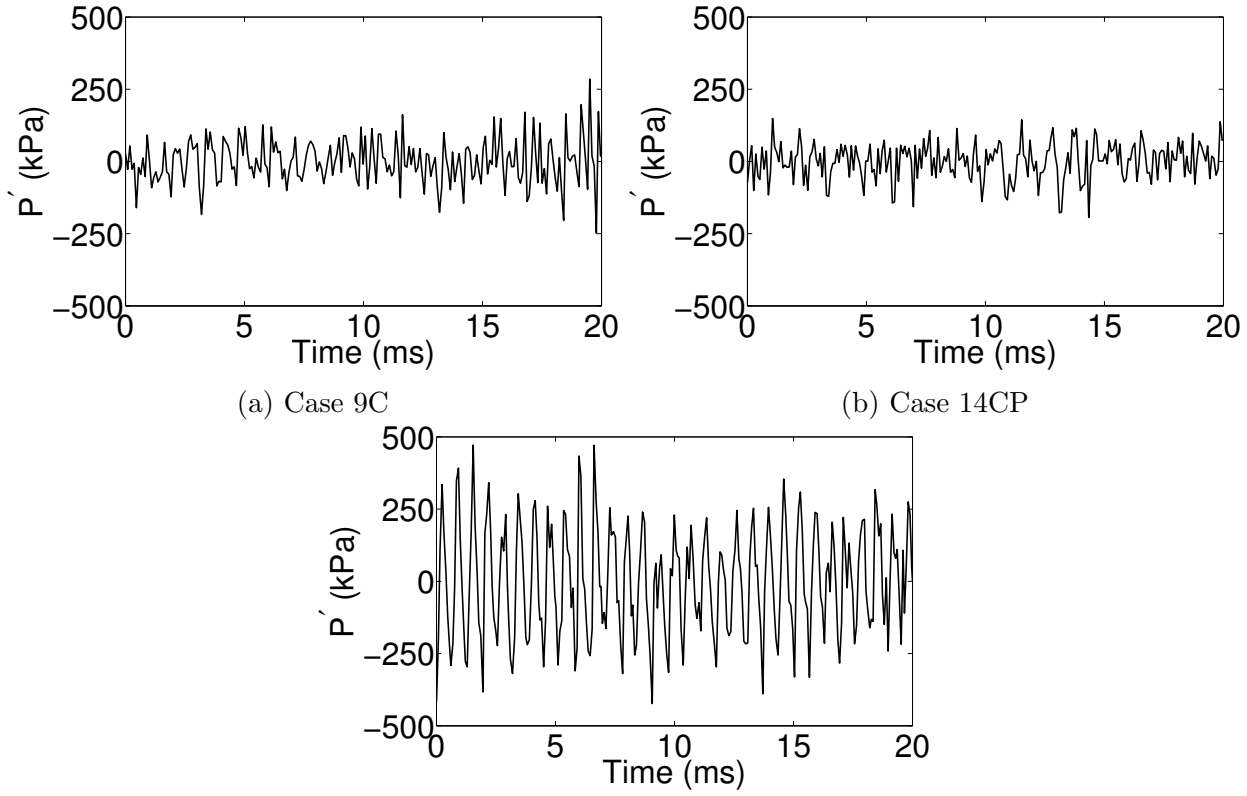

(a) Case 9C

(b) Case 14CP

(c) Case 14C

Figure 4.1: Pressure oscillation amplitude (p') for all three cases at the dump plane in the shear layer.

For case 14CP, the pressure oscillation frequency is 800 Hz. A quarter-wave standing mode is found in the combustion chamber. The dump plane remains a pressure anti-node while the exit is now a pressure node due to the constant pressure exit condition.

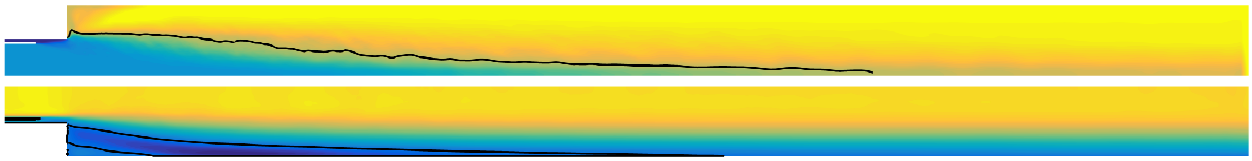

Figure 4.2: Time-averaged temperature and axial velocity for the 14CP case.

As previously found, the flame becomes more compact as the flow becomes more unstable (figures 3.6 and 4.2). An explanation for these measurements can be found from the vortex shedding frequencies. We now consider the Strouhal number, defined as [73] :

$$St = \frac{f_v D}{U} \tag{4.1}$$

where f_v is the vortex shedding frequency. D is the jet flow characteristic length (either oxidizer post and fuel post diameter), U is the main flow axial velocity. The Strouhal number relates to the flow mixedness. The preferred mode Strouhal number, which indicates intense mixing, is between 0.1-0.3 [73] for dump combustor configurations such as the CVRC experimental configuration. In case 14C, vortices are shed at a frequency of 1546.24 Hz. Case 9C has a vortex shedding frequency of 1397 Hz. On the other hand, case 14CP sheds vortices at roughly half of the frequency of its choked counterpart (800 Hz vs. 1546 Hz). Based on these frequencies, the Strouhal numbers are 0.1316, 0.1229, and 0.0878 for cases 14C, 9C, 14CP, respectively. Therefore, the flow in 14CP is not as well mixed as in the choked cases. Furthermore, the higher the Strouhal number in the preferred range, the more likely it will form large coherent vortex structures downstream of the dump plane. This is shown to be true based on the vortex dynamics results shown in figures 4.7, 4.11, 4.15 in chapter 4.

4.2 Baroclinic torque

The next mechanism being studied is the baroclinic torque. The vorticity equation for a general 3D flow is written as

$$\frac{\partial \omega_i}{\partial t} + u_j \frac{\partial \omega_i}{\partial x_j} = -\left(\omega_i \frac{\partial u_j}{\partial x_j}\right) + \epsilon_{ijk} \frac{\partial \rho}{\partial x_j} \frac{\partial p}{\partial x_k} \frac{1}{\rho^2} + \omega_j \frac{\partial u_i}{\partial x_j} + \frac{1}{Re} \frac{\partial^2 \omega_i}{\partial x_j \partial x_i} \tag{4.2}$$

The first term on the right-hand side (RHS) of equation 4.2 is a dilational term that represents the effects of the flow expansion on the vorticity field. The second term is the baroclinic torque. The third term is called vortex tilting or stretching. This term is zero since the flow is axisymmetric. The fourth term is the vorticity diffusion term. For high Reynolds number flow of interest, this term is negligible. Figure 4.3 shows values for three significant vorticity modifying terms left in equation 4.2 at an instance in time for case 14C.

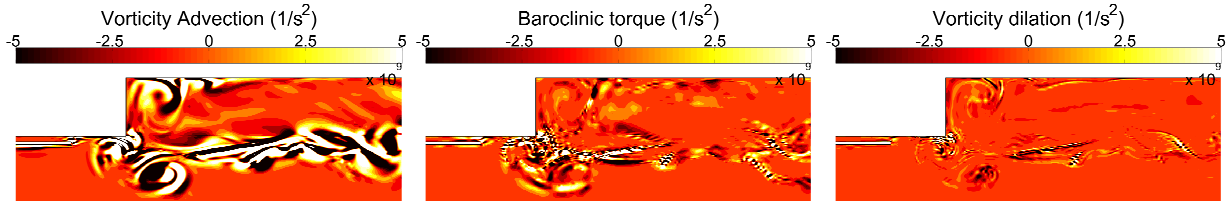

Figure 4.3: The vorticity advection, baroclinic torque, and vorticity dilation for case 14C.

Based on our computations, there is a monotonic increase in baroclinic torque from the stable (14CP) to the semi-stable case (9C) and the unstable case (14C) (not shown). The baroclinic torque, as the cross product between density and pressure gradients, will inherently increase with higher pressure oscillations. Harvazinski et al. [72], while finding similar results to this work, concluded that baroclinic torque is an essential driver in promoting instability. However, as shown in figure 4.3, the vorticity enters with the shear layer flows at the oxidizer and fuel ports, and is advected downstream. Vortex structures form as it flows. That is, vortex shedding occurs at the end of the splitter plate, and the back step in the combustion chamber and these structures are advected downstream. This is also

consistent with cases 9C and 14CP, but not shown here for brevity. Evidently, the vorticity advection term is significantly larger than both the baroclinic torque and vorticity dilation (other researchers have not reported comparisons of various terms in the vorticity evolution equation). Therefore, baroclinic torque is not a significant factor in the vorticity development and the correlation with oscillation should not be misinterpreted. It is a result of the pressure oscillations and the density difference between the fluids rather than a cause of the unstable oscillation. It is noteworthy that our conclusion is only based on axisymmetric calculations, where the effects of vortex-strain interactions such as vortex stretching-tilting are not present. Nevertheless, it should not affect our conclusion that the baroclinic torque is not a significant instability mechanism.

4.3 Heat Release Rate-Pressure Coupling

To understand the interaction between acoustic and flame behavior, the Rayleigh index will be used as a guideline in the following section. The Rayleigh index is a correlation used to determine the locations where the pressure oscillations are being driven or damped by the unsteady heat release rate (HRR). The time-averaged spatially local Rayleigh index [40] is defined as

$$RI = \frac{1}{\tau}\int_{t_o}^{t_o+\tau} \frac{\gamma-1}{\gamma} p'\dot{\omega}' dt \tag{4.3}$$

where p' is the local pressure oscillation and $\dot{\omega}'$ is the local HRR oscillation. Positive Rayleigh index indicates that the unsteady HRR drives the pressure oscillations. Figure 4.4 presents the Rayleigh index results for all three cases. Only half of the combustion chamber is shown in these plots.

Figure 4.4 shows a strong correlation between the pressure oscillations and the HRR around

the recirculation zone for the 14C case as well as the mixing layer immediately after the splitter plate. In case 14CP, a large damping region is observed immediately after the back-step. In the shear layer of the combustion chamber, small instability driven areas are found along with damping regions. Case 9C exhibits behavior which is a combination of both cases 14C and 14CP. A substantial instability driven region is located along the shear layers in the combustion chamber. This region is surrounded by smaller damping regions near the recirculation zone and the centerline. It is noted that the maximum values of the Rayleigh index in cases 9C and 14CP are an order of magnitude smaller than case 14C. This means the unsteady HRR drives the instability more strongly in case 14C compared to case 9C.

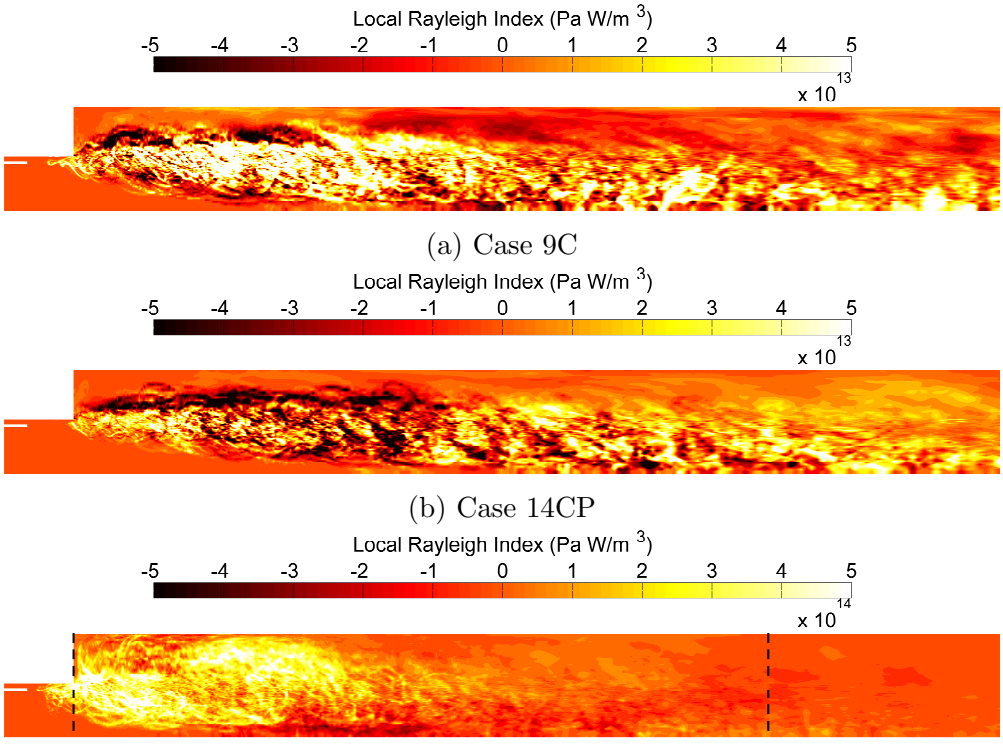

(a) Case 9C

(b) Case 14CP

(c) Case 14C

Figure 4.4: Time-averaged spatially local Rayleigh index.

Based on the flame length calculated and the Rayleigh index analysis, the following analyses will be performed for all three cases focusing on the region enclosed by the dump plane (x=0) and the mean-flame length of case 14C (x=15 cm), as shown by the two vertical broken lines

in figure 4.4c. This region will now be called Volume 1.

4.4 Mechanisms for case 14C

Figure 4.5a shows the volume-averaged HRR and pressure of Volume 1 for case 14C. The volume-averaged method is used to remove any phase-lag bias due to the spatial locality of the pressure signal in Volume 1. As seen in figure 4.5a, the HRR is completely in phase with the pressure oscillation, further confirming our Rayleigh index analysis. Figure 4.5b shows the pressure signal for approximately 2 cycles. There are five circular markers on the plot, identifying the five time instances analyzed in the following discussion. These time instances are called t1 to t5.

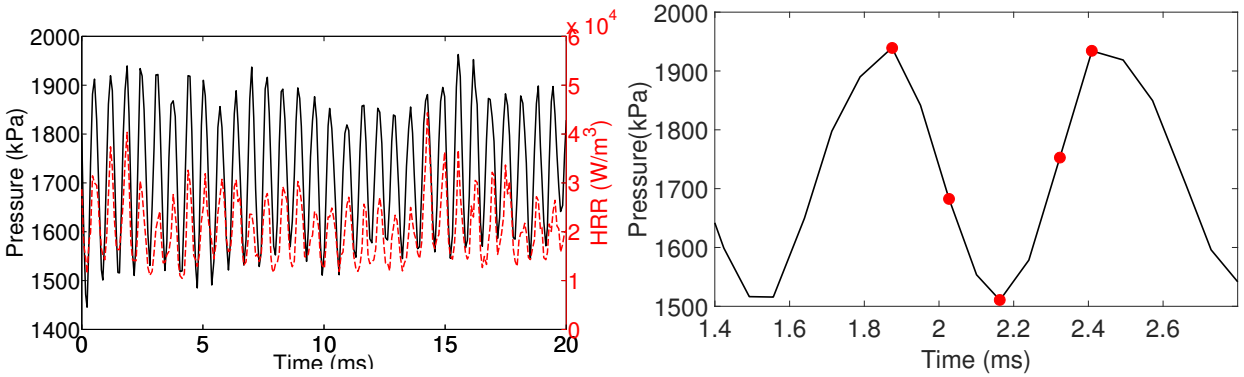

(a) (b)

Figure 4.5: Volume-averaged heat release rate (HRR) and pressure of Volume 1 for case 14C.

Since the dominant pressure waves are longitudinal, the transverse pressure gradients are found to be negligible. Therefore, the pressure field will be best represented as axial functions. Figure 4.6 shows the pressure signal along the centerline at different instances in time marked by the previously described red circles in figure 4.5b. The dump plane is located at $x = 0\ cm$.

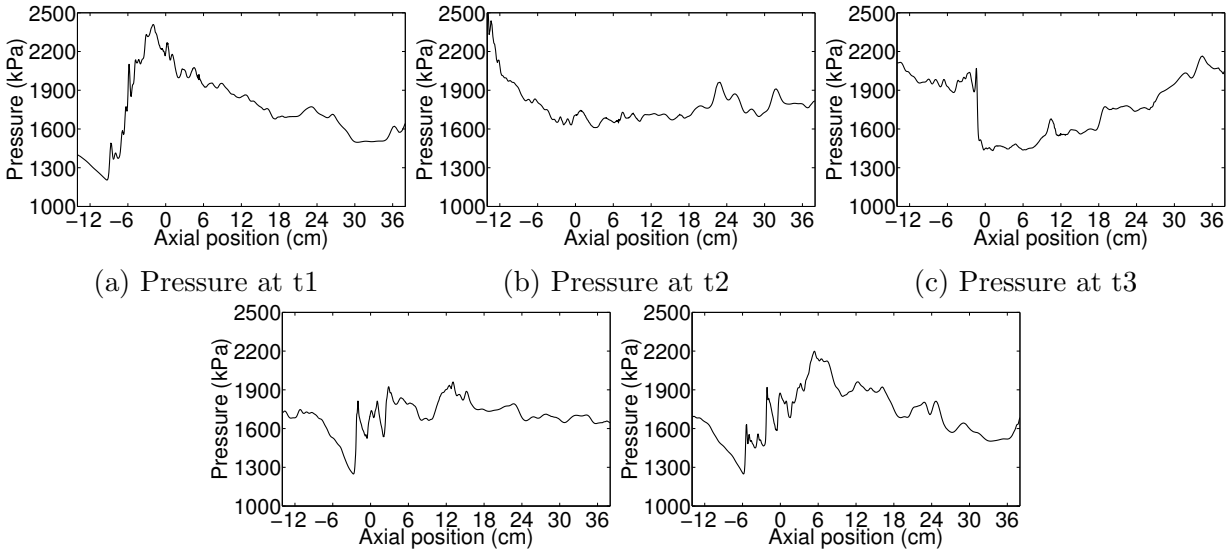

(a) Pressure at t1 (b) Pressure at t2 (c) Pressure at t3

(d) Pressure at t4 (e) Pressure at t5

Figure 4.6: Spatial pressure variation for the entire computational domain for 14C.

Figures 4.7-4.8 show contour plots of the vorticity, HRR, fuel and oxidizer mass fractions for a complete cycle from time t1 to t5 for case 14C. Time is different for each row of sub-figures. These time instances from top to bottom correspond to red circles in figure 4.5b from left to right. The domain shown is from $x = -1.5\ cm$ to $x = 10\ cm$.

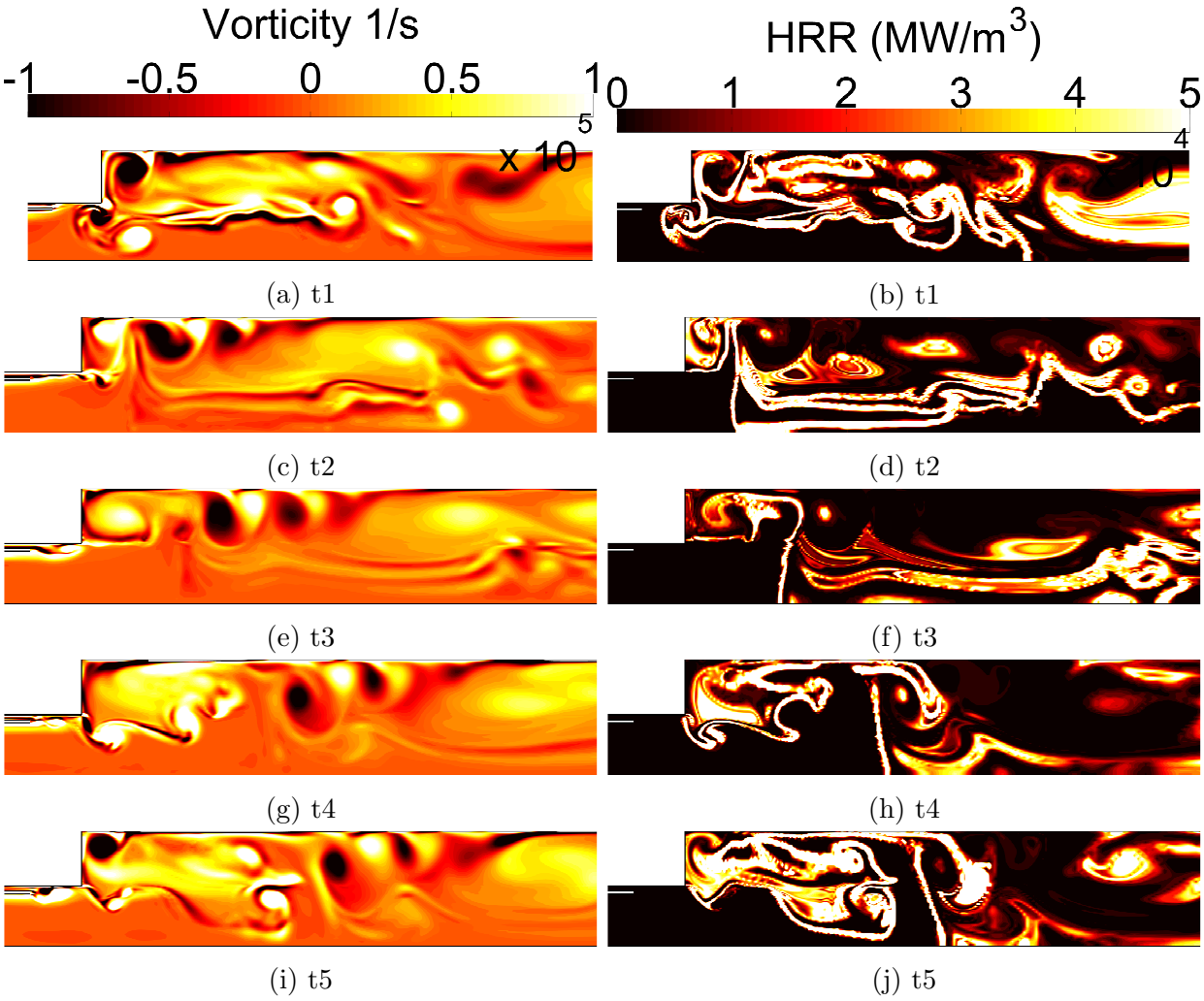

(a) t1 (b) t1

(c) t2 (d) t2

(e) t3 (f) t3

(g) t4 (h) t4

(i) t5 (j) t5

Figure 4.7: Contour plots of vorticity and HRR at different time instances for case 14C.

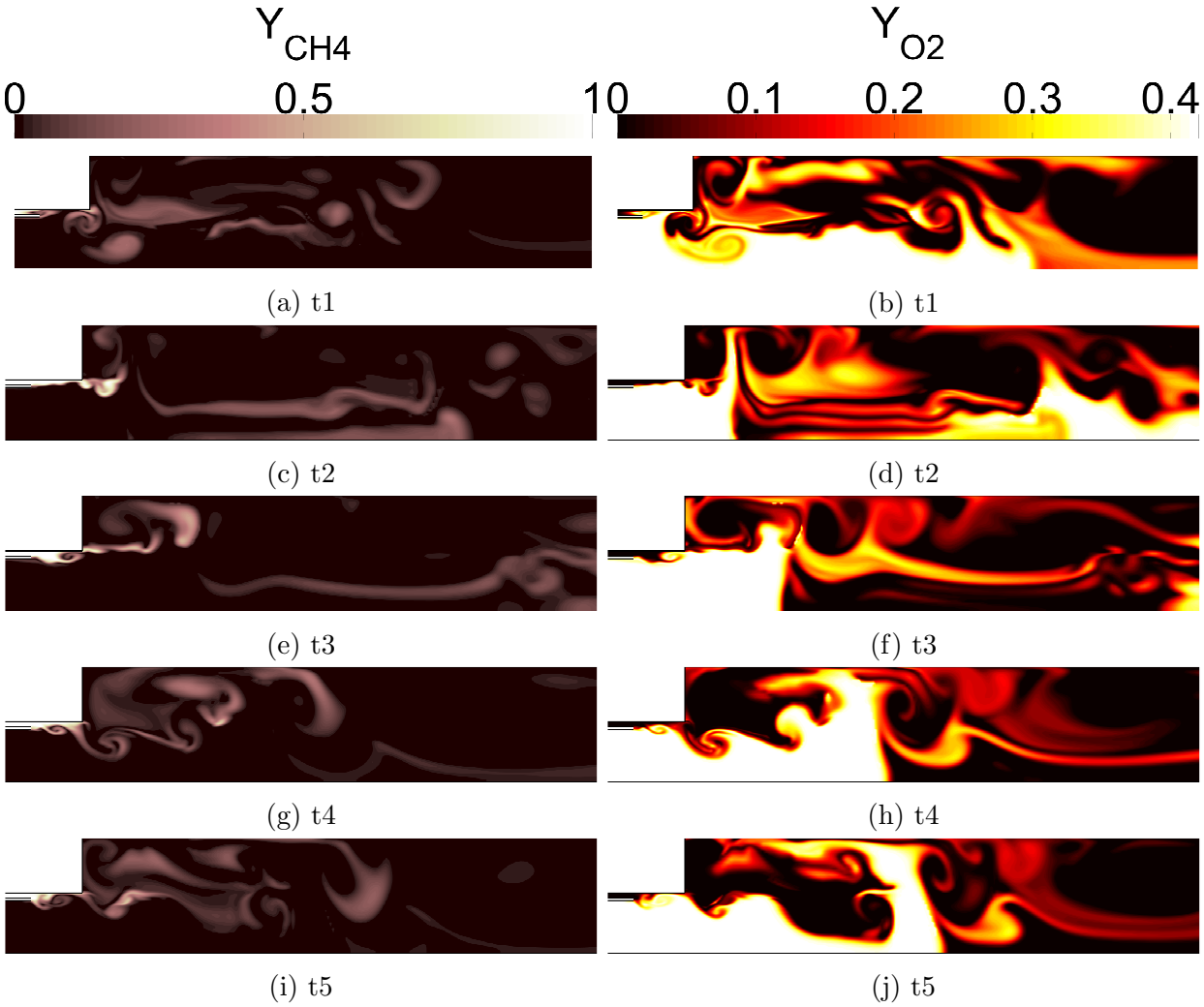

Figure 4.8: Contour plots of the reactants mass fractions at different time instances for case 14C.

The cycle begins at time t1, corresponding to the first pressure peak noted by the first red circle in figure 4.5b. As seen in figure 4.7, most of the reactions happen in the two largest vortex structures, one immediately after the dump plane and one further downstream around x=0.01 m. At this instance, the pressure peaks around the dump plane. These vortex structures enhance turbulent mixing and allow premixed burning to occur inside of these structures while non-premixed burning surrounds them (not shown). In the meantime, there are small vortices shedded along the shear layer after the dump plane; and they carry with them unburnt fuel toward the unburnt oxygen stream along the centerline, as seen in figures

4.7a and 4.8a.

As shown in figures 4.6a-4.6c, a pressure wave traveling downstream from the dump plane (x= 0 cm) toward the combustion chamber exit at t3 and pressure waves moving upstream toward both the inlets of the reactants at t1 are observed. The pressure waves traveling upstream impose an adverse pressure gradient on the reactant streams, disrupting the reactant flow into the combustion chamber. At this instance of time, the adverse pressure gradient is even strong enough to push a mixture of fuel and oxidizer from the splitter plate region into the fuel post, as shown in figures 4.8a-4.8b. At time t2, because of the favorable pressure gradient in the combustion chamber from time t1 (figure 4.6a), the large vortex structures in the recirculation zone are advected further downstream. The previously unburnt reactants along the centerline from time t1 are now ignited, as shown in figure 4.7d. Now, the upstream traveling pressure waves are now reflected from both the inlets, as shown in figure 4.6b, create a favorable pressure gradient that pushed these reactant streams into the combustion chamber. An expanded oxidizer impinging jet is found in all the subsequent time instances because of the reflected downstream running wave at this time instance. Similarly, a large fuel concentration is located around the dump plane due to the favorable pressure gradient.

At time t3, the downstream traveling pressure wave in the oxidizer post is now approaching the splitter plate (x=-10 cm), as seen from figure 4.6c. The favorable pressure gradient in the oxidizer post now accelerates the flow, pushing the accumulated reactants from the mixing layer into the recirculation zone. Meanwhile, an adverse pressure gradient is found in the same recirculation region. This adverse pressure gradient prevents the newly shed vortex structures, which carry the reactants, to move farther downstream.

At time t4, vortex structures shed from the mixing layer continue to merge and form a sizeable coherent structure in the recirculation zone. Due to the formation of the considerable coherent structure, the reactants are allowed sufficient time to be mixed as well as being heated by the hot product gases present in this zone. The increase in reaction rate at time

t4 causes a rise in chamber pressure, specifically in region from the dump plane to x=8 cm. Now, the reflected pressure wave from the chamber exit is approaching the same region, with its peak found at x = 12 cm, as seen from figure 4.6d. This phenomenon creates a syncing/coupling mechanism between the pressure and the HRR, this further promoting combustion instability.

At time t5, the mixture in the recirculation zone finally combusts, creating large separated pressure waves traveling upstream of the reactant posts as well as downstream of the combustion chamber. The cycle is now poised to repeat itself. It is noteworthy the adverse pressure gradient imposed by the upstream traveling waves is not as large the one found at t1, as shown in figure 4.6e. This means the mixture found at the splitter plate cannot travel upstream of the fuel post, as shown in figures 4.8i-4.8j.

4.5 Mechanism for case 9C

Figure 4.9a shows the volume-averaged HRR and pressure of Volume 1 for case 9C. The HRR, in this case, is intermittently in phase with the pressure oscillations, further confirming its semi-stable classification in which the oscillation amplitudes never reach a limit cycle behavior. Therefore, the following analysis is not truly a cycle analysis, but a description of the oscillatory behavior in this case. The red circles in figure 4.9b denotes the 5 time instances described by figures 4.10-4.11.

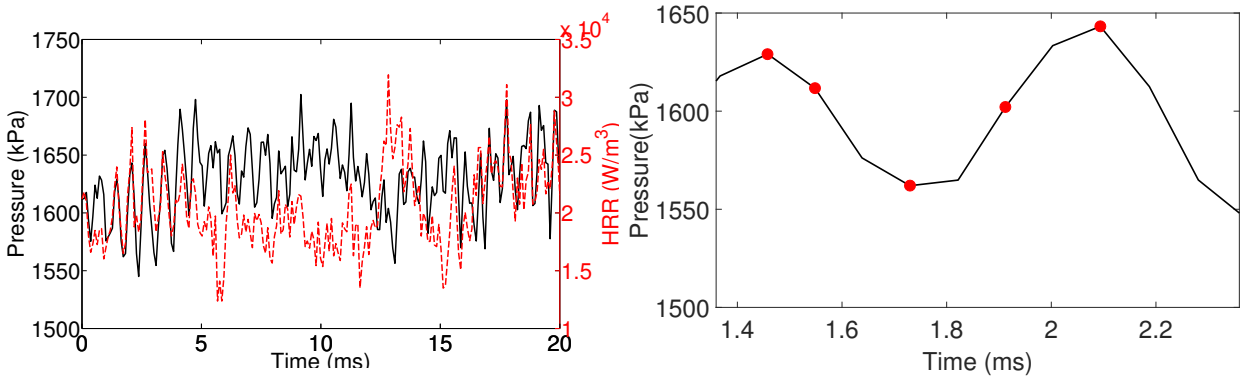

(a) (b)

Figure 4.9: Volume-averaged HRR and pressure of Volume 1 for case 9C.

Similar to case 14C, the pressure field in the computational domain is presented as a one-dimensional function in the axial direction, as shown in figure 4.10.

Figures 4.11-4.12 show contour plots of the vorticity, HRR, fuel, and oxygen mass fractions at various time instances. The domain shown in these plots is the same as in figures 4.7-4.8.

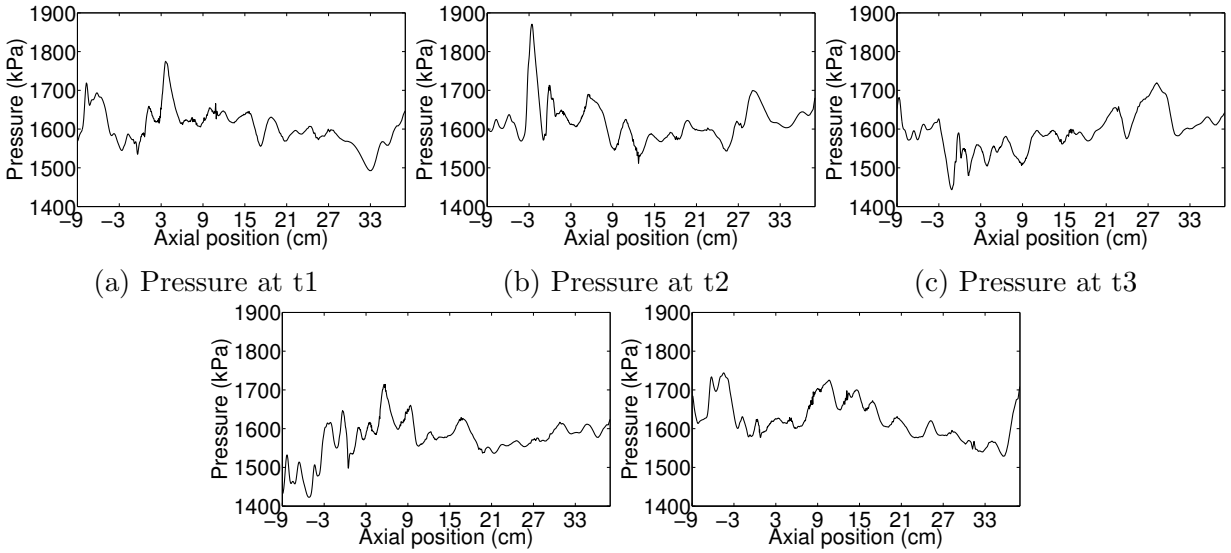

(a) Pressure at t1 (b) Pressure at t2 (c) Pressure at t3

(d) Pressure at t4 (e) Pressure at t5

Figure 4.10: Spatial pressure variation for the entire computational domain for case 9C.

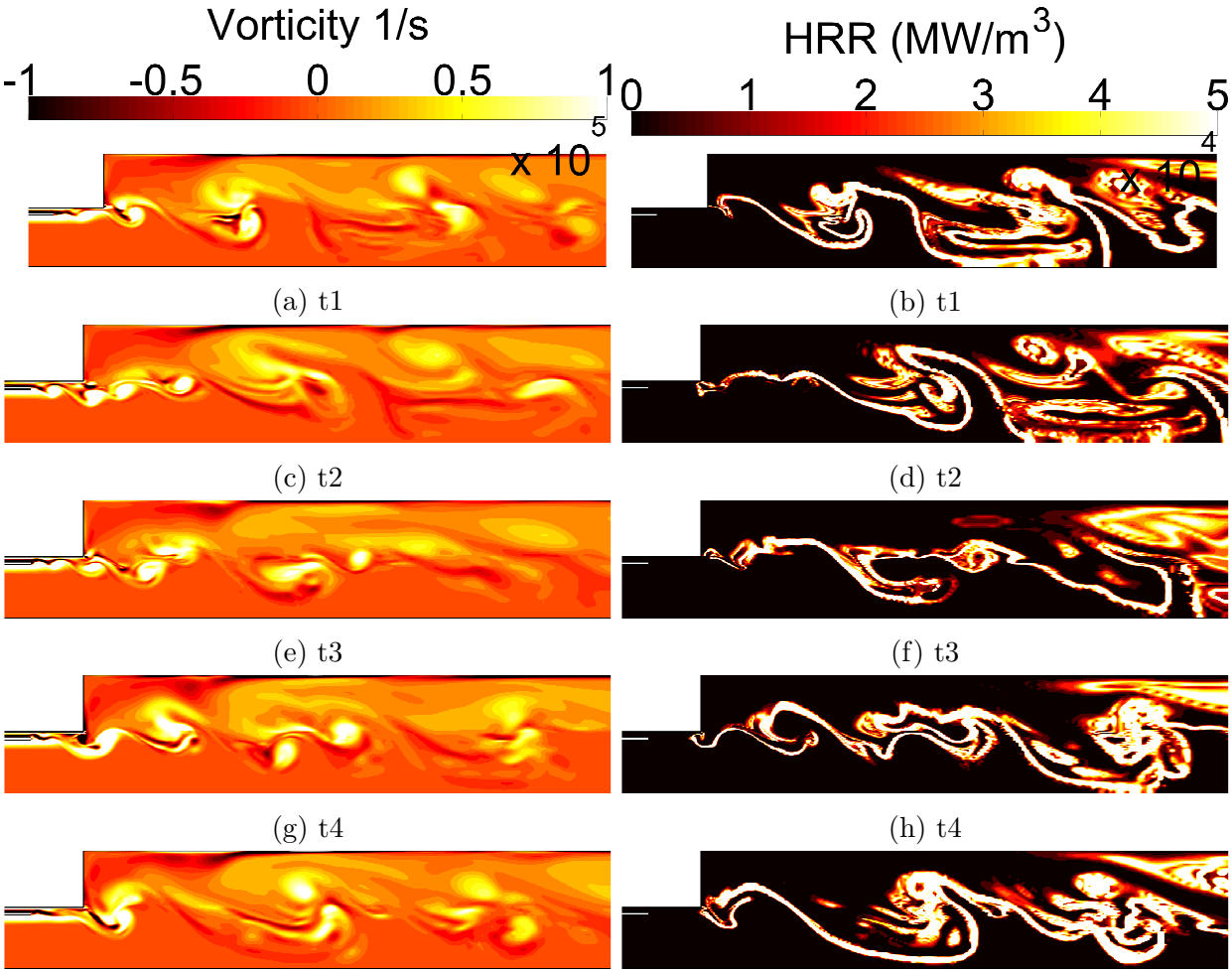

(a) t1 (b) t1

(c) t2 (d) t2

(e) t3 (f) t3

(g) t4 (h) t4

(i) t5 (j) t5

Figure 4.11: Contour plots vorticity and HRR at different time instances for case 9C.

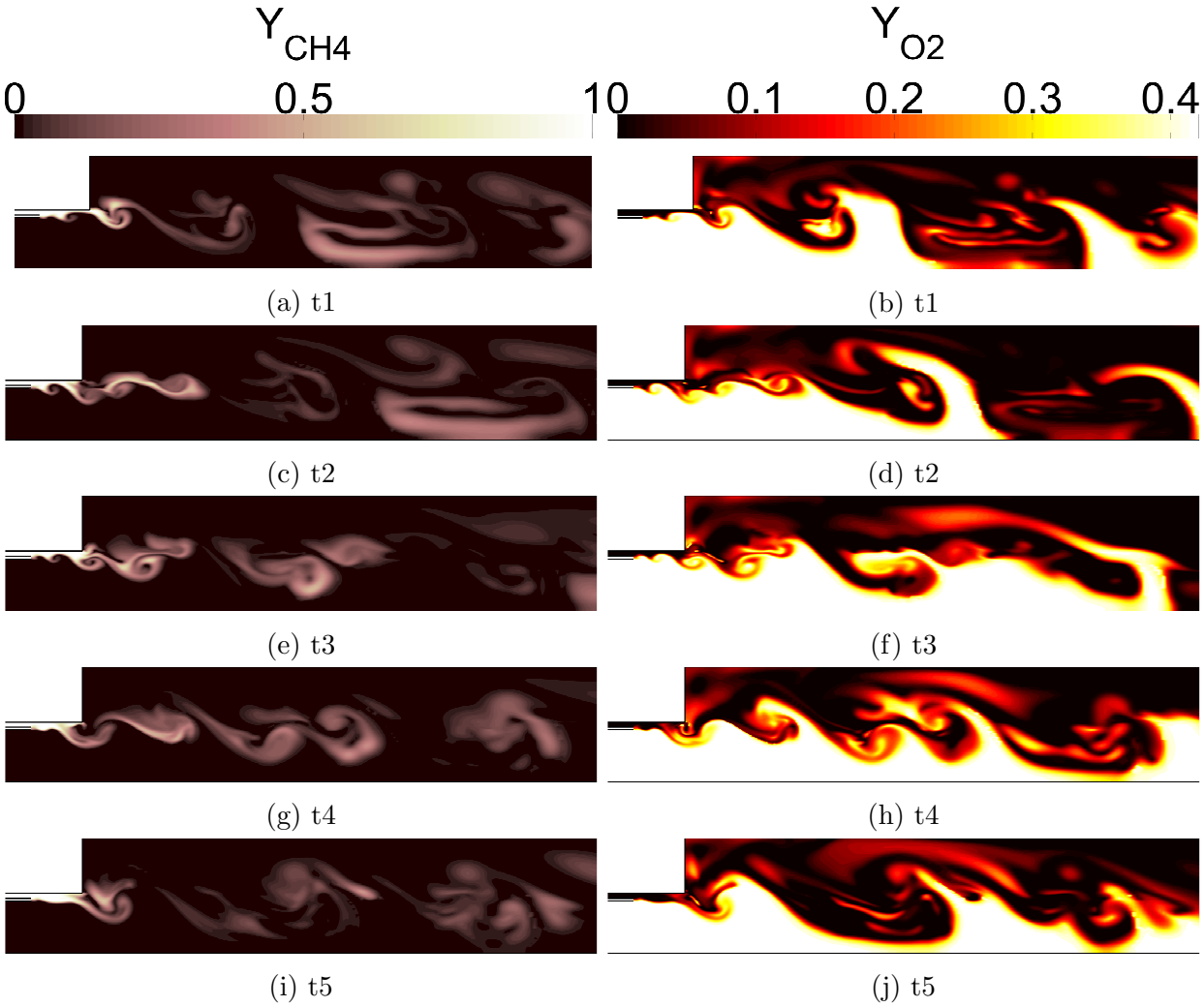

Figure 4.12: Contour plots of reactants mass fractions at different time instances for case 9C.

The first distinctive feature in case 9C compared to case 14C is the lack of vortex merging phenomena occurring immediately downstream of the back step. Instead, smaller vortex structures are shed and advected downstream immediately. The vortex merging occurs further downstream from the dump plane, creating a lumped reaction zone similar to the one found in the recirculation zone in case 14C. A long, thin reaction zone occurs within the shear layer immediately downstream of the back step. Comparing the pressure contour plots between time t1 and t2 in figure 4.10, there is clearly again a left-running pressure wave propagating toward the oxidizer inlet. However, these pressure gradients are not strong

enough to cause a disruption in reactants flow compared to case 14C. Instead, these pressure gradients simply push the fuel against the horizontal wall before the back step, temporarily hindering the reactants mixing. Stronger premixed burning is found in the recirculation zone at the peak of the pressure oscillation compared to its trough (not shown).

4.6 Mechanism for case 14CP

Figure 4.13a shows the volume-averaged heat release rate (HRR) and pressure of Volume 1 for case 14CP. The HRR in this case is completely out of phase with the pressure oscillations. The red circles in figure 4.13b denote the four time instances described by figures 4.14-4.15.

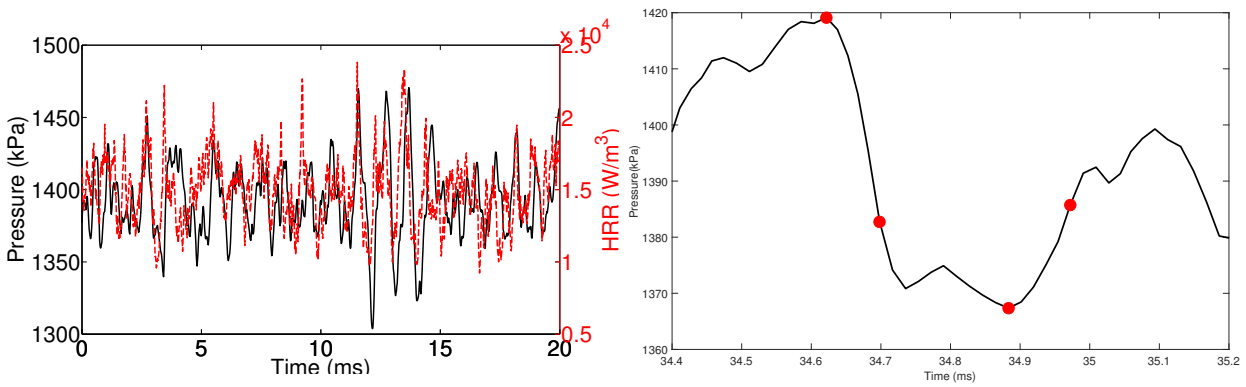

(a) (b)

Figure 4.13: Volume-averaged heat release rate (HRR) and pressure of Volume 1 for case 14CP.

Figure 4.14 shows the pressure field in the computational domain as a one-dimensional axial function. Each of the sub-figures corresponds to different instances in time marked by the red circle in figure 4.13b.

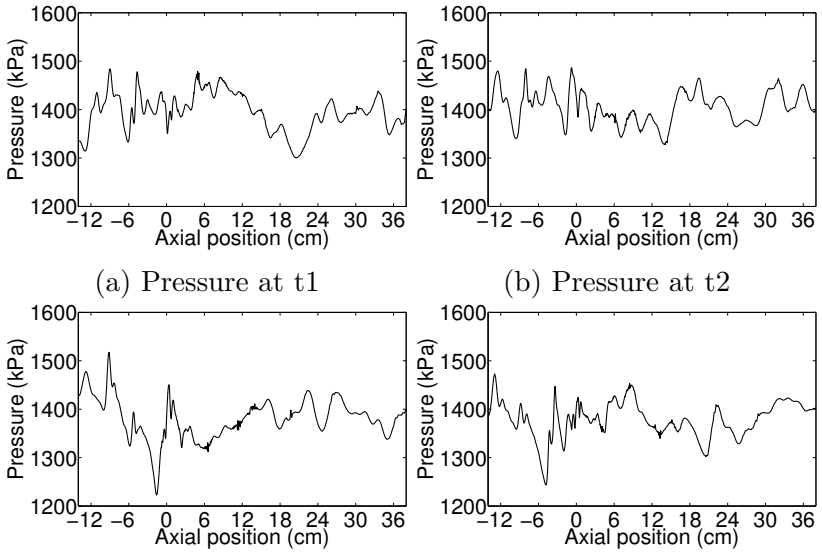

(a) Pressure at t1 (b) Pressure at t2

(c) Pressure at t3 (d) Pressure at t4

Figure 4.14: Spatial pressure variation for the entire computational domain for case 14CP.

Figures 4.15-4.16 shows contour plots of the vorticity, HRR, fuel and oxygen mass fractions at various time instances on the same domain as figures 4.11-4.12.

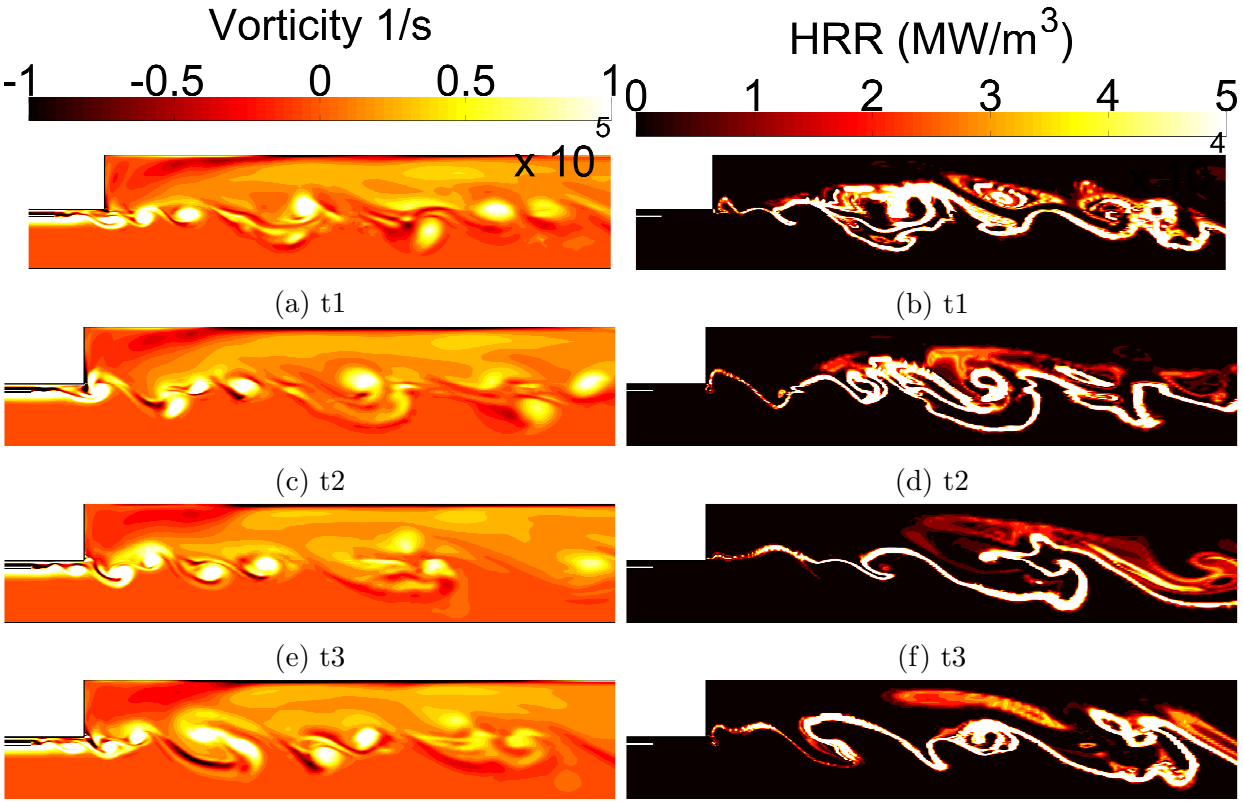

(a) t1 (b) t1

(c) t2 (d) t2

(e) t3 (f) t3

(g) t4 (h) t4

Figure 4.15: Contour plots of vorticity and HRR at different time instances for case 14CP.

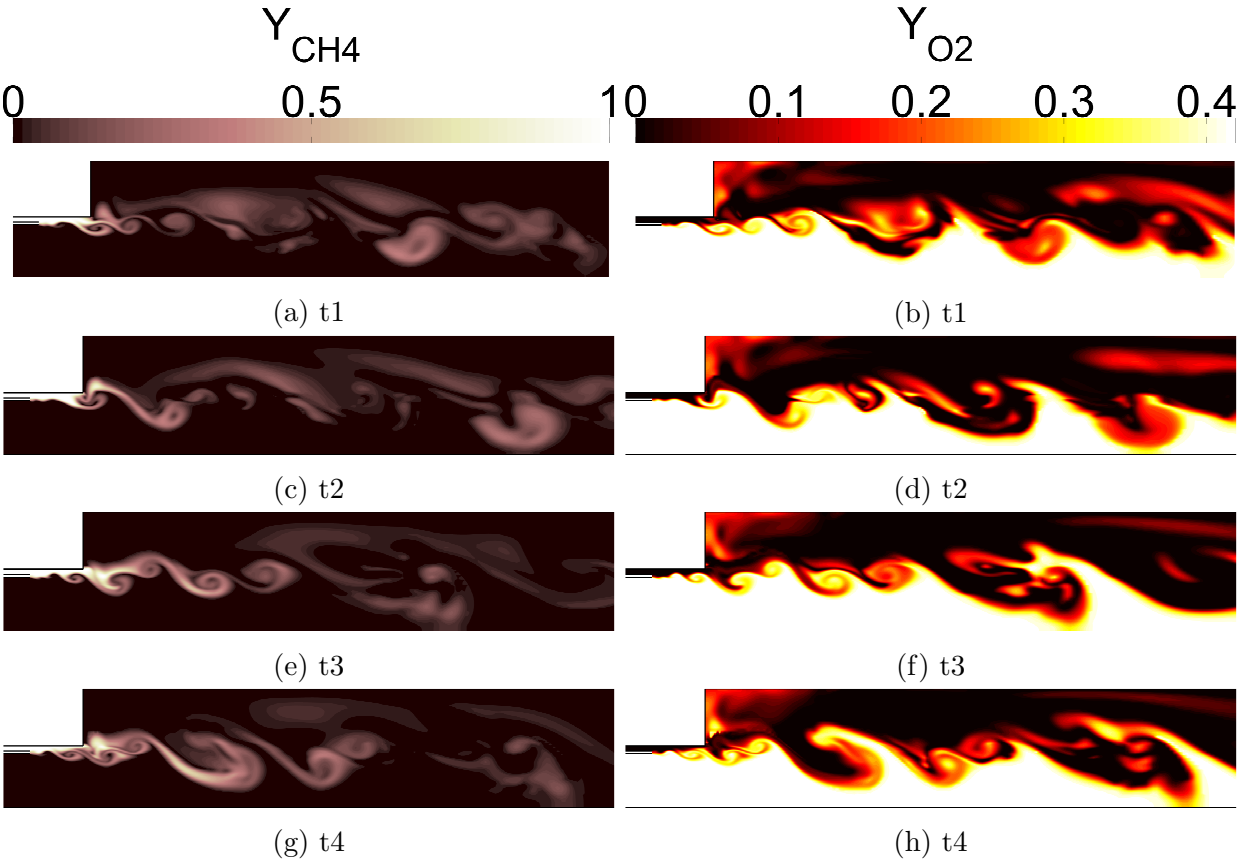

(a) t1 (b) t1

(c) t2 (d) t2

(e) t3 (f) t3

(g) t4 (h) t4

Figure 4.16: Contour plots of reactants mass fractions at different time instances for case 14CP.

In this case, there is no distinctive vortex merging pattern. Therefore, the lumped reaction zones present in case 14C and to a degree in case 9C are not found in this case. Instead, the vortex structures shed in the shear layer immediately after the back step are simply advected downstream. These vortex structures simply carry the reactants downstream until sufficient mixing is achieved and the mixture combusts. Therefore, most of the reactions can be found within the shear layer.

4.7 Concluding Remarks

Comparing to chapter 3, an additional simulation is performed using an open-end exit boundary condition for the 14-cm oxidizer post length. Comparisons are made with a semi-stable case (9C) and completely unstable case (14C). In the 14C case, the Rayleigh-index analysis reveals a strong correlation between the pressure fluctuations and the heat release rate around the upstream pressure anti-node in the chamber, causing a destabilizing effect in the chamber. In the semi-stable and stable cases, strong correlations between the pressure oscillations and heat release rates can only be found around mixing shear layers. Cycle-to-cycle analyses further confirm the Rayleigh-index findings. In case 14C, highly intense (lumped) reaction zones are found near the dump plane (pressure anti-node). In case 9C, these lumped reaction zones move further away from the dump plane and closer to the pressure node. This phenomenon has a stabilizing effect on the combustion chamber. In case 14CP, no lumped reaction zones are found.

Chapter 5

Flame Dynamics

The majority of the existing research utilizing the flamelet approach has concentrated in simulations of flames in the incompressible limit [74–76]. In the compressible limit, the CFPV approach has only been studied in supersonic and hypersonic combustion [62–64]. Therefore, this chapter explores the flame dynamics of the CVRC experiment, which is classified as subsonic compressible combustion. Moreover, flame dynamics, under nonlinear pressure oscillation, has never been analyzed by using the flamelet concept. Representing the flamelet solutions, as obtained in section 2.4.5, by their maximum temperature and χ_{st} resulting in an S-curve, as shown in figure 5.1a

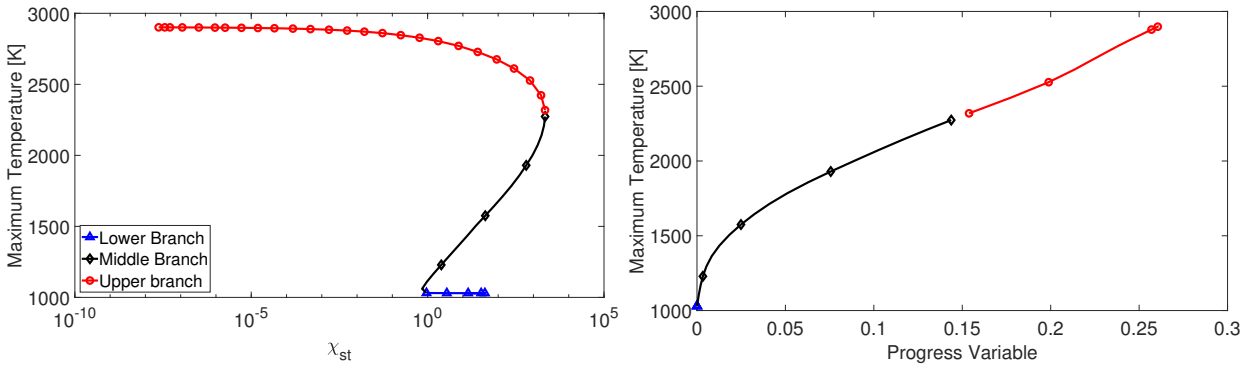

(a) S-shaped curve (b)

Figure 5.1: S-curve results for the present reactants.

This S-shaped curve illustrates the nature of diffusion flamelets. Each scalar dissipation rate could have multiple solutions; it is thus not a well-defined function (figure 5.1a). The upper branch describes stable burning solutions (curve with circle markers). The lower branch (horizontal line with triangle markers) describes non-burning solutions. The middle branch (line with diamond markers) shows the unstable burning solutions. The traditional diffusion flamelets approach of Peters [46] can only cover the upper branch. The Flamelet Progress Variable (FPV) approach, first introduced by Pierce and Moin [61], can cover all three branches because all the relevant quantities (e.g., maximum temperature) become monotonic functions of the progress variable (C) (figure 5.1b). The importance of utilizing the whole S-curve in predicting the correct instability behavior is explored in this chapter. Additionally, the flamelet extinction and reignition behaviors under different stability regimes are examined. Finally, discussion regarding the combustion model ability to simulate partially premixed flame characteristic is presented.

5.1 Flamelet Structures

Figure 5.2a shows different temperature solutions along the S-curve. When the mixture fraction is zero, the flow is solely composed of oxidizer. When the mixture fraction is one, the flow is solely composed of fuel. Therefore, the left boundary of all the temperature curves is always 1030 K, and their right boundary is 300 K. The bottom curve represents mixing branch. The next six curves above it represent unstable flamelet burning solutions, along the middle branch of the S-curve. These solutions are classified as unstable due to their sensitivity to small perturbations by moving either toward the stable upper branch or a stable quenched solution [74]. The top 3 curves represent stable flamelet burning solutions.

Figure 5.2b shows the maximum HRR as functions of the progress variable at different

pressures. In these figures, the total HRR rate for n number of species is defined as

$$HRR = -\sum_{k=1}^{n} \dot{\omega}_k h_k \tag{5.1}$$

where $\dot{\omega}_k$ is the mass reaction rate per unit volume ($kg/m^3 s$) of the k species. h_k is the species enthalpy (J/kg), which also includes the enthalpy of formation. Depending on the pressure, the progress variable values at extinction are from 0.145-0.155. Pressure effects on the flame can be observed from figure 5.2b. Since the Dirac delta function is the marginal PDF for pressure, the mean pressure ($\bar{p}$) is the same as the background pressure in the flamelet solutions. Using this fact along with figure 5.2b, the coupling relationship between the pressure and HRR can now be observed. As the pressure increases, the HRR increases as there is more mass per unit volume to burn. Admittedly the effect of using the Dirac delta function for the pressure remains somewhat ambiguous. However, by using equation 2.32 to obtain the mean temperature and to solve for the full Navier-Stokes equations, we allow the pressure waves to propagate independently (to a certain extent) from the flamelet model.

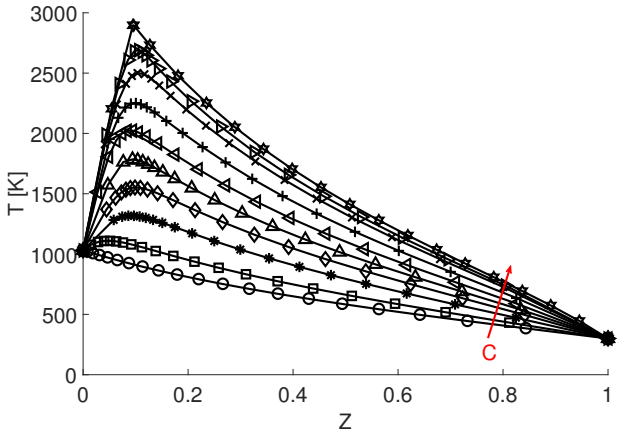

(a) Temperature as functions of the mixture fraction at various progress variable values at p= 18 atm.

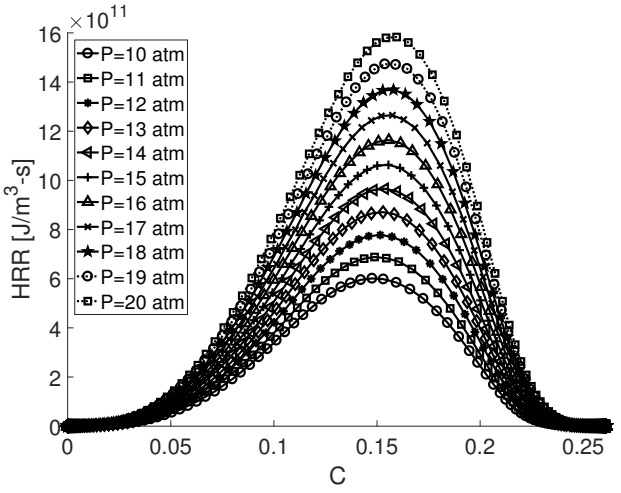

(b) Maximum HRR as functions of the progress variable at different pressure values.

Figure 5.2: Representative flamelet solutions for the entire S-curve.

Figure 5.3 shows two different flamelet solutions for approximately the same reference stoichiometric dissipation rate near the quenching limit. The left column represents an unstable flamelet burning solution while the right column represents a stable flamelet burning solution. The top row shows the HRR as well as the HRR by major species. The bottom row shows major species mass fractions as well as the temperature profile. The region enclosed by the vertical lines is the approximated oxidation layer [77]. The right vertical lines mark the stoichiometric mixture fraction.

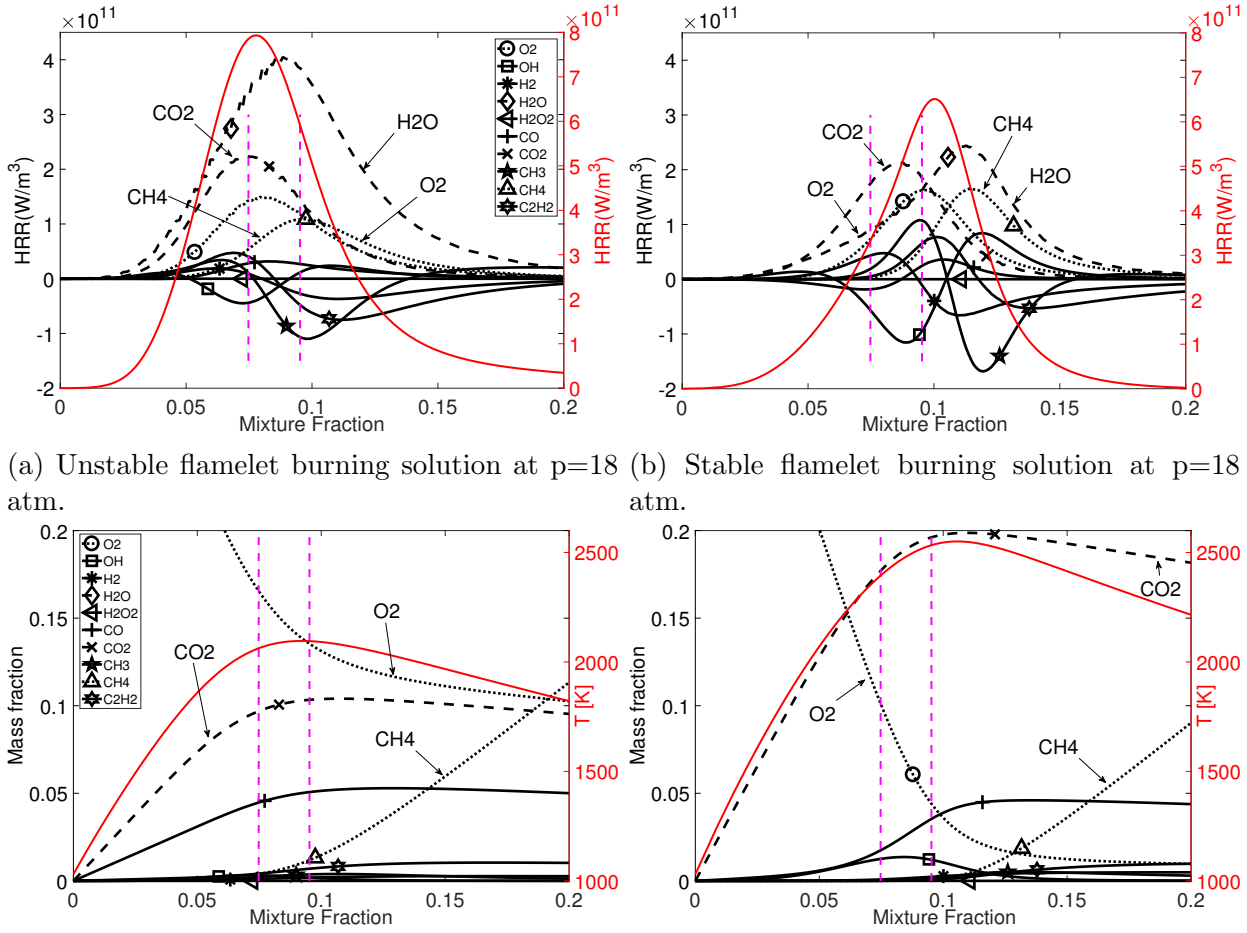

(a) Unstable flamelet burning solution at p=18 atm.

(b) Stable flamelet burning solution at p=18 atm.

(c) Unstable flamlet burning solution at p=18 atm.

(d) Stable flamelet burning solution at p=18 atm.

Figure 5.3: Major species reaction rates, temperature, and HRR as functions of the mixture fraction.

In the unstable flamelet burning limit, the most intense HRR region locates within the

oxidation layer on the fuel-lean side 5.3a. This region is dominated by the secondary reactions involving H_2O and CO_2. In the stable flamelet burning limit, however, the HRR region is located on the fuel-rich side, slightly to the right of the stoichiometric line. Reactions in this branch are much more stable, with the consumption of CH_4 accounting for a larger fraction of the total HRR. In both cases, due to high scalar dissipation rates in the reaction zone (small characteristic diffusion time), there is considerable reactant leakage through the reaction zone, as shown in figures 5.3c-5.3d. In the stable burning case, oxygen is consumed faster across the oxidation layer, thus leading to less oxygen leakage to the fuel-rich side. The flame structures described above are similar to findings by Seshadri and Peters [77] for methane-air diffusion flame.

5.2 Flame Extinctions and Reignition

There are three separated cases considered in this chapter. The first two cases are the 14C and 9C, as reported in chapter 4. These cases represent unstable and semi-stable pressure oscillations. Because the objective of this chapter is to study the flame/acoustic interactions at different stability limit, case 14CP in chapter 4 is not chosen since there is no wave reflection at the exit. Instead, the third case has a 17-cm oxidizer post and 30-cm chamber configuration. The choked nozzle boundary condition is applied in this case. Figure 5.4 shows the oscillatory behaviors and first-longitudinal-mode shape for all cases considered in this chapter. The peak-to-peak oscillation amplitude is around 80 kPa, which is about 5% of mean chamber pressure (P=1540 kPa). The 17-cm case is therefore classified as stable. Further analysis of this case is given in chapter 6.

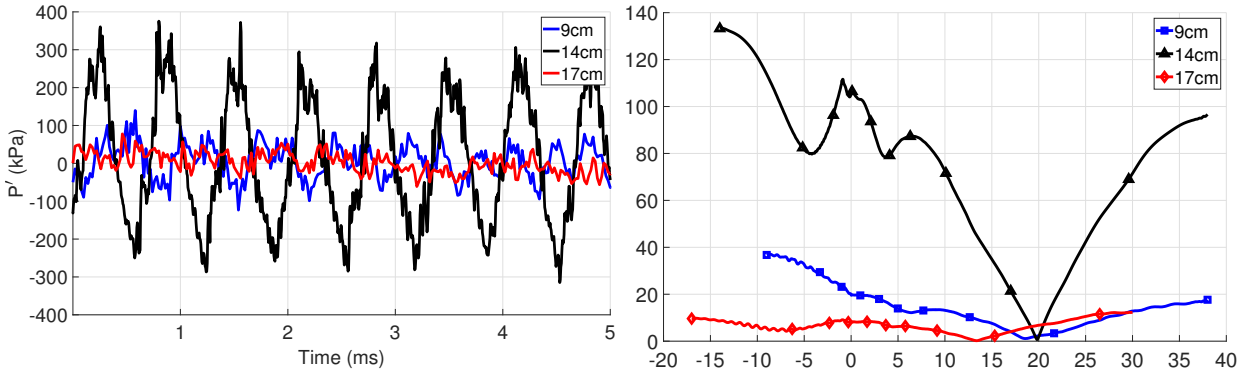

(a) Pressure oscillations for all cases.

(b) Mode shape.

Figure 5.4: Pressure oscillation behavior and first longitudinal-mode-shape for the 14-cm oxidizer post case.

Figure 5.5 illustrates the local ignition and extinction effects for the 14-cm case. The white isocontour lines represent the stoichiometric mixture fraction value ($\tilde{Z}_{st} = 0.095$). Only the region between the splitter plate and the combustor dump plane is shown here. The spatial vectors are plotted in millimeter. Four random probes are placed in each figure. These probes are now numbered I to IV following from left to right and counterclockwise direction. Therefore, probe I is located at ($x = -6.6\ mm$, $r = 8.9\ mm$) and probe IV is located at ($x = -2.6\ mm$, $r = 10.2\ mm$). Local extinctions and reignitions are observed by following the transient behavior probe I. At time t1 (first row of figure 5.5), probe I is fuel-rich ($\tilde{Z} = 0.27$). Moderately burning ($HRR = 164\ GJ/m^3s$) occurs in the unstable flamelet burning branch ($\tilde{C} = 0.14 < 0.16$). At time t2 (second row), the location is fully burning on the stable branch. The HRR increases by a factor of three while the fuel-rich mixture is still maintained. At time t3 (the third row), while the local flow composition remains relatively the same compared to time t2, the flame is locally extinct with its HRR decreased by a factor of 10. Further examination shows an increase in the Favre-averaged scalar dissipation rate ($\tilde{\chi}$) at this probe from time t2 to t3 (from 4251 $1/s$ to 7776 $1/s$). Thus the flame is extinguished. For similar values of $\tilde{Z}$ and C, the increase in the mean scalar dissipation rate is caused by the decrease in the mean mixture variance, mainly through the transport of the $\widetilde{Z^2}$ equation.

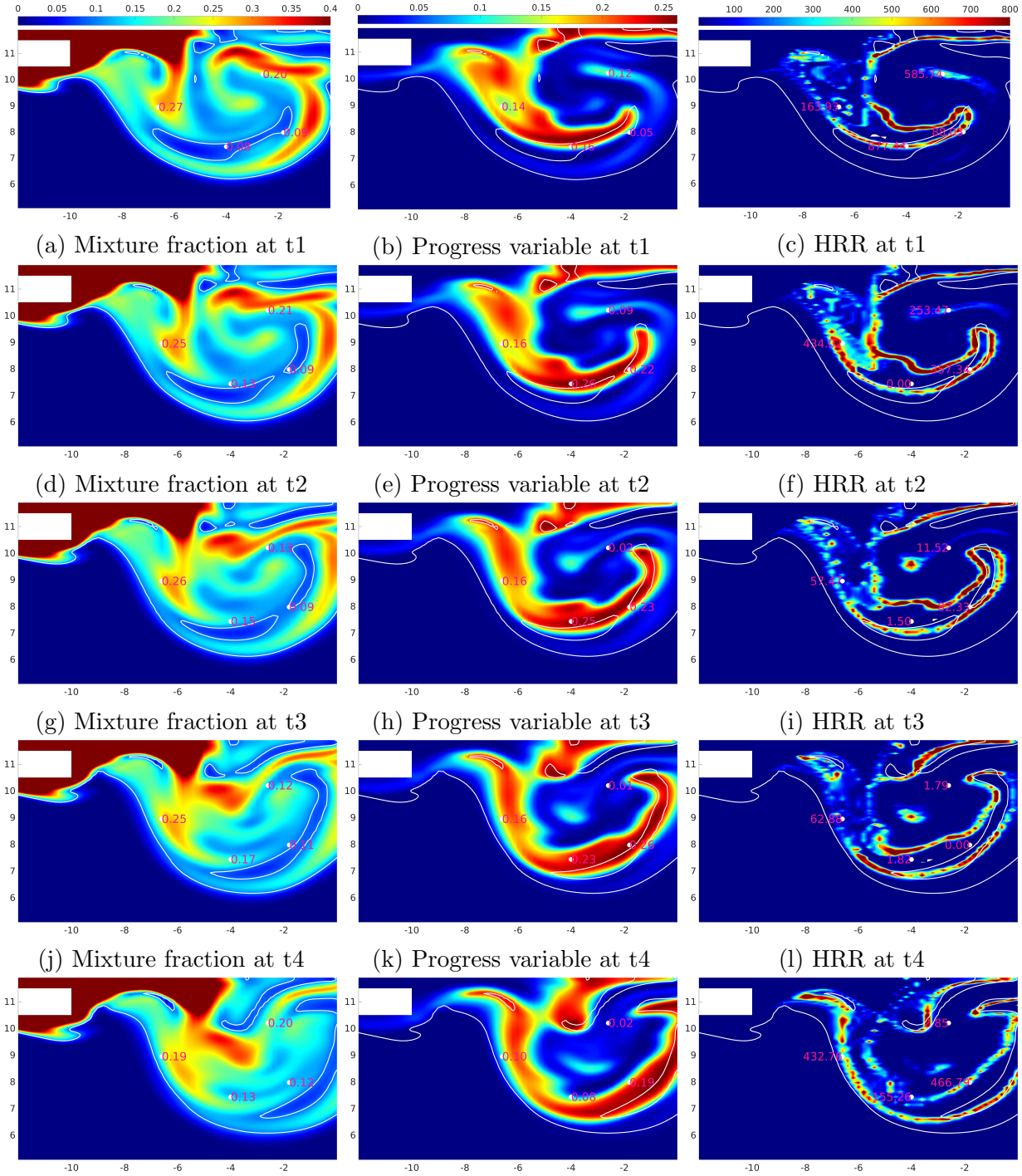

(a) Mixture fraction at t1 (b) Progress variable at t1 (c) HRR at t1

(d) Mixture fraction at t2 (e) Progress variable at t2 (f) HRR at t2

(g) Mixture fraction at t3 (h) Progress variable at t3 (i) HRR at t3

(j) Mixture fraction at t4 (k) Progress variable at t4 (l) HRR at t4

(m) Mixture fraction at t5 (n) Progress variable at t5 (o) HRR at t5

Figure 5.5: Unsteady behaviors of different flow variables subjected to an adverse pressure gradients during the peak of the unstable pressure oscillation. Each time frame is separated by 5 microseconds. HRR has a unit of GJ/m^3s.

At time t5 and still following probe I, the flame is now locally ignited, but burning in the

unstable burning branch ($\tilde{C} = 0.10 < 0.16$). The $\tilde{Z}$ value significantly decreases from time t4 to t5 due to the propagation of the unburnt reactant mixtures.

Following probe II, at time t1, the flame is substantially fuel-lean ($\tilde{Z} = 0.08$) even though it is burning in the stable flamelet burning branch. Due to its fuel-lean structure, the flame burns in a very short time ($\tilde{C} = 0.16$ to $\tilde{C} = 0.26$). A small flame burning on the fuel-rich side in the unstable flamelet burning branch is found at this location at time t5. At time t1 for probe IV, a small, intense flame (hotspot) is found burning in the unstable flamelet burning branch. This hot spot continuously burns for at least 15 microseconds as it moves to the center of the roll-up vortex.

Examination beyond time t5 reveals that once the left-running pressure wave passes toward the oxidizer inlet upstream of the splitter plate, the roll-up vortex moves significantly faster downstream toward the combustion chamber. The flame in the region shown in figure 5.5 burns weakly and is mostly diffusion controlled, as shown in figure 5.6 which is 50 microseconds later than time t5.

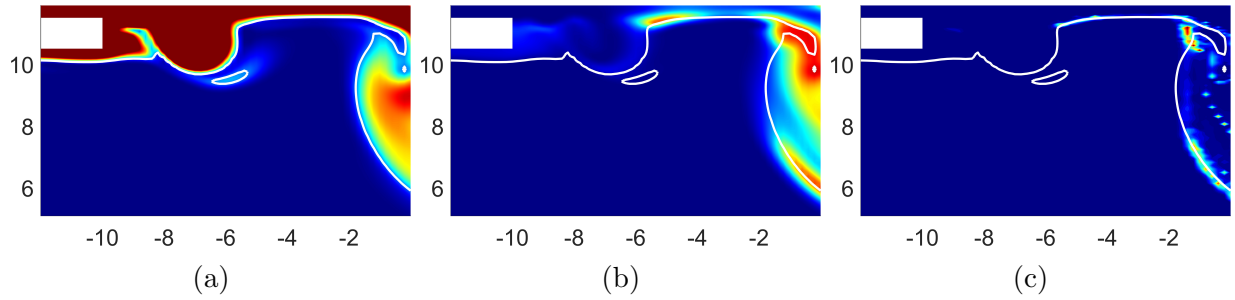

Figure 5.6: Contour plots of the mean mixture fractions (left column), the progress variable (middle column), and the HRR (right column) subjected to a favorable pressure gradient during the trough of the unstable pressure oscillation. The same scales are used when compared to figure 5.5.

To further illustrate the importance of utilizing the whole S-curve in the calculation, an additional simulation of the 14-cm case is performed. While the full flamelet equations are solved, the progress variable values are limited to above 0.16, preventing the flame from

reaching the extinction scalar dissipation rates. The flame in this case, therefore, can only burn in the stable flamelet burning branch. This approach is similar to the Steady Laminar Flamelet Model [46]. The peak-to-peak pressure oscillation amplitude is 200-250 kPa, which is roughly one-third of the amplitude predicted when the full S-curve is allowed, as shown in figure 5.7. In comparison, the experimental peak-to-peak magnitude is 750 kPa for this case. This pressure oscillation amplitude matches well with calculations in Pant *et al.* [78] using the Steady Laminar Flamelet Model.

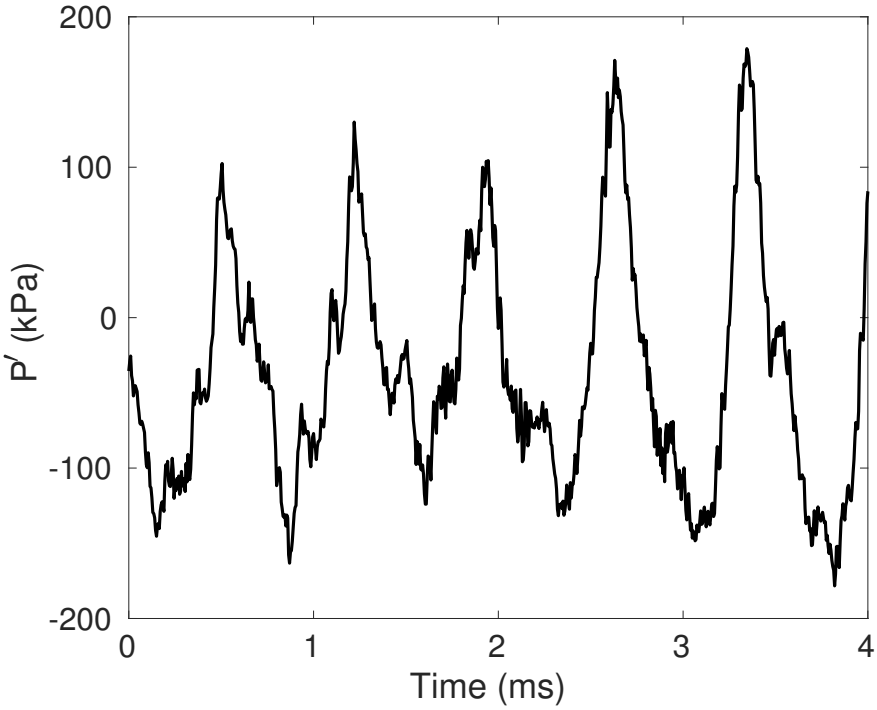

Figure 5.7: Pressure signal on the combustion chamber wall at x= 37 cm for the steady flamelet simulation.

The flame, in this case, is much cooler compared to the full S-curve simulation, as seen in figure 5.8c. The flame is strongly attached to the splitter plate regardless of whether favorable or adverse pressure gradients are imposed on the flow. Similar phenomena are observed for a coaxial combustor simulation using the steady laminar flamelet approach [61]. The lack of local extinctions and reignitions also means the flame front cannot be lifted and reattached as seen when the full S-curve is allowed. The Rayleigh index analysis in this

case (figure 5.8d) reveals a significant reduction in pressure-HRR coupling around the dump plane (pressure anti-node).

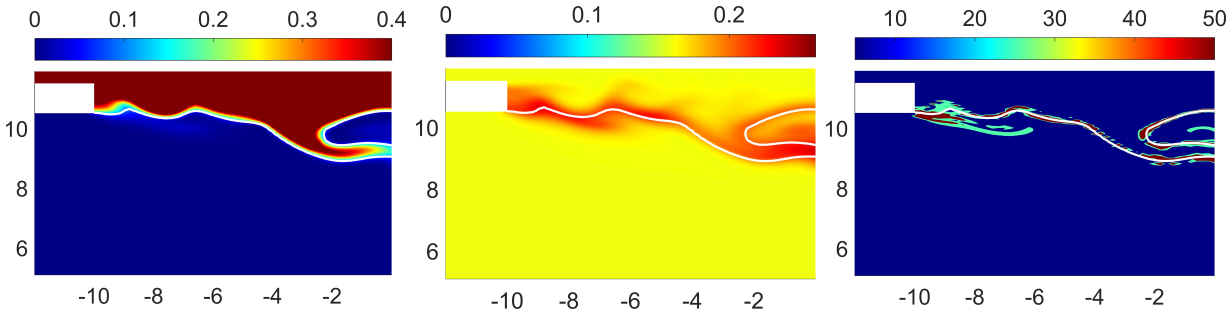

(a) Mean mixture fraction. (b) Progress Variable. (c) HHR.

(d) Rayleigh index.

Figure 5.8: Contour plots of the simulation results using only the stable flamelet branch. HRR has a unit of GJ/m^3s. The Rayleigh index is plotted using the same scale as in figure 4.4.

Figure 5.9 shows the HRR and fuel consumption rate for each of three cases. The flame occurs much closer to the injector lips (upstream of the dump plane) compared with the stable and semi-stable cases. The flame in the stable case is lifted further away from the dump plane compared to the semi-stable case. The most intense fuel consumption region does not entirely overlap the high HRR region. Specifically, in the recirculation zone of case 14-cm, there are regions in which fuel consumption rate is low, but high HRR are found. These regions are dominated by the short-lived fuel-lean flame structures. This phenomenon allows stronger coupling between the HRR and the pressure, leading to higher pressure amplitudes prediction (and closer to the experimental results) compared to other existing axisymmetric calculations.

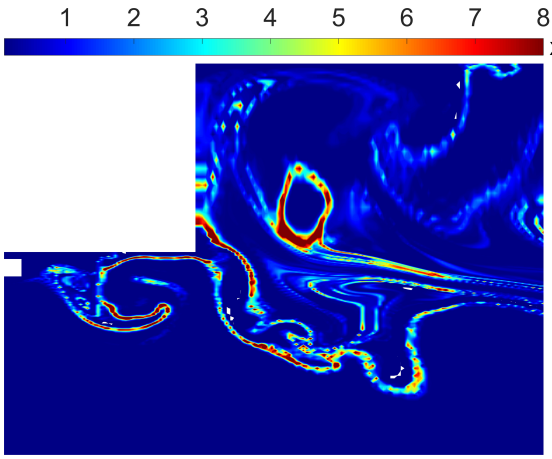

(a) Total HRR for the 14-cm case.

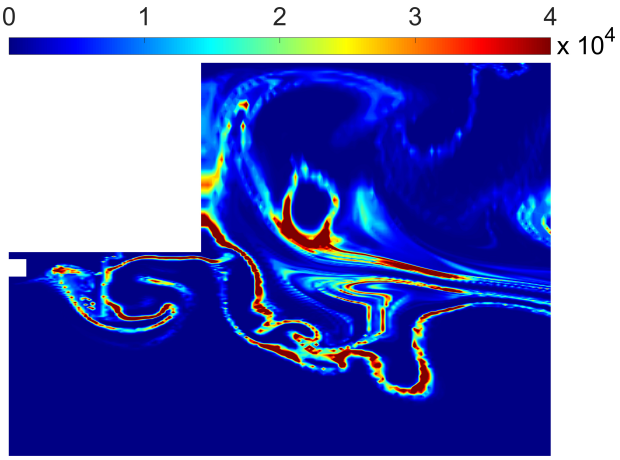

(b) Fuel reaction rate for the 14-cm case.

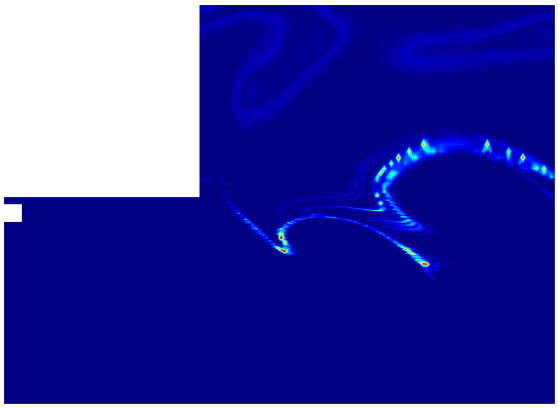

(c) Total HRR for the 9-cm case.

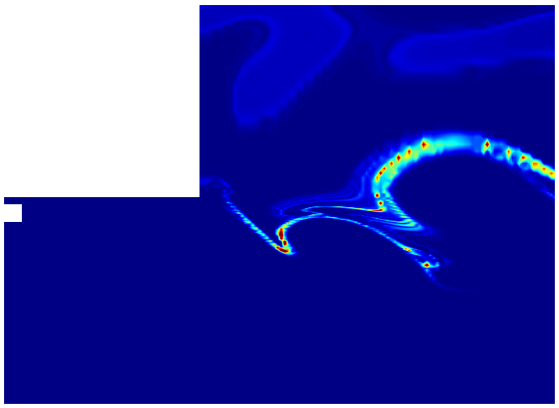

(d) Fuel reaction rate for the 9-cm case.

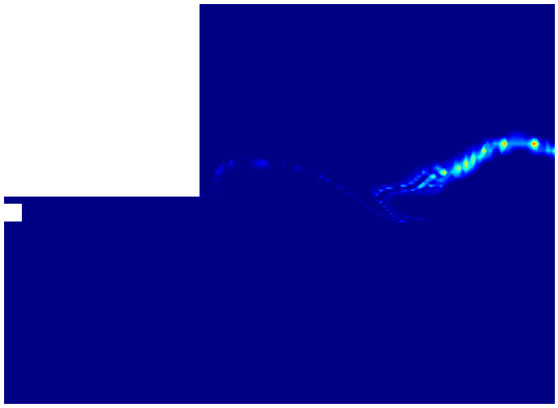

(e) Total HRR for the 17-cm case.

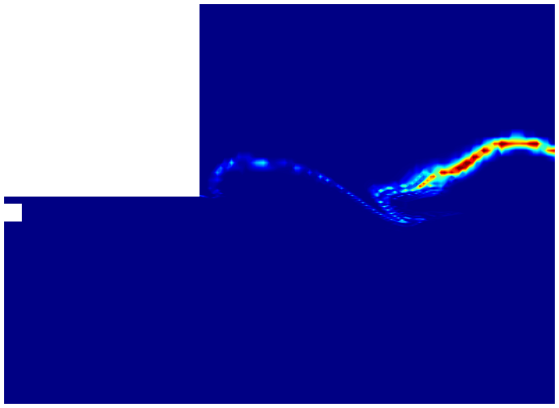

(f) Fuel reaction rate for the 17-cm case.

Figure 5.9: HRR (J/m^3s) and fuel consumption rate (kg/m^3s) contour plots for three different cases.

The nonlinearity of the pulsing mechanism, as well as high axial-to-radial aspect ratio, presents a difficult challenge in the examination of the transient behaviors of local extinction and ignitions such as the one shown in figure 5.5. Scatter plots of the mean temperature somewhat alleviate the difficulty. Figure 5.10 shows scatter plots of the Favre-averaged temperatures ($\tilde{T}$) as functions of the mean mixture fractions ($\tilde{Z}$) at two different locations of the combustion chamber. The broken lines in these figures represent the laminar-flamelet solutions along the S-curve, similar to figure 5.2a. The broken middle lines represent the flame solution at the quenching limit between the stable and unstable branches on the S-curve. The first column represents the data sampled over multiple oscillation periods at the dump plane of the combustion chamber ($x = 0\ cm$). The second column represents the data of the entire chamber surface (a line in our axisymmetric calculations) at the midpoint of the combustion chamber ($x = 20\ cm$). This location represents the pressure node for both the 14- and 9-cm case. Examining the reaction zone of the first column in figure 5.10, it is clear that more burning occurs much closer to the injector lips as the oscillation amplitude increases. Moreover, local extinctions and reignitions occur much more frequently and intensely in the reaction zone of the 14-cm case compared to the other two cases. The solid blue line further illustrates this point in these figures. These lines represent the transient behaviors of an arbitrary point within the shear layer at the dump plane. The points along these curves are labeled by Roman numerals, indicating their orders in time. As seen from figure 5.10a, at time t= *I*, the first point represents an unmixed oxygen situation. At time t= *II*, an unstable flame is observed. The flame is fully burning at time t= *III*. It is then extinguished at time t= *IV*, thus returning it to the mixing line. Similar behavior can be observed for the 9-cm case but on the fuel-rich side. On the other hand, in the 17-cm case, the flame could only burn in the unstable burning branch. The flame is thus strongly anchored at the back step for the 9-cm case while completely lifted from the back step in the 17-cm case.

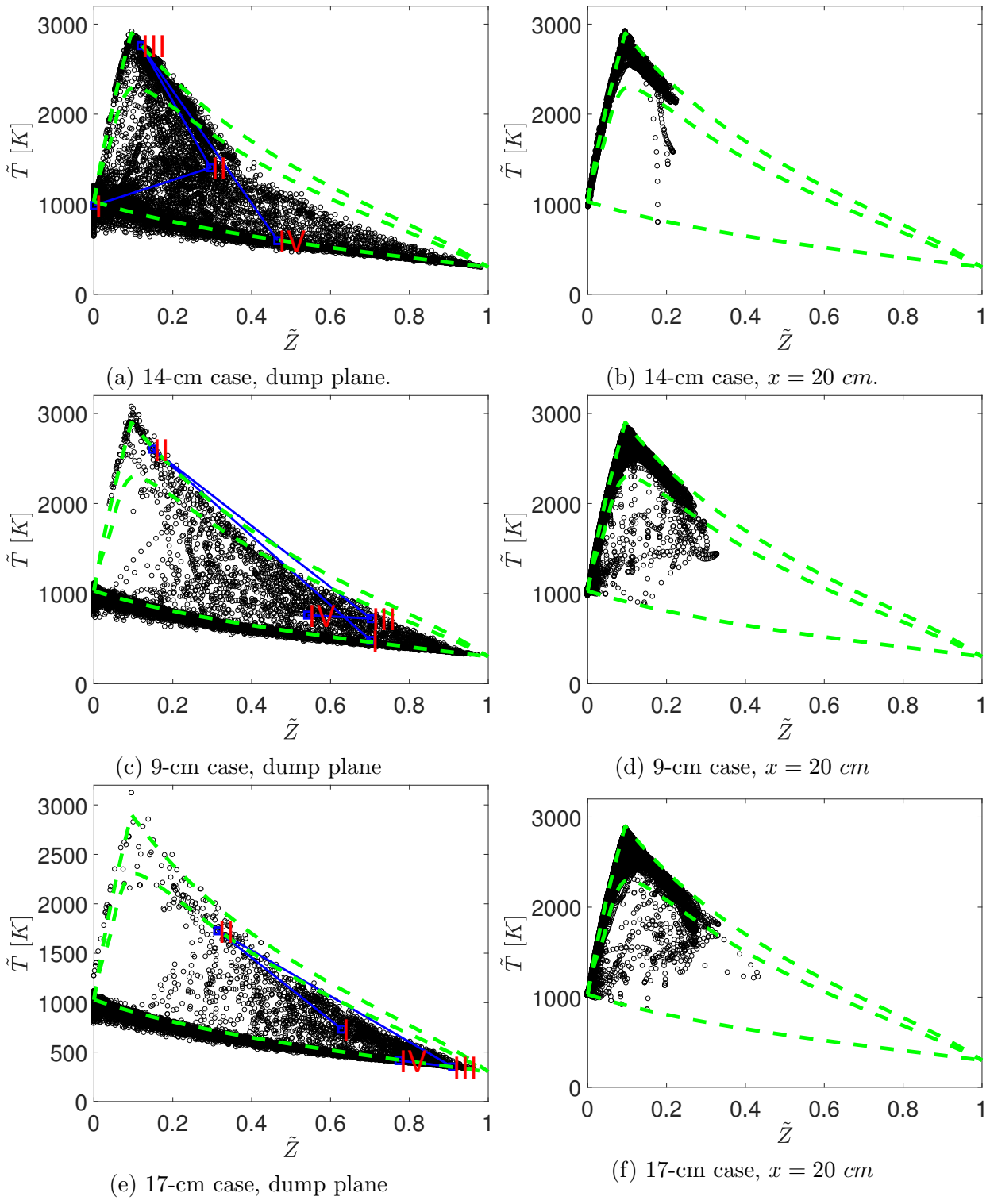

(a) 14-cm case, dump plane.

(b) 14-cm case, $x = 20\ cm$.

(c) 9-cm case, dump plane

(d) 9-cm case, $x = 20\ cm$

(e) 17-cm case, dump plane

(f) 17-cm case, $x = 20\ cm$

Figure 5.10: Scatter plots of the Favre-averaged temperature as functions of mean mixture fraction. Solutions from the laminar flamelet library are also shown as the broken lines.

Comparing the second column of figure 5.10, the flame is entirely burning on the stable branch in the 14-cm case. In the other two cases, the flame still burns in both stable and unstable branches, but with much less intense local ignitions and extinctions compared to the dump plane of the 14-cm case. Finally, by comparing the first row of figure 5.10, we can see the influence of the pressure oscillations on the flamelet temperatures. Notably, at $\tilde{Z} = 0$, at the dump plane (a pressure anti-node), the temperature of the oxidizer stream can differ by more than 300 K from the laminar flamelet solution. On the other hand, at $x = 20\ cm$, the oxidizer temperature remains close to the flamelet solution.

5.3 Burning Mode

As shown previously, the flame in the CVRC is classified as partially premixed regardless of its instability characteristics [39, 71]. Previously, Nguyen *et al.* [71] used the following flame index definition to distinguish between the premixed and non-premixed burning mode:

$$FI = \frac{\nabla Y_f \cdot \nabla Y_o}{\left|\nabla Y_f\right|\left|\nabla Y_o\right|}|\dot{\omega}_f| \tag{5.2}$$

where Y_o, Y_f are the oxidizer and fuel mass fraction, respectively. $\dot{\omega}_f$ is the fuel consumption rate. In equation (5.2), the first term is the classical Takeno flame index. Therefore, the flame index is positive (premixed burning) when the reactant gradients are aligned and negative (non-premixed burning) when the react gradients are opposite of each other. It was shown in figure 5.9, however, there exists high HRR region due to the effects of the secondary reactions on the fuel-lean side, even when the fuel consumption rate is small. Therefore, the

flame index will be modified as

$$FI = \frac{\nabla Y_f \cdot \nabla Y_o}{\left|\nabla Y_f\right|\left|\nabla Y_o\right|}\dot{\omega}_T \tag{5.3}$$

where $\dot{\omega}_T$ is the HRR. In the following analysis, the flame index is first computed, then volume-averaged over the combustion chamber (including the upstream splitter plate region). Figure 5.11 shows the total volume-averaged HRR of the combustion chamber and its fraction that is burning in a non-premixed mode (taking only the negative flame index value.). For clarity, only 2.1 milliseconds are shown in each figure, which corresponds to roughly three first-mode pressure oscillation cycle in the 14-cm case. The initial time in the 14-cm case corresponds to time t1 in figure 5.5. The dominant burning mode is now premixed, as shown by the flame dynamics analysis. As the pressure in the chamber drops, the flame moves further downstream while becoming non-premixed dominant. This observation is further supported by figure 5.6. The cycle repeated itself roughly every 0.7 milliseconds, corresponding to a first-mode cycle period with a frequency of 1520 Hz for the 14-cm case. In the 9-cm case, the lack of a strong pressure oscillation leads to less fluctuation in the averaged HRR. The 17-cm case exhibits similar behavior to the 9-cm case but with less fluctuation in its burning mode because of its stable pressure behavior. The averaged fractions over time of non-premixed burning mode are 46%, 41%, 38% for the 14-cm, 9-cm, and 17-cm cases.

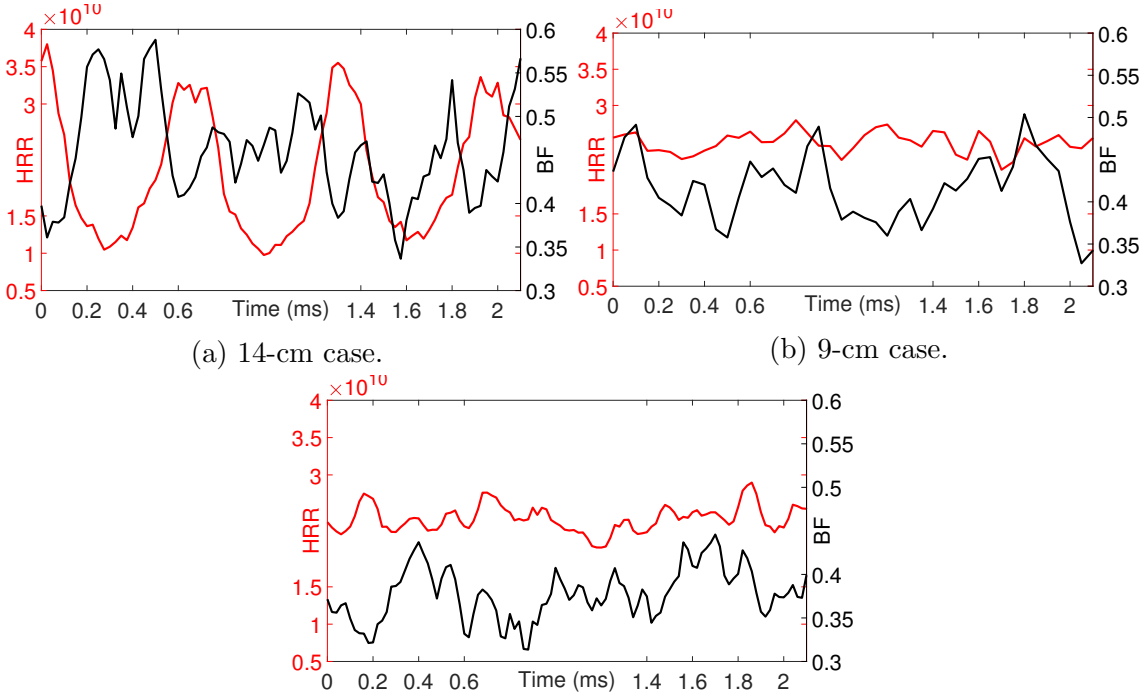

(a) 14-cm case.

(b) 9-cm case.

(c) 17-cm case.

Figure 5.11: Volume-averaged HRR and non-premixed burning fraction (BF) for three different cases. HRR has the unit J/m^3s.

The analysis above suggests that while the current CFPV approach can describe the partially premixed flame in the CVRC experiments, the premixed burning mode is dominant. This means multiple regimes of non-premixed and premixed flamelet approach should be used instead of the current non-premixed flamelet based approach. However, there is also a weakness in the Takeno flame-index definition. By taking the dot products of only the global reactant gradients, it does not adequately represent the flame behaviors when a detailed mechanism is used. Following Seshadri and Peters [77], there exists a small diffusion control reaction layer around the stoichiometric mixture fraction on the fuel-rich side. As shown by Fiorina *et al.* [79] in the double counterflow flame configuration, the flame index cannot adequately distinguish this region from the adjacent premixed fuel-rich flame. This likely means the non-premixed fraction of the total HRR should also be higher.

5.4 Concluding Remarks

Flamelet behaviors under different conditions of the S-curve are examined. In the limit of higher pressure, the combustion process becomes more efficient, thus resulting in a hotter flame. In the unstable flamelet burning branch, the highest HRR locates on the fuel-lean side. In the stable flamelet burning branch, the most intense reaction zone shifts to the fuel-rich side. In the unstable case (14-cm oxidizer post), when the pressure peaks near the dump plane, an adverse-pressure gradient is imposed on the reactant streams. As a result, the flame moves upstream close to the injector lip. During this time, the flame is dominated by premixed burning. Significant local extinctions and reignitions occur during this period. As the pressure decreases inside the chamber, the flame moves further downstream and diffusion burning dominates, where less local ignition and extinction is found. An additional simulation with only stable flamelet burning branch was performed. Without local extinction and reignition, the flame anchored this case at the injector lip. Therefore, the pressure-HRR coupling significantly decreased compared to the simulation where the full S-curve was allowed.

Combustion dynamics are further examined for flames under different pressure instability conditions. In the semi-stable case (9-cm oxidizer post), the flame is lifted away from the injector lip and weakly anchored at the dump plane. In the stable case (17-cm oxidizer post), the flame moves further downstream. In both cases, there is no strong axial flame movement as previously found with the 14-cm oxidizer post. There is a monotonic decrease in local extinction and reignition as the flow becomes more stable (decreases in pressure fluctuations). However, extinction and reignition still occur around the dump plane even for the stable oscillation. Therefore, the whole S-curve, and by extension, the CFPV approach, should be utilized when flame/acoustic interactions are concerned.

Flame index analysis revealed the premixed flame as the dominant burning mode for all

three cases. However, cautious interpretation of the flame index should be taken due to its oversimplified formulation. Nevertheless, there is still a significant amount of premixed burning. A hybrid premixed and non-premixed approaches, like ones used by Knudsen and Pitsch [74], should be considered for future work. More accurate predictions of local extinction and reignitions should also be considered by using the Statistically Most Likely Distribution (SMLD) PDFs for either the progress variable or the pressure [75, 76].

Chapter 6

Chamber Stabilizations and Triggering

In this chapter, we explore the effects of wall heat loss and geometric modifications on stabilizing the combustion chamber. Variation in the mixture ratio by making the flow more fuel lean was explored. However, significant stabilizing effects were not observed compared to the baseline case. Therefore, those results are not presented in this dissertation. As seen in the previous chapters, case 14C with the 14-cm oxidizer post and 38-cm chamber configuration exhibits the most unstable characteristics. Therefore, stabilizing this configuration means all the other configurations will also be stabilized. This case is therefore used as the baseline case and with the same mesh as the calculations presented in chapter 5. In all cases, radial mesh remains unchanged compared to the baseline case. The geometric modifications only change the axial meshes near the oxidizer post inlet and the combustion chamber exit. Grid clustering near the dump plane and the stretching factor remain the same as in the baseline case. The effects of heat loss are explored by imposing various wall temperatures on the combustor wall. As previously mentioned in chapter 2, the isothermal wall boundary condition is now described. Because the wall temperature during the CFD computation is known,

extrapolation procedure to find the mean temperature, as described in section 2.3.3, is no longer needed. Instead, at the end of each time step, from the known mean temperature at the wall, equation 2.30 is used to the determine the total thermal energy. All other wall boundary conditions such as no-slip and impermeability are still applied. In all cases, the constant wall temperature is only imposed on the axial wall and not the back step. This means the maximum flame temperature near the centerline remains similar to the adiabatic case.

6.1 Effects of Wall Heat Loss

Three different wall temperatures are considered: 1800 K, 1030 K, and 600 K. All other parameters are kept the same as the baseline case. For the baseline case, the time-averaged temperature on the combustor wall is around 2700 K (figure 3.6c). As shown in figure 6.1, significant reduction in oscillation amplitude is immediately achieved from the adiabatic case to the 1800-K case. Lowering the wall temperature from 1800 K to 1030 K and subsequently to 600 K results in monotonic but moderate decreases in oscillation amplitude compared to going from the adiabatic case to the 1800-K case. The mean chamber pressure in the 600-K case is around 1700 kPa with the mean-to-peak oscillation amplitude of about 75 kPa. Thus it can be classified as stable. However, by computing the time-averaged fuel mass flow rate at the exit of the combustor, it is found that around 42 % of the fuel is unburnt for the 600-K case. In comparison, 17.32 % and 16.47 % of the fuel is unburnt for the 1030-K and 1800-K, respectively. For the baseline (adiabatic) case, only 6 % of the fuel is unburnt. These facts are consistent with previous findings [71] in which the instability enhances the mixing process, leading the much more efficient combustion processes. Therefore, the stability achieved by the 600-K case is due to inefficient burning.

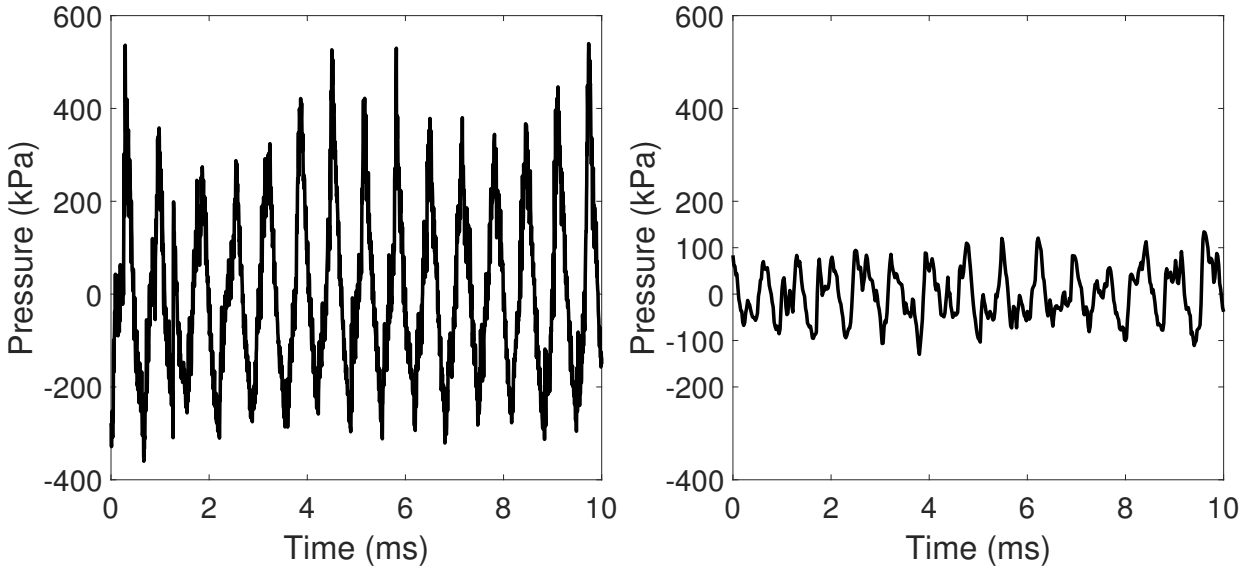

(a) Baseline

(b) $T = 1800\ K$

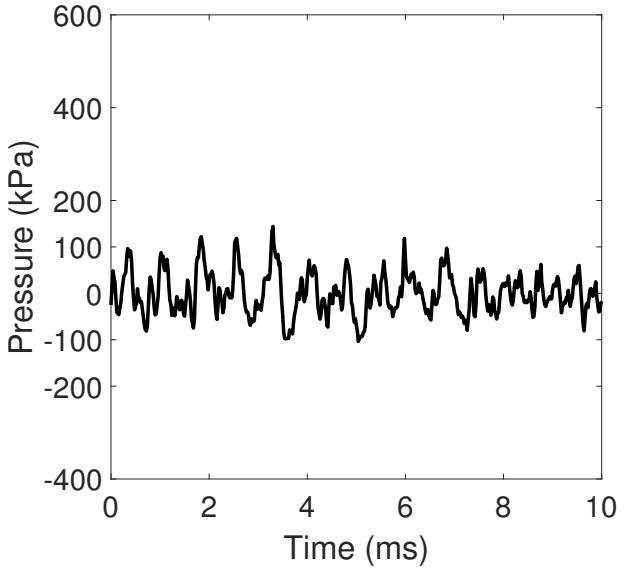

(c) $T = 1030\ K$

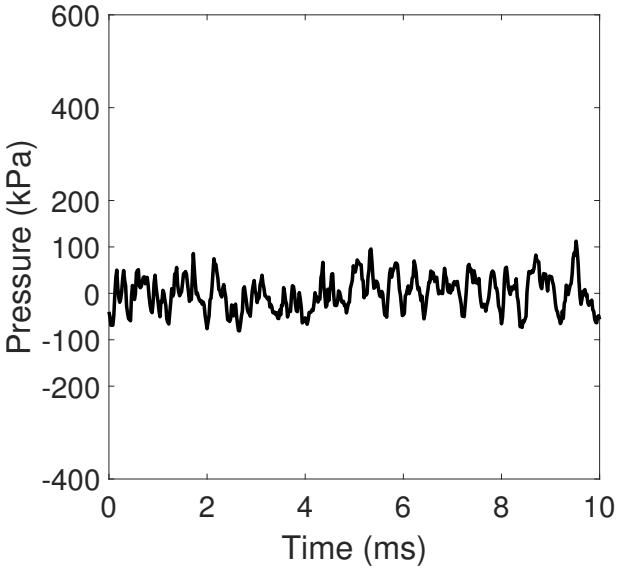

(d) $T = 600\ K$

Figure 6.1: Pressure signals at on the combustion chamber wall at $x = 37\ cm$.

Table 6.1 shows the frequency responses for the first three longitudinal modes for all the cases considered in this section. These frequencies are obtained by identifying the highest frequency responses in the PSD analyses. As seen in table 6.1, decreases in the wall temperature lead to lower frequency responses.

Table 6.1: Dominant frequencies on the combustion chamber wall at $x = 37\ cm$.

Case	f_1 **(Hz)**	f_2 **(Hz)**	f_3 **(Hz)**
Baseline	1520	3053	4565
$T = 1800\ K$	1422	2670	4217
$T = 1030\ K$	1397	2600	4017
$T = 600\ K$	1372	2495	4017

Figure 6.4 shows the time-averaged HRR for all three isothermal cases. The similar flame shape can be observed for all cases, with the most intense reactions found immediately downstream of the back step in the shear layer and near the isothermal wall. Due to the heat loss at the wall, the flames in these cases are more compact around the back-step compared to the baseline case. These flame shapes are similar to case 9C in chapter 3.

Figure 6.2 shows the first longitudinal mode shape for all cases using the same post-processing procedure described in figure 3.4. Compared to figure 3.4, the mode shape in these cases remains relatively the same but with much lower magnitudes.

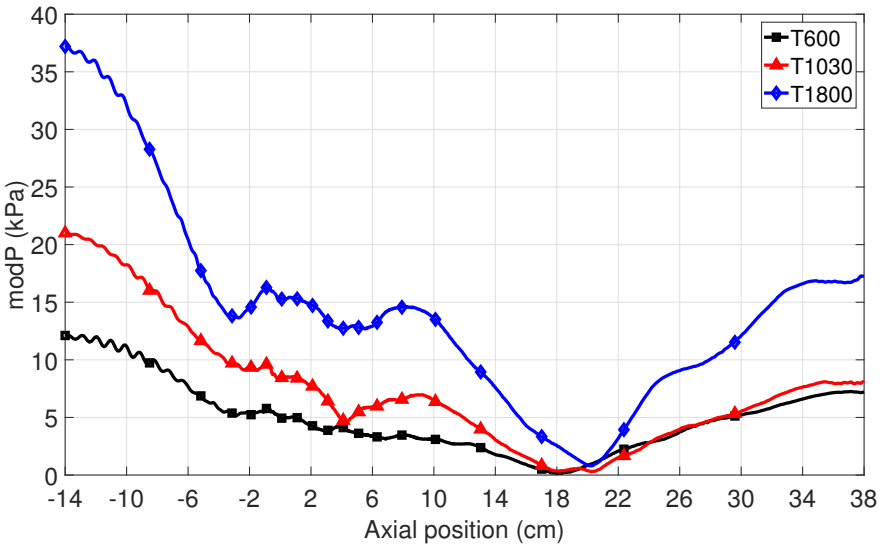

Figure 6.2: First longitudinal mode shape for all isothermal cases.

Figure 6.3 shows the time-averaged temperature as functions of the radial positions for all cases. The correct temperature values are found on the wall for each case, further confirming the validation of the new thermal boundary conditions. While thermal boundary layers are seen in figure 6.3, their resolved structures, mainly through the laminar viscous sublayer, are questionable. This limitation is due to both the deficiency of the current turbulence model as well as the considerable coarse grids used for such high turbulence flow ($Re \approx 400000$). In reality, the combustor wall temperature through viscous sublayer can be even lower even than what is specified at the wall. Nevertheless, the effectiveness of the isothermal boundary condition in modeling heat loss across the wall is valuable in the current study. These results, along with the boundary condition solution procedure described in the introduction of this chapter, means that the heat loss effect is implicitly introduced by decreasing the sensible energy and not the chemical reaction energy generated by the flamelet. Therefore, the HRR magnitudes across all the cases are comparable to the adiabatic cases (left column of figure 6.4) while the maximum flame temperature is still smaller compared to all the adiabatic cases (2500 K vs. 2700 K). The right column of figure 6.4 shows the Rayleigh index for all the isothermal cases. These results are plotted using the same scale for the 9C and 14CP cases demonstrated in figure 4.4, which is at least an order of magnitude smaller than case 14C. Similar to all the cases in the previous section, there are strong pressure-HRR coupling immediately downstream of the back step. However, there is a monotonic decrease in the pressure-HRR coupling observed corresponding to lower wall temperature; thus, further confirming the stabilizing effect of higher wall heat loss.

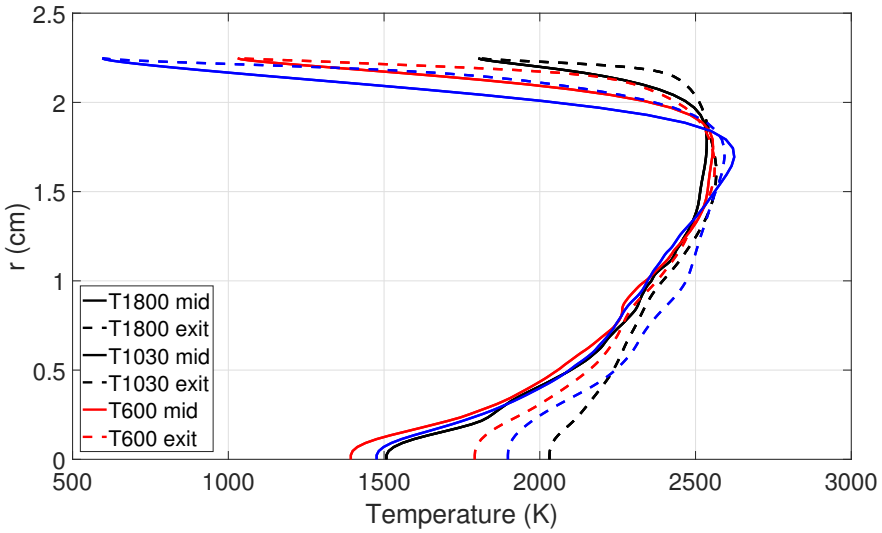

Figure 6.3: Time-averaged temperature at various axial locations for all cases. The solid lines represent the midpoint of the chamber while the broken lines represent the exit location. The maximum y-axis value denotes the combustion wall location.

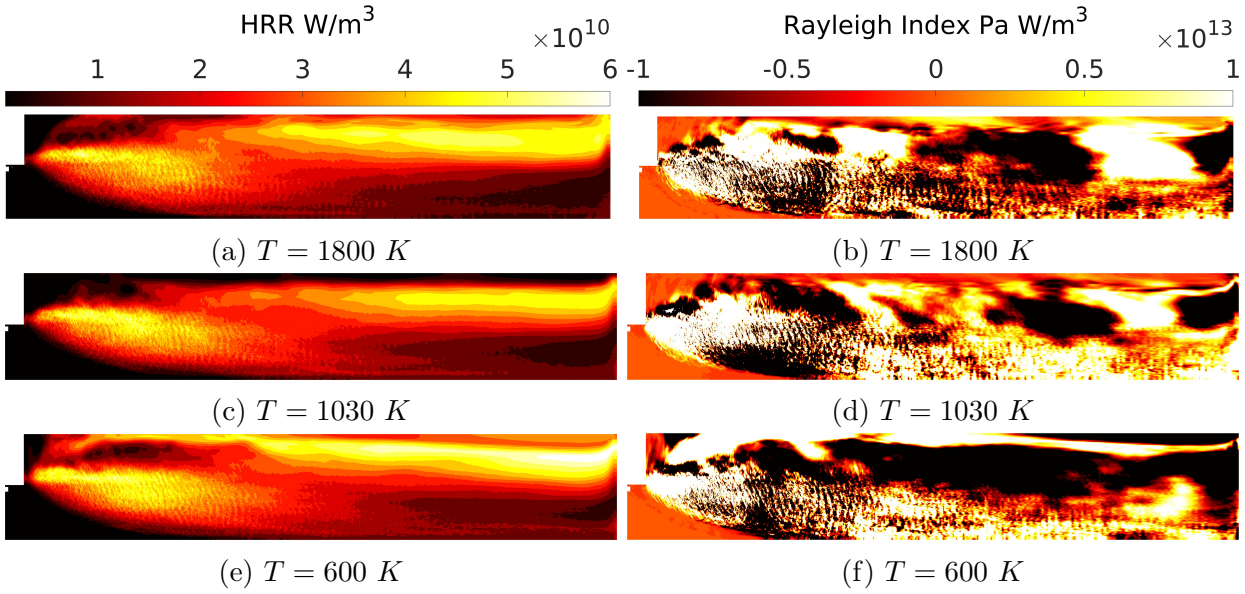

(a) $T = 1800\ K$ (b) $T = 1800\ K$

(c) $T = 1030\ K$ (d) $T = 1030\ K$

(e) $T = 600\ K$ (f) $T = 600\ K$

Figure 6.4: Time-averaged HRR (left column) and Rayleigh index (right column) for all the isothermal cases.

6.2 Effects of Geometric Modifications

6.2.1 General results

In the CVRC experiments, the combination of 19.1-cm oxidizer post and 38-cm chamber leads to a bifurcation in which both stable and unstable oscillations can occur. The following approach is taken to examine the stability characteristic of different geometric modification. First, the chamber is shortened to 30 cm while the oxidizer post length remains at 14 cm. Then, the full 38-cm chamber will be used with the 17-cm oxidizer post. Finally, a simulation is run for the 17-cm oxidizer post with the 30-cm chamber. Adiabatic walls are used for all cases to compare with the baseline case directly. Otherwise, all other parameters are kept the same as in the baseline case.

Figure 6.5 shows the pressure responses for different geometric modification cases. Due to the shortening of the chambers, the previous location of x= 38 cm, corresponding to the downstream pressure anti-node, can no longer be used for comparison. Instead, the pressure is sampled at x= 6 cm, corresponding to the upstream anti-node for all cases. By comparing the respective shortened chamber cases with their corresponding full chamber cases, a drastic reduction in oscillation amplitude is observed, like when heat loss is introduced through the combustor wall. With the mean chamber pressure at roughly 1700 kPa, both of the shortened chamber cases can be classified to be stable. In the baseline case, the limit cycle behavior as shown in figure 6.1 is quickly established a few milliseconds after the initial injection (as described in section 2.4.3) is complete. In comparison, figure 6.5c shows a semi-stable limit-cycle behavior with a peak-to-peak amplitude of roughly 250 kPa for almost 20 milliseconds. After the initial 24 milliseconds, the instability started to grow to a higher amplitude limit-cycle. While not shown here for brevity, simulation beyond the maximum time shown in figure 6.5d are performed in which a full limit cycle behavior is established. In the lower limit cycle, there are 78 % of the injected fuel burnt for this case. Once the higher limit

cycle is established, the combustion process becomes much more efficient, with only 5.5 % of the fuel left unburnt. On average, there are 21.18% (14-cm post) and 19.7% (17-cm post) of the injected fuel left unburned for the two shortened chamber cases. Therefore, the stability achieved in these cases are much more desirable compared to the lowest isothermal wall case. Because of the adiabatic boundary condition used these cases, the time-averaged temperature profiles are similar to ones found in figure 3.6, and will not be plotted here for brevity.

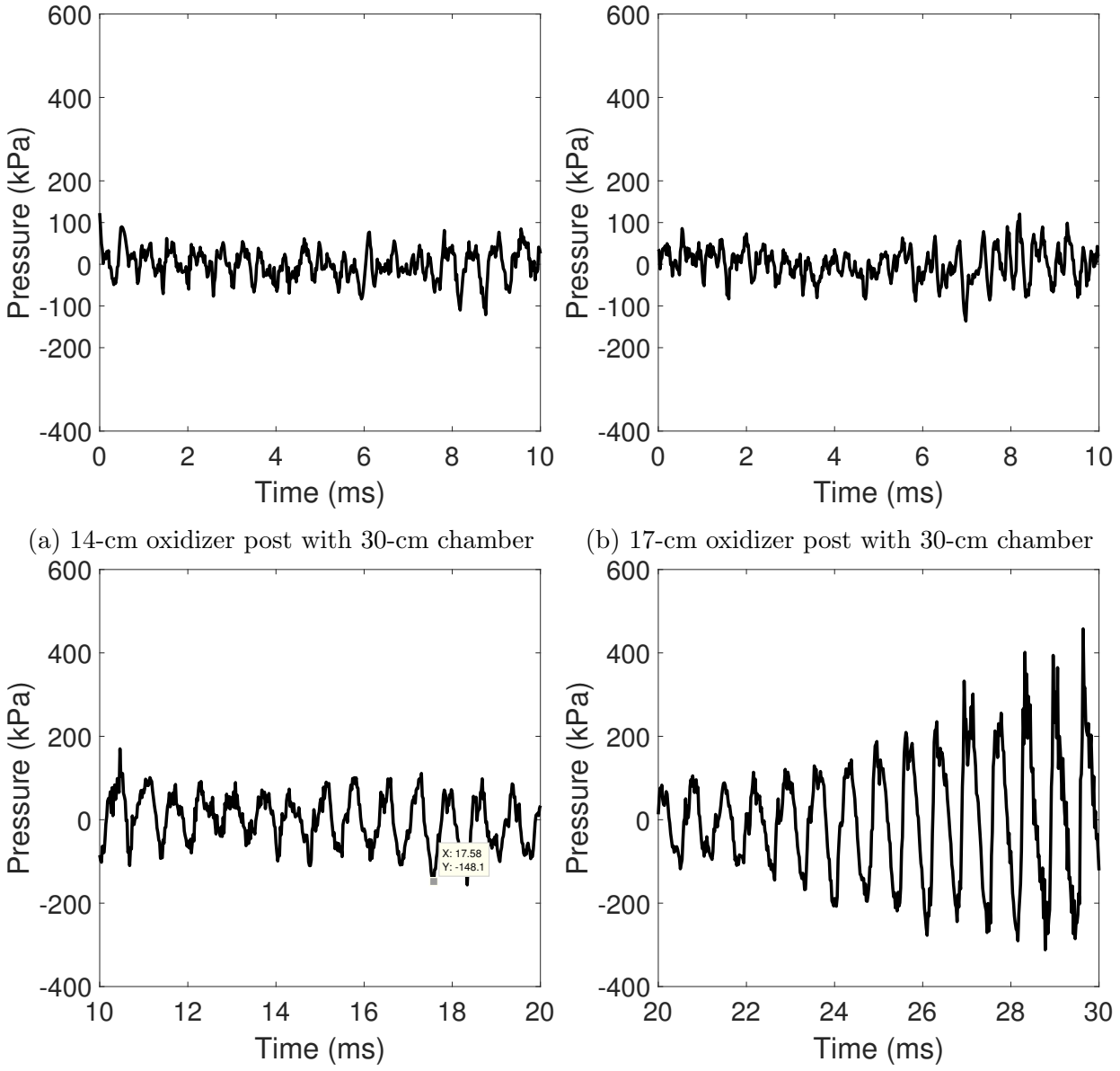

(a) 14-cm oxidizer post with 30-cm chamber

(b) 17-cm oxidizer post with 30-cm chamber

(c) 17-cm oxidizer post with 38-cm chamber, lower limit cycle

(d) 17-cm oxidizer post with 38-cm chamber, transition to higher limit cycle

Figure 6.5: Pressure signals on the combustion chamber wall at $x = 1\ cm$.

Table 6.2 shows the first three longitudinal mode frequency responses for all the cases in this section. As expected, shortening the chamber by 20 % (from 30-cm to 38-cm) results in 16 % and 12 % increases in first mode frequency response for the 14-cm and 17-cm cases, respectively. In contrast, lengthening the oxidizer port from 14-cm to 17-cm only results in roughly 100 Hz decreases in frequency.

Table 6.2: Dominant frequencies on the combustion chamber wall at $x = 1\ cm$.

Case	f_1 **(Hz)**	f_2 **(Hz)**	f_3 **(Hz)**
Baseline	1520	3053	4565
14-cm oxidizer post with 30-cm chamber	1771	3593	5215
17-cm oxidizer post with 38-cm chamber	1447	2919	4142
17-cm oxidizer post with 30-cm chamber	1622	3543	5389

Regardless of the geometric modification, there is a half-wave standing pressure wave occur in the combustor for all cases, as shown in figure 6.6. The standing pressure wave has two anti-nodes around 4-6 cm downstream of the dump plane and at the exit of the combustor. The pressure node is placed at near the midpoint of the combustion chamber. The two shortened chamber cases have relatively the same modulus as the isothermal case with T= 600 K, further confirming their completely stable classifications. Mode shapes during two different stability domains are also plotted for the 17-cm oxidizer post with 38-cm chamber case. The results indicate the first mode being excited, as the modulus responses of the transitioning period are larger than the lower limit-cycle behavior.

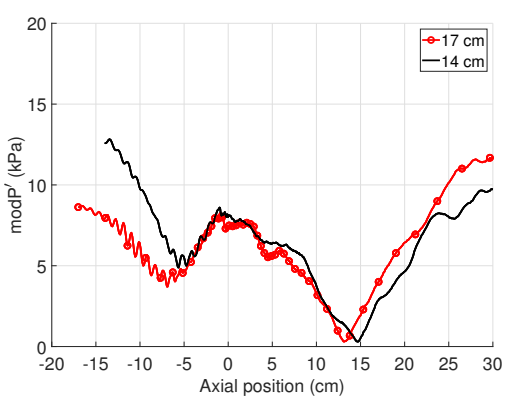

(a) Two 30-cm chamber cases.

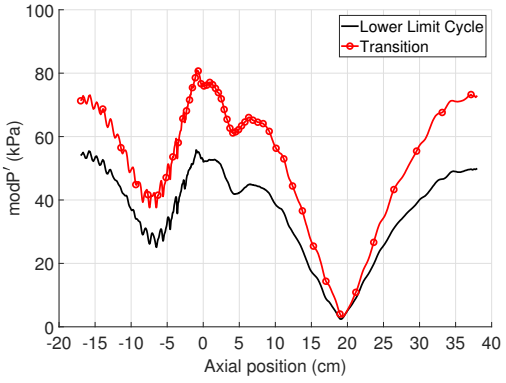

(b) 17-cm oxidizer post with 38-cm chamber.

Figure 6.6: First longitudinal modeshapes for all the cases. Different y-scales are used for the two figures due to different stability characteristics.

Figures 6.7-6.8 show the time-averaged HRR and Rayleigh index results for all cases considered in this section. The flame shape for different cases is very similar, with the most intense burning occur in the first half of the combustion chamber. When the chamber is shortened, the pressure node moves much closer to the intense reaction zones (figure 6.6) compared to the full chamber cases; thus, it results in more stabilizing effects. The Rayleigh index results of the two shortened chamber cases are qualitatively the same as in the isothermal cases. Within the 17-cm oxidizer post with the 38-cm chamber, transitioning between the lower limit cycle to the higher limit cycle shows results in much stronger pressure-HRR coupling at both the upstream and downstream pressure anti-nodes. However, the flame shapes for the two cases remain qualitatively the same.

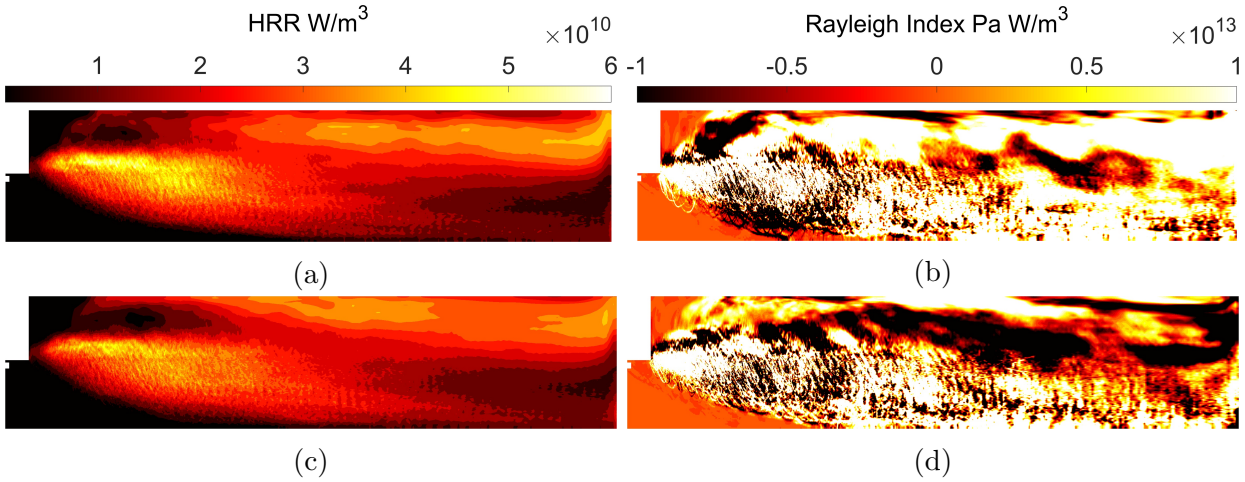

Figure 6.7: Time-averaged HRR and Rayleigh index for the two cases with 30-cm chamber. The top row represents the 14-cm while the bottom row represents the 17-cm oxidizer post cases.

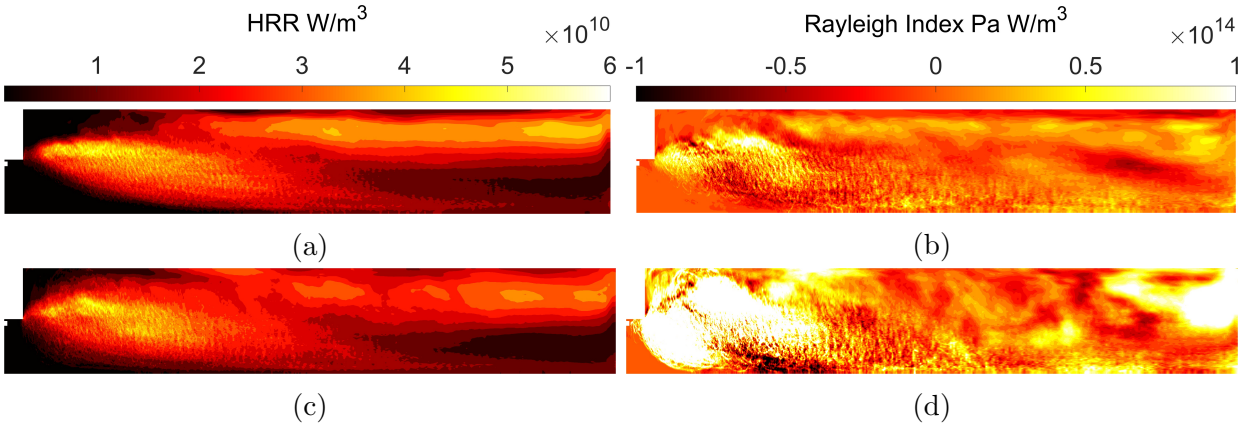

Figure 6.8: Time-averaged HRR and Rayleigh index for the 17-cm case with 38-cm chamber. The top row represents the lower-limit cycle behavior while the bottom row represents the transition to high limit cycle behavior.

6.2.2 Limit-cycle growth description

The above section only offers a qualitative Rayleigh-index analysis on the limit-cycle growth of the 17-cm oxidizer post with 38-cm chamber case. In this section, a more quantitative analysis is added to further identify the growth mechanism of the limit cycle. Nicoud and Poinsot [80], based on the acoustic energy equation, proposed an extended Rayleigh criterion as

$$\frac{\gamma-1}{\gamma p_o}\int_t\int_V p'q'dVdt > \int_t\int_S p'u'dSdt \tag{6.1}$$

where p', q', u' are the fluctuating pressure, HRR, and axial velocity. The left-hand side of the equation is the volume- and time-integrated definition of the spatially local Rayleigh index (equation 4.3) used throughout this dissertation. The right-hand side is defined as the net acoustic fluxes across the boundaries of the enclosed volume. For the instability to sustain (limit-cycle) or grow, the global Rayleigh index (RI) has to be larger than the net acoustic fluxes across the volume. This analysis is applied to two different volumes of the combustion chamber. Region 1 is from $x = 0 - 10\ cm$, corresponds to the upstream

pressure anti-node. Region 2 is from $x = 30\ cm$ to the end of the chamber, corresponds to the downstream pressure anti-node. In the following analysis, the time interval is roughly 0.7 ms, corresponding to a cycle of the first-mode pressure oscillation. Approximately 28 cycles, starting from $t = 10\ ms$ (figures 6.5c-6.5d) are analyzed. Figure 6.9 compares the RI results with the net fluxes across the surfaces of the enclosed volume for Region 1 and 2. Additionally, the total energy output for each region is also plotted on the right secondary axes. The total energy output is defined as

$$E_{out} = \int_t \int_V \dot{Q}_T dV dt \tag{6.2}$$

where $\dot{Q}_T$ is the instantaneous HRR and not the fluctuating HRR (q'). This definition explains the difference in magnitudes between the total energy output and the correlation energy of the extended Rayleigh criterion.

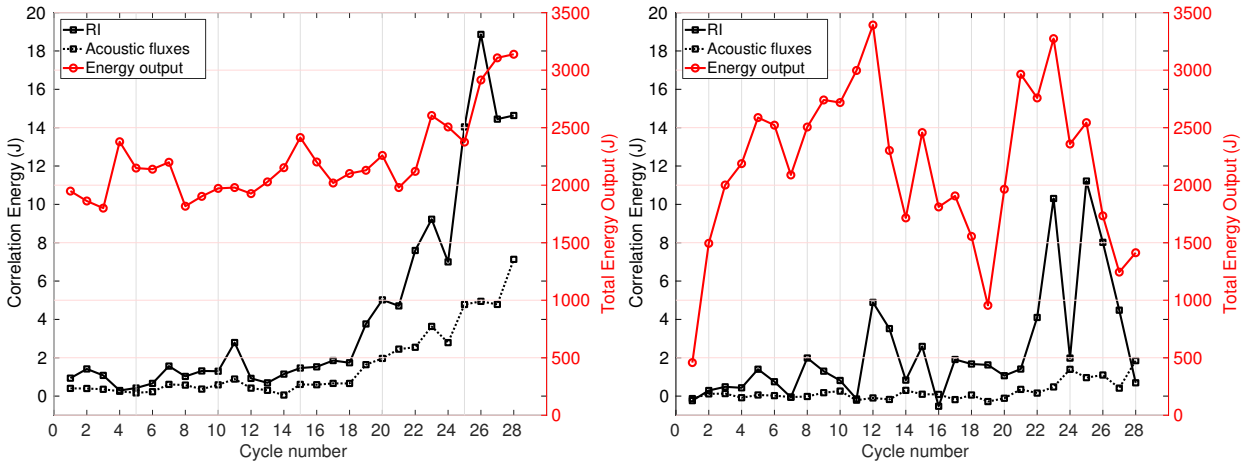

(a) Region 1.

(b) Region 2

Figure 6.9: Extended Rayleigh criterion results and the total energy output of the two different regions.

As seen in figure 6.9, during the lower limit cycle (cycle number 1-15), the combustion drives the pressure instability in the upstream pressure anti-node region (Region 1). In Region 2, the combustion process intermittently supports the instability. The variation between

cycle-to-cycle is much larger compared to Region 1. From cycle 16 (t= 21.2 ms) to later, there is a steep increase in pressure-HRR correlation; thus, a limit cycle growth is seen in figure 6.5d. There is no direct correlation between the RI results as the total energy output. For example, in Region 1, the total energy output between cycle 4, 15, 25 is approximately the same while their correlation energies are very different than each other.

6.3 Triggering

The combustion instability occurs in all previous cases are linearly self-excited. The remainder of this dissertation addresses the question of nonlinear triggering instability. For transverse combustion instability, Popov et al. demonstrated the possibility of triggering by using a localized pressure pulse [6] or a blockage in one of the injector ports [81]. Urbano et al. [38] explored transverse triggering of a 42-injector rocket engine. However, while the instability in the experiment was self-excited, the initial simulation of the same condition was not. Therefore, the triggering is used out of necessity to match the experimental findings. There is currently no triggering study for longitudinal combustion instability using CFD. In this section, triggering results for the two isothermal cases (T=1030 K and T= 1800 K) are presented. For a specified period, both of the fuel and oxygen mass flow rates are simultaneously perturbed using the following general function:

$$\dot{m} = \dot{m}_i \left[1 + \epsilon \left(A_1 sin(\omega_1 t) + A_2 sin(\omega_2 t) + A_3 sin(\omega_3 t) \right) \right] \tag{6.3}$$

where m_i is either the fuel or oxidizer steady-state mass flow rate. Both of the reactants mass flow rates are perturbed to ensure the global equivalence ratio remains constant. $\omega_1, \omega_2, \omega_3$ are the first-, second-, and third-mode frequencies for each respective case (table 6.1). ϵ is the mean-to-peak oscillation amplitude, which is bounded between 0 and 1. In all cases, ϵ

is taken as 0.75. For a specific value of A_1, A_2 and A_3 are computed as

$$A_2 = \frac{2}{3}(1 - A_1), \qquad A_3 = \frac{1}{3}(1 - A_1) \tag{6.4}$$

Two types of disturbances are explored: a pure sine wave in the first mode ($A_1 = 1.0$) and a steep-fronted wave in which higher harmonics are superimposed ($A_1 = 0.5$). Two different triggering durations, corresponding to two and four of the first-mode periods, are used for both wall conditions. Each simulation is performed for 20 ms. Figure 6.10 shows the propellant inlet mass flow rates results for all four triggering simulations of the 1800-K case. Only the first 10 ms results are shown here for clarity. These results confirm the correct behaviors at the inlets.

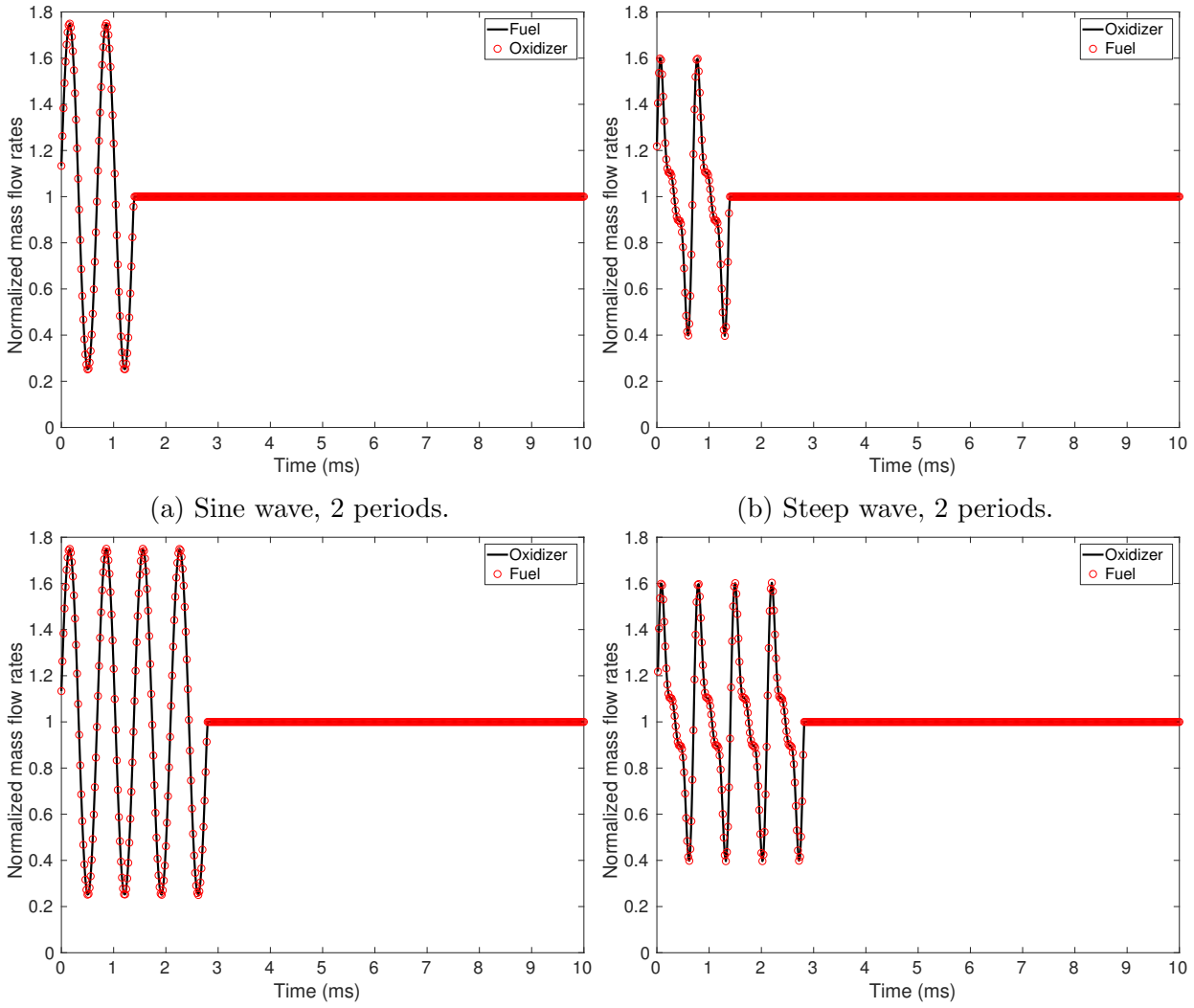

(a) Sine wave, 2 periods.

(b) Steep wave, 2 periods.

(c) Sine wave, 4 periods.

(d) Steep wave, 4 periods.

Figure 6.10: Normalized propellants mass flow rates results for cases with wall temperature of 1800 K.

Figures 6.11-6.12 show the pressure responses of the perturbed flow for both the 1800-K and 1030-K cases. For both wall temperature values, longitudinal combustion instability is triggered for all cases except the 2-period steep wave. In all triggered cases, the limit-cycle amplitudes increase by a factor of 2-3. The triggered 1030-K cases peak-to-peak oscillation amplitudes are roughly 100 kPa smaller than their 1800-K counterparts. Regardless of the type or duration of the disturbances, the limit-cycle magnitudes for the same wall temperature are qualitatively the same.

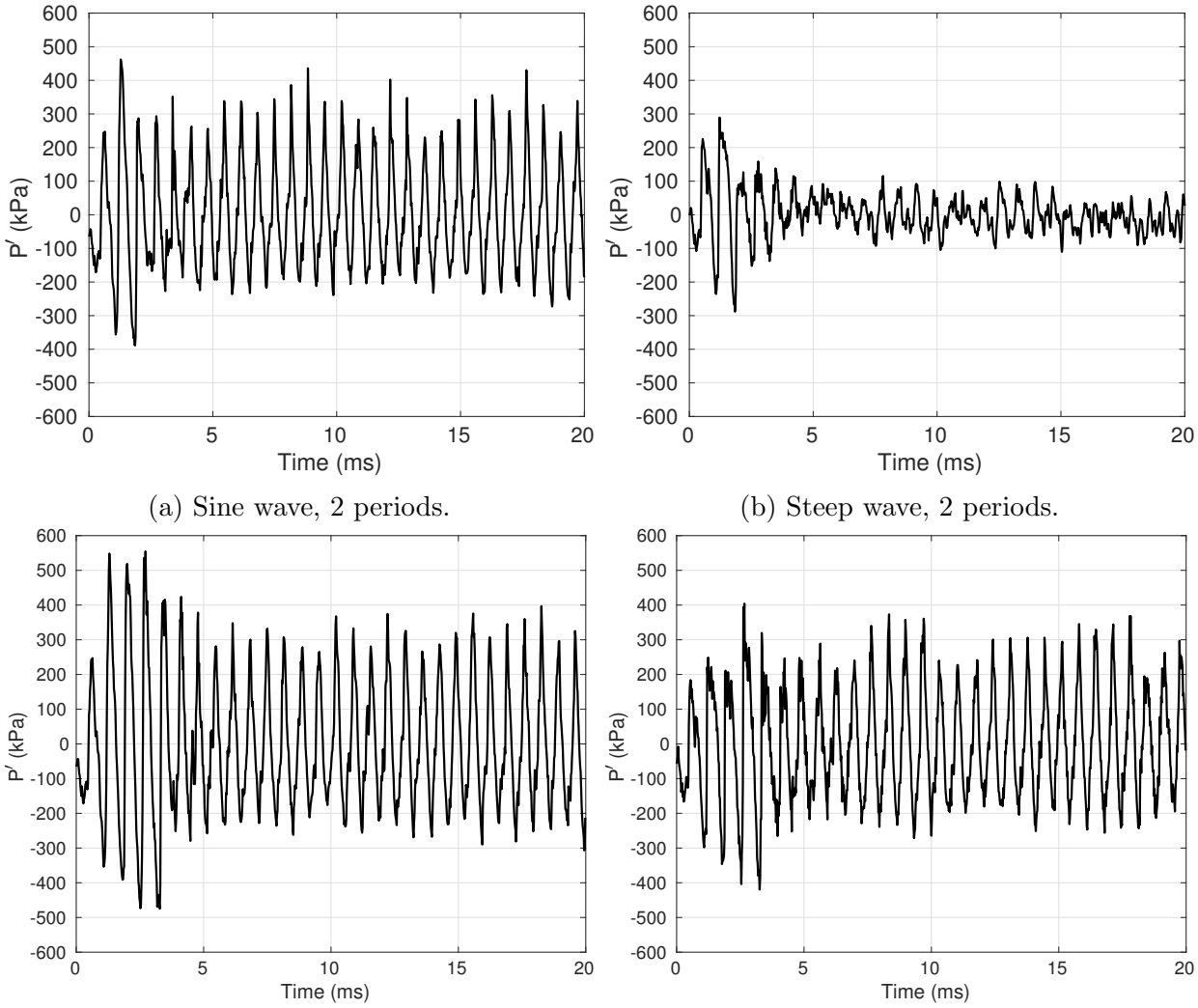

(a) Sine wave, 2 periods.

(b) Steep wave, 2 periods.

(c) Sine wave, 4 periods.

(d) Steep wave, 4 periods.

Figure 6.11: Pressure responses for cases with wall temperature of 1800 K at x= 37 cm.

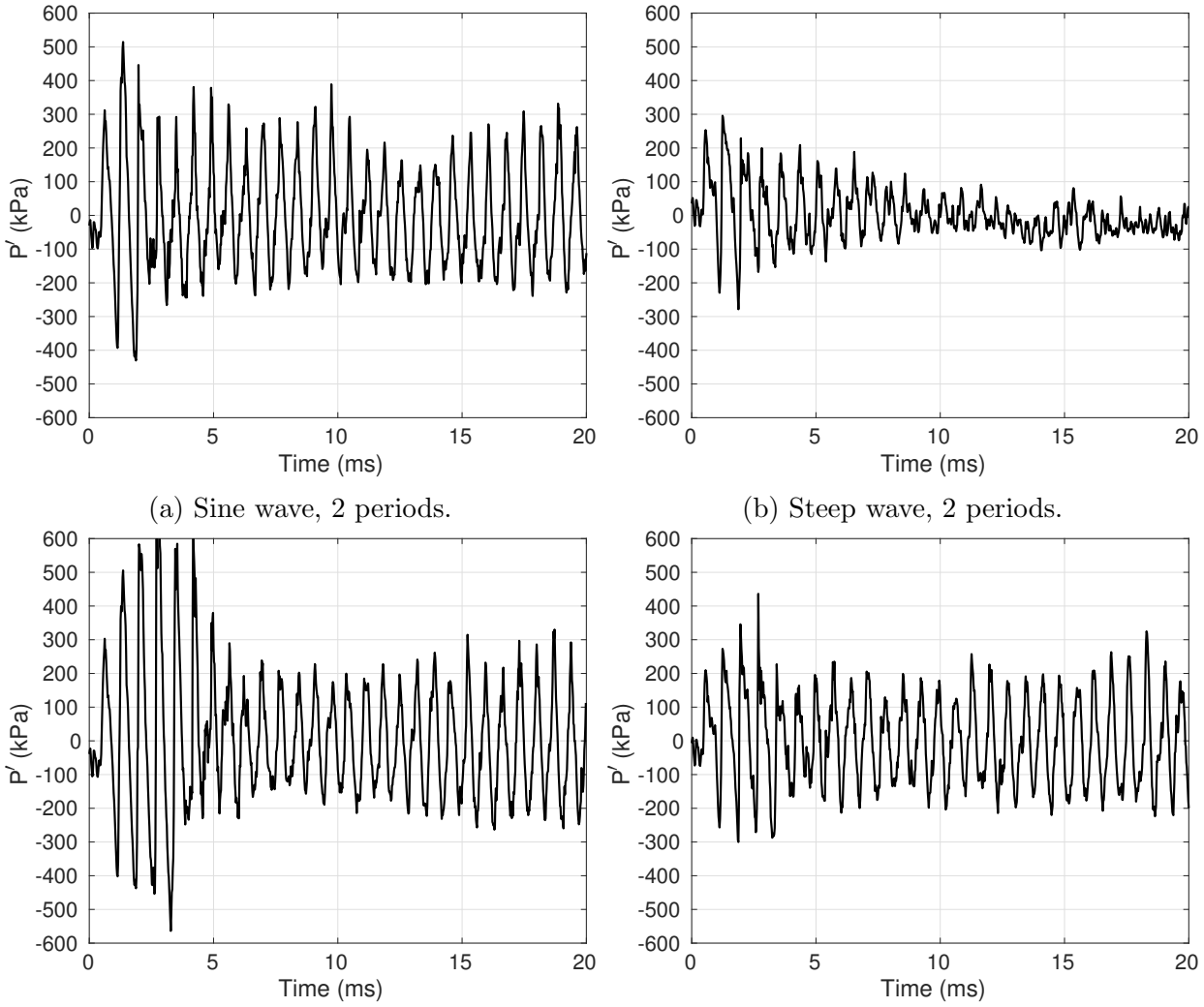

(a) Sine wave, 2 periods.

(b) Steep wave, 2 periods.

(c) Sine wave, 4 periods.

(d) Steep wave, 4 periods.

Figure 6.12: Pressure responses for cases with wall temperature of 1030 K at x= 37 cm.

To further quantify the threshold in which the triggering can occur, from equation 6.3, we have:

$$e_p = \int_0^{t_{trig}} (\dot{m} - \dot{m}_i)^2 dt \tag{6.5}$$

where e_p can be viewed as the cumulative mass flow rate perturbation energy. Because the oxidizer mass flow rate is an order of magnitude larger than its fuel counterpart, the perturbation energy is only calculated for the oxidizer stream. Moreover, these calculations

are performed for the 1800-K only since the difference between the perturbation duration for different wall temperature is very negligible.

Table 6.3: Perturbation energy results for the 4 disturbances type. The unit is kg^2/s.

Type of disturbance	**2 periods**	**4 periods**
Steep wave	1.64e-05	3.29e-05
Sine wave	4.24e-05	8.48e-05

The disturbance energies for all the triggered cases are at least two times larger than the 2-period steep wave disturbances. There is a monotonic increase in maximum pressure responses that correspond to the monotonic increase in the perturbation energy, as shown in the first 5 ms of figures 6.11-6.12 .

Figures 6.13-6.14 compares the instantaneous HRR between the unperturbed and the perturbed conditions for each wall temperature. For the perturbed cases, the HRR is plotted when the limit cycle is fully established. For both wall temperatures in the unperturbed cases, there is no qualitative difference in the flame shape between the trough and the peak of the pressure cycle. However, for the triggered cases of both wall temperature, the flame moves upstream closer to the back step during the peak of the pressure cycle while it becomes much hotter. These behaviors are analogous to those observed in the 14C case. However, due to heat loss across the axial chamber wall, these flames are much more radially compact compared to case 14C (figure 4.5a)

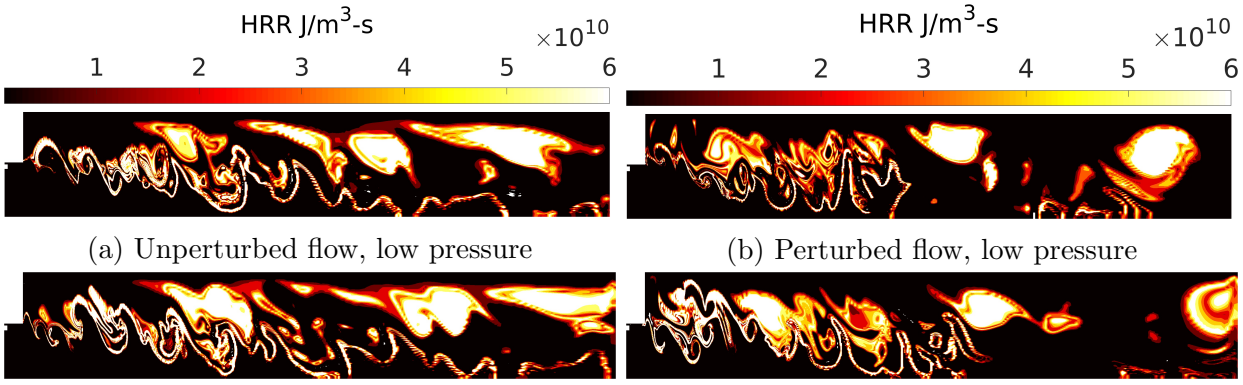

(a) Unperturbed flow, low pressure

(b) Perturbed flow, low pressure

(c) Unperturbed flow, high pressure

(d) Perturbed flow, high pressure

Figure 6.13: Comparisons between the instantaneous HRRs of the original (left column) and triggered (right column) for the 1800-K case. The top row denotes the trough while the bottom row denotes the peak of the pressure cycle within the upstream pressure anti-node region.

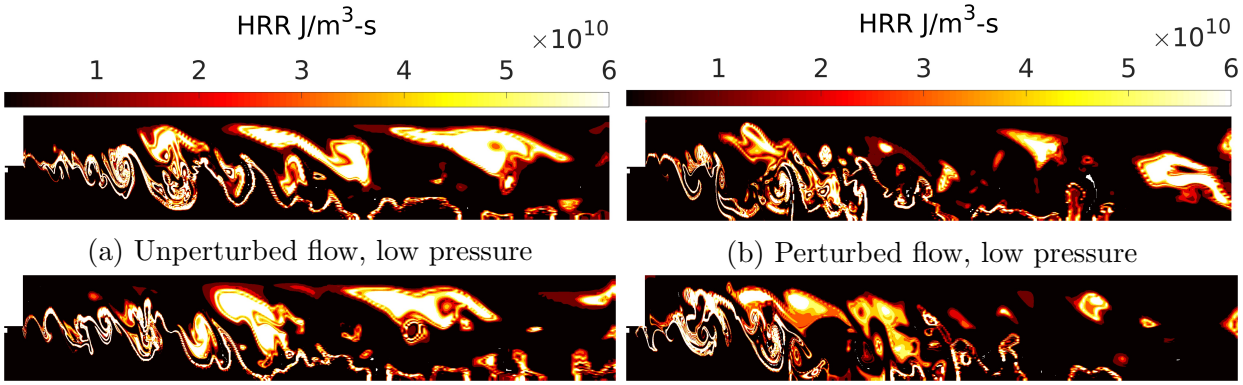

(a) Unperturbed flow, low pressure

(b) Perturbed flow, low pressure

(c) Unperturbed flow, high pressure

(d) Perturbed flow, high pressure

Figure 6.14: Comparisons between the instantaneous HRRs of the original (left column) and triggered (right column) for the 1030-K case. The top row denotes the trough while the bottom row denotes the peak of the pressure cycle within the upstream pressure anti-node region.

Figure 6.15 shows the extended Rayleigh index criterion, as described in section 6.2.2, for Region 1 (x=0-10 cm). The first two cycles data are the same for all quantities when comparing the results of same wave type with different durations; thus, indicating the consistency of the solver in obtaining the correct behavior. In all cases, the average energy output of the region remains the same. However, the correlation energy values are much larger compared to the net acoustic fluxes across the volume for the triggered cases. In contrast, in the

un-triggered case (2-period steep wave), the correlation energy quickly decreases after the initial disturbance is done, leading to rapid decays of the initial pressure responses. Similar to findings in section 6.2.2, the pressure-HRR coupling, not the total energy output, is the dominating factor in determining if a limit cycle is reached. For brevity purposes, similar phenomena are found for the 1030-K triggered cases but not shown here.

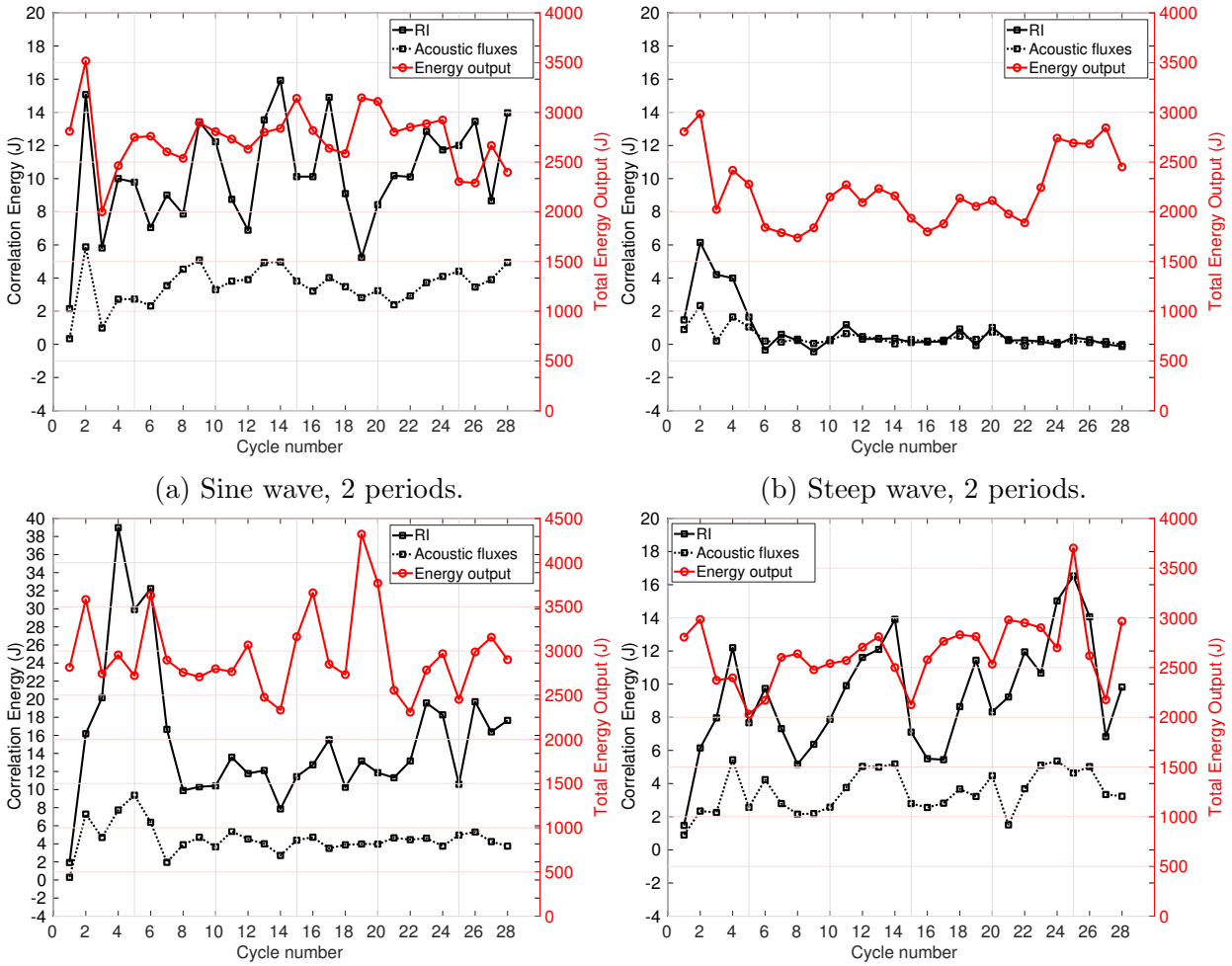

(a) Sine wave, 2 periods.

(b) Steep wave, 2 periods.

(c) Sine wave, 4 periods.

(d) Steep wave, 4 periods.

Figure 6.15: Extended Rayleigh criterion results and the total energy output of Region 1 for the 1800-K cases. The y-axis ranges of sub-figure c are larger compared to the other three subfigures.

6.4 Concluding Remarks

Combustion chamber stabilizing effects are explored via either imposing wall heat loss or chamber geometry modification. In the first section, using a 14-cm oxidizer post with the 38-cm chamber, three different wall temperature values are used: 1800 K, 1030 K, and 600 K. Compared to the adiabatic case in which the wall temperature is 2700 K, imposing an 1800-K wall produces significant heat loss. Further decrease in wall temperature results in more modest amplitude reduction. As the wall becomes cooler, there is a monotonic decrease in oscillation amplitudes. The 600-K wall temperature results in stable oscillation.

In the chamber geometry modification, using a shortened chamber of 30 cm with adiabatic boundary conditions, stable oscillation is found for two different oxidizer post lengths (14 cm and 17 cm). An additional simulation is performed with a 38-cm chamber and 17-cm oxidizer post. In the first initial 20 ms, the pressure oscillates in a lower limit cycle with an amplitude of 250 kPa. However, it gradually grows to a higher limit cycle with a peak-to-peak amplitude of 650 kPa, which is comparable to the 14C case. This higher limit cycle is also found in the experimental results [32]. During the transition from lower limit cycle to higher limit cycle, the pressure-HRR coupling significantly increases in the upstream pressure anti-node. This sudden coupling becomes considerably larger than the net acoustic fluxes across the region, allowing the pressure to grow to a higher limit cycle.

Finally, this chapter also explores the possibility of triggering. While the 1800-K case is considered at first, realistic chamber wall cooling should also consider. Therefore, the 1030-K condition, which is well below the stainless-steel melting temperature, is also used. Triggering is performed by perturbing the mass flow rate at the inlet. Both the fuel and oxidizer mass flow are simultaneously disturbed to ensure constant equivalence ratio. Two different types of disturbance, with two different perturbation periods, are considered: sine and steep waves. A total of 8 simulations are performed. For the steep wave with two periods of perturbation,

the initial significant pressure response is quickly dampened regardless of wall temperature. Triggered instability is achieved for the sine wave with various durations and steep wave with 4-period of perturbation. In all cases, the instability increases by at least a factor of 2. Therefore, the oscillation of the unperturbed flow in both of these wall temperature is classified as unstable limit cycles.

Chapter 7

Conclusions and Future Works

An efficient numerical solver, suitable for solving turbulent compressible combustion, is developed in this dissertation. The computational cost is at least an order of magnitude cheaper than existing axisymmetric solvers while using a more complex chemical mechanism. Therefore, the developed code is suitable for running large parametric studies. For example, 8 triggering cases studied in chapter 6 were performed utilizing only four cores on the UCI HPC cluster during the period of one week.

The developed solver is used to simulate longitudinal combustion instability in the CVRC single-injector rocket engine. Benchmarking our results against the experimental as well as existing three dimensional results, good agreements are found for various cases with different stability domain. Regardless of the stability domain, a half-wavelength standing pressure wave always occurs in the combustion chamber in the first mode. The pressure anti-nodes are located immediately downstream of the back step and before the entrance of the choked nozzle. The main instability mechanism can be attributed to the pressure-HRR coupling in the upstream anti-node. There is significantly more vortex shedding in the unstable cases compared to the semi-stable and stable cases. As a direct effect, the flow mixedness

increases as the pressure oscillation increases; which leads to a more compact flame around the upstream pressure anti-node.

Flame dynamics analysis revealed the combustion process can be classified as a partially premixed flame. Even though the combustion model is based on non-premixed flame formulation, it still reasonably predicts the premixed part of the flame. There are considerably more local extinctions and reignitions in the unstable cases compared to stable cases. These phenomena are crucial in capturing the correct instability behavior.

In the last chapter of this dissertation, different chamber stabilizing effects are found by either imposing wall heat loss or shortening the combustion chamber. Several completely stable domains are found. Using the isothermal wall temperature of 1800 K and 1030 K, combustion instability can be triggered via perturbing the inlet mass flow rate. A minimum threshold in term of perturbation energy is found in which the instability can occur. Two different types of disturbance are used: a sine wave and a steep front wave. For the sine wave, limit cycle with high pressure oscillation can be triggered using a short duration (2 first-mode period). While the steep wave case is significantly less energetic, the instability can be triggered if the perturbation period is sufficiently long. Regardless of the magnitude of the initial disturbance, the oscillation amplitude of the limit-cycle for each respective wall temperature remains the same.

While the parametric study conducted in the final chapter of this dissertation is much larger than any existing efforts, a more comprehensive study with a wider range of parameters should be considered in the future. Even though the solver is very numerically efficient, the computational costs associated with large parametric study are still very high. To that end, reduced-order models are currently being explored in our group.

Improvements in term of numerical methods of the current solver should also be considered. First, the code can be extended into the third dimension to further study the effect of vortex

stretching and tilting on the combustion process. The code can also be written in a more generalized curvilinear form, which will allow it to accommodate more complex geometry. A preconditioning scheme should also be added to simulate turbulent combustion in the low Mach number limits. With future improvements in the turbulence and the flamelet combustion model, these additions will make the current solver much more versatile in simulating not only combustion instability, but also turbulent combustion in general.

Bibliography

[1] J. C. Oefelein and V. Yang, "Comprehensive review of liquid propellant combustion instabilities in f-1 engines," *Journal of Propulsion and Power*, vol. 9, no. 5, pp. 657–677, 1993.

[2] F. E. Culick and V. Yang, *Overview of Combustion Instabilities in Liquid-Propellant Rocket Engines*, ser. AIAA Progress in Astronautics and Aeronautics. Washington,DC: AIAA, 1995, vol. 169, ch. 1, pp. 3–37.

[3] F. E. Culick, "Unsteady motions in combustion chambers for propulsion systems," AGARDograph, Tech. Rep. AG-AVT-039, 2006.

[4] W. A. Sirignano and P. Popov, "Two-dimensional model for liquid-rocket transverse combustion instability," *AIAA Journal*, vol. 51, no. 12, pp. 2919–2934, December 2013.

[5] W. A. Sirignano and L. Crocco, "A shock wave model of unstable rocket combustors," *AIAA Journal*, vol. 2, no. 7, pp. 1285–1296, 1964.

[6] P. P. Popov, A. Sideris, and W. A. Sirignano, "Stochastic modeling of transverse wave instability in a liquid-propellant rocket engine," *Journal of Fluid Mechanics*, vol. 745, pp. 62–91, 2014.

[7] D. Harrje and F. Reardon, "Liquid propellant rocket combustion instability," NASA SP194, Tech. Rep., January 1972.

[8] L. Crocco and S. Cheng, "High frequency combustion instability in rockets with distributed combustion," in *Fourth Symposium (International) on Combustion*, vol. 4, 1953, pp. 865–880.

[9] L. Crocco and S. Cheng, "Theory of combustion instability in liquid propellant rocket motors," in *Monograph 8*. AGARD, 1956.

[10] F. H. Reardon, L. Crocco, and D. Harrje, "Velocity effects in transverse mode liquid propellant rocket combustion instability," *AIAA Journal*, vol. 2, no. 9, pp. 1631–1641, 1964.

[11] L. Crocco and W. A. Sirignano, "Behavior of supercritical nozzle under three dimensional oscillatory conditions," in *Monograph 117*. AGARD, 1967.

[12] H. S. Tsien, "The transfer functions of rocket nozzles," *ARS Journal*, vol. 22, no. 3, pp. 139–143, 1952.

[13] W. A. Sirignano, "Theoretical study of nonlinear combustion instability: Longitudinal mode," Ph.D. Thesis, Department of Aerospace and Mechanical Sciences, Princeton University, Princeton,NJ, 1964.

[14] C. E. Mitchell, L. Crocco, and W. A. Sirignano, "Nonlinear longitudinal instability in rocket motors with concentrated combustion," *Combustion Science and Technology*, vol. 1, no. 1, pp. 35–64, 1969.

[15] B. T. Zinn, "A theoretical study of nonlinear combustion instability in liquid-propellant rocket engines," *AIAA Journal*, vol. 6, no. 10, pp. 1966–1972, 1968.

[16] L. Crocco and C. E. Mitchell, "Nonlinear periodic oscialltions in rocket motors with distributed combustion," *Combustion Science and Technology*, vol. 1, no. 2, pp. 147–169, 1969.

[17] B. T. Zinn and E. A. Powell, "Nonlinear combustion instability in liquid-propellant rocket engines," in *Thirteenth Symposium (International) on Combustion*, vol. 13, 1971, pp. 491–503.

[18] E. Awad and F. Culick, "On the existence and stability of limit cycles for longitudinal acoustic modes in a combustion chamber," *Combustion Science and Technology*, vol. 46, no. 3-6, pp. 195–222, 1986.

[19] V. Yang, S. Kim, and F. Culick, "Triggering of longitudinal pressure oscillations in combustion chambers, i: Nonlinear gas dynamics," *Combustion Science and Technology*, vol. 72, no. 4-6, pp. 183–214, 1990.

[20] F. E. Culick, "Some recent results for nonlinear acoustic in combustion chambers," *AIAA Journal*, vol. 32, no. 1, pp. 146–169, 1994.

[21] M. F. Heidmann and P. Wieber, "Analysis of n-heptane vaporization in unstable combustor with tranvelling transverse osciallations," NASA, Tech. Rep. TN-3424, 1965.

[22] W. C. Strahle, "Unsteady reacting boundary layer on a vaporizing flat plate," *AIAA Journal*, vol. 3, no. 6, pp. 1195–1198, 1965.

[23] W. A. Sirignano, *Fluid Dynamics and Transport of Droplets and Sprays*, 2nd ed. Cambridge University Press, 2010.

[24] R. Bhatia and W. Sirignano, "One-dimensional analysis of liquid-fueled combustion instability," *Journal of Propulsion and Power*, vol. 7, no. 6, pp. 953–961, 1991.

[25] A. Tong and W. A. Sirignano, "Oscillatory vaporization of fuel droplets in unstable combustor," *Journal of Propulsion and Power*, vol. 5, no. 3, pp. 257–261, 1989.

[26] J.-P. Delplanque and W. A. Sirignano, "Transcritical liquid oxygen droplet vaporization: Effect on rocket combustion instability," *Journal of Propulsion and Power*, vol. 12, no. 2, pp. 349–357, 1996.

[27] F. Richecoeur, S. Durcruix, P. Scouflaire, and S. Candel, "Experimental investigation of high-frequency combustion instabilities in liquid rocket engine," *Acta Astronautica*, vol. 62, no. 1, pp. 18–27, 2008.

[28] M. R. Beltran, B. Breen, T. Kosvic, C. Sanders, R. Hoffman, and R. Wright, "Liquid rocket engine combustion instability studies," Air Force Rocket Propulsion Laboratory, Monrovia, California 91016, Tech. Rep., 1966.

[29] K. Miller, J. Sisco, N. Nugent, and W. Anderson, "Combustion instability with a single element swirl injector," *Journal of Propulsion and Power*, vol. 23, no. 5, pp. 1102–1111, 2007.

[30] Y. C. Yu, S. M. Koeglmeier, J. C. Sisco, and W. E. Anderson, "Combustion instability of gaseous fuels in a continuously variable resonance chamber (cvrc)," in *44th AIAA/ASME/SAE/ASEE Joint Propulsion Conference and Exhibit.* Hartford, CT: AIAA, July 2008.

[31] Y. C. Yu, L. O'Hara, J. C. Sisco, and W. E. Anderson, "Experimental study of high-frequency combustion instability in a continuously variable resonance combustor(cvrc)," in *47th AIAA Aerospace Sciences Meeting Including The New Horizons Forum and Aerospace Exposition.* Orlando, Florida: AIAA, 2009.

[32] Y. C. Yu, J. C. Sisco, S. Rosen, A. Madhav, and W. E. Anderson, "Spontaneous longitudinal combustion instability in a continuously variable resonance combustor," *Journal of Propulsion and Power*, vol. 28, no. 5, pp. 876–887, 2012.

[33] R. Smith, G. Xia, W. A. Anderson, and C. L. Merkle, "Computational simulations of the effect of backstep height on nonpremixed combustion instability," *AIAA Journal*, vol. 48, no. 9, pp. 1857–1868, 2010.

[34] H. Huo, X. Wang, and V. Yang, "A general study of counterflow diffusion flames at subcritical and supercritical conditions: Oxygen/hydrogen mixtures," *Combustion and Flames*, vol. 161, pp. 3040–3050, 2014.

[35] S. Menon and W.-H. Jou, "Large-eddy simulations of combustion instability in an axisymmetric ramjet combustor," *Combustion Science and Technology*, vol. 75, pp. 53–72, 1991.

[36] G. Staffelbach, L. Gicquel, G. Boudier, and T. Poinsot, "Large-eddy simulations of self-excited azimuthal modes in annular combustors," *Proceedings of the Combustion Institute*, vol. 32, pp. 2909–2916, 2009.

[37] A. Ghani, T. Poinsot, L. Gicquel, and G. Staffelbach, "Les of longitudinal and transverse self-excited combustion instabilities in a bluff-body stabilized turbulent premixed flame," *Combustion and Flame*, vol. 162, pp. 4075–4083, November 2015.

[38] A. Urbano, L. Selle, G. Staffelbach, B. Cuenot, T. Schmitt, S. Ducruix, and S. Candel, "Exploration of combustion instability triggering using large eddy simulation of a multiple injector liquid rocket engine," *Combustion and Flame*, vol. 169, pp. 129–140, 2016.

[39] S. Srinivasan, R. Ranjan, and S. Menon, "Flame dynamics during combustion instability in a high-pressure, shear-coaxial injector combustor," *Flow, Turbulence and Combustion*, pp. 1–26, 2014. [Online]. Available: http://dx.doi.org/10.1007/s10494-014-9569-x

[40] R. Garby, L. Selle, and T. Poinsot, "Large-eddy simulation of combustion instabilities in a variable length combustor," *Comptes Rendus Mecanique*, vol. 341, pp. 220–229, 2013.

[41] M. E. Harvazinski, W. E. Anderson, and C. L. Merkle, "Analysis of self-excited combustion instabilities using two- and three dimensional simulations," *Journal of Propulsion and Power*, vol. 29, no. 2, pp. 396–409, 2013.

[42] M. E. Harvazinski, D. G. Talley, and V. Sankaran, "Application of detailed chemical kinetics to combustion instability modeling," in *54th AIAA Aerospace Sciences Meeting*. San Diego,CA: AIAA, January 2016.

[43] S. V. Sardeshmukh, S. D. Heister, and W. E. Anderson, "Prediction of combustion instability with detailed chemical kinetics," in *53rd AIAA Aerospace Sciences Meeting*. Kissimmee,FL: AIAA, January 2015.

[44] M. Harvazinski, V. Sankaran, and D. Talley, "Parametric trends in the combustion stability characteristics of a single-element gas-gas rocket engine," in *52nd AIAA Aerospace Sciences Meeting*. National Harbor,MD: AIAA, January 2014.

[45] P. Spalart, W. H. Jou, M. Strelets, and S. Allmaras, "Comments on the feasibility of les for wings and on a hybrid rans/les approach," in *First AFOSR Conference on DNS/LES*, January 1997.

[46] N. Peters, *Turbulent Combustion*, 2nd ed., ser. Cambridge Monographs on Mechanics. Cambridge: Cambridge University Press, 2000.

[47] F. Liu and X. Zheng, "A strongly coupled time-marching method for solving the navier-stokes and k-ω turbulence model equations with multigrid," *Journal of Computational Physics*, vol. 128, 1996.

[48] M. Strelets, "Detached eddy simulation of massively separated flows," in *39th Aerospace Sciences Meeting and Exhibit*. Reno, NV: AIAA, January 2001.

[49] R. H. Nichols, "A comparison of hybrid rans/les turbulence models for a generic weapons bay with and without a spoiler," in *26th AIAA Applied Aerodynamics Conference*. Honolulu, Hawaii: AIAA, 2008.

[50] D. Chakraborty, P. Paul, and H. Mukunda, "Evaluation of the combustion models for high speed h2/air confined mixing layer using dns data," *Combustion and Flame*, vol. 121, pp. 195–209, 2000.

[51] P. Volpiani, T. Schimitt, and D. Veynante, "A posteriori tests of a dynamic thickened flame model for large eddy simulations of turbulent premixed combustion," *Combustion and FLame*, vol. 174, pp. 166–178, 2016.

[52] T. Poinsot and D. Veynannte, *Theoretical and Numerical Combustion*, 2nd ed. Philaphidelphia, PA: R.T. Edwards, Inc, 2005.

[53] D. Haworth, "Progress in probability density function methods for turbulent reacting flows," *Progress in Energy and Combustion Science*, vol. 36, pp. 168–259, 2010.

[54] P. P. Popov and S. B. Pope, "Large eddy simulation/probability density function simulations of bluff body stabilized flames," *Combustion and Flame*, vol. 161, pp. 3100–3133, 2014.

[55] V. Moureau, P. Minot, H. Pitsch, and C. Brat, "A ghost-fluid method for large-eddy simulations of premixed combustion in complex geometries," *Journal of Computational Physics*, vol. 221, pp. 600–614, 2007.

[56] A. Benima and K. Syedb, "Laminar flamelet modelling of turbulent premixed combustion," *Applied Mathematical Modelling*, vol. 22, pp. 113–136, 1998.

[57] H. Kolla and N. Swaminathan, "Strained flamelets for turbulent premixed flames, i: Formulation and planar flame results," *Combustion and Flame*, vol. 157, pp. 943–954, 2010.

[58] P. Domingo, L. Vervisch, and D. Veynante, "Large-eddy simulation of a lifted methane jet flame in a vitiated coflow," *Combustion and Flame*, vol. 152, pp. 415–432, 2008.

[59] S. Popp, F. Hunger, S. Hartl, D. Messig, B. Coriton, J. H. Frank, F. Fuest, and C. Hasse, "Les flamelet-progress variable modeling and measurements of a turbulent partially-premixed dimethyl ether jet flame," *Combustion and Flame*, vol. 162, pp. 3016–3029, 2015.

[60] M. D. Renzo, A. Coclite, M. D. de Tullio, P. D. Palma, and G. Pascazio, "Les of the sandia flame d using an fpv combustion model," *Energy Procedia*, vol. 82, pp. 402–409, 2015.

[61] C. D. Pierce and P. Moin, "Progress-variable approach for large-eddy simulation of non-premixed turbulent combustion," *Journal of Fluid Mechanics*, vol. 504, pp. 73–97, 2004.

[62] R. Pecnik, V. E. Terrapon, F. Ham, G. Iaccarino, and H. Pitsch, "Reynolds- averaged navier-stokes simulations of the hyshot ii scramjet," *AIAA Journal*, vol. 50, no. 8, pp. 1717–1732, 2012.

[63] A. Saghafian, V. E. Terrapon, and H. Pitsch, "An efficient flamelet-based combustion model for compressible flows," *Combustion and Flame*, vol. 162, pp. 652–667, 2015.

[64] A. Saghafian, L. Shunn, D. A. Phillip, and F. Ham, "Large eddy simulations of the hifire scramjet using a compressible flamelet/progress variable approach," *Proceedings of the Combustion Institute*, vol. 35, pp. 2163–2172, 2015.

[65] A. Jameson, W. Schmidt, and E. Turkel, "Numerical solution of the euler equations by finite volume methods using runge kutta time stepping schemes," in *14th Fluid and Plasma Dynamics Conference*, Palo Alto, CA, June 1981.

[66] M. Harvazinski, "Modeling self-excited combustion instabilities using a combination of two and three dimensional simulations," Ph.D. dissertation, Purdue University, West Lafayette, Indiana, May 2012.

[67] T. Poinsot and S. K. Lele, "Boundary conditions for direct simulations of compressible viscous flows," *Journal of Computational Physics*, vol. 101, no. 1, pp. 104–129, 1992.

[68] L. Crocco and W. A. Sirignano, "Effects of transverse velocity components on the nonlinear behavior of short nozzles," *AIAA Journal*, vol. 4, no. 8, pp. 1428–1430, 1966.

[69] H. Pitsch, "Flamemaster, a c++ computer program for 0d combustion and 1d laminar flame calculations."

[70] N. Peters and B. Rogg, *Reduced Kinetic Mechanism for Applications in Combustion System*, ser. Lecture notes in physics. Berlin, New York: Springer-Verlag, 1993.

[71] T. M. Nguyen, P. P. Popov, and W. A. Sirignano, "Longitudinal combustion instability in a rocket engine with a single coaxial injector," *Journal of Propulsion and Power*, vol. 34, no. 2, pp. 354–373, 2018. [Online]. Available: https://arc.aiaa.org/doi/pdf/10.2514/1.B36516

[72] M. Harvazinski, C. Huang, V. Sankaran, T. Feldman, W. Anderson, C. Merkle, and D. Talley, "Coupling between hydrodynamics, acoustics, and heat release in a self-excited unstable combustor," *Physics of Fluids*, vol. 27, 2015.

[73] K. Schadow and E. Gutmark, "Combustion instability related to vortex shedding in dump combustors and their passive control," *Progress in Energy and Combustion Science*, vol. 18, pp. 117–132, 1992.

[74] E. Knudsen and H. Pitsch, "Capabilities and limitations of multi-regime flamelet combustion models," *Combustion and Flame*, vol. 159, pp. 242–264, 2012.

[75] M. Ihme, C. M. Cha, and H. Pitsch, "Prediction of local extinction and re-ignition effects in non-premixed turbulent combustion using a flamelet/progress variable approach: 1. a priori study and presumed pdf closure," *Combustion and Flame*, vol. 155, pp. 70–89, October 2008.

[76] M. Ihme, C. M. Cha, and H. Pitsch, "Prediction of local extinction and re-ignition effects in non-premixed turbulent combustion using a flamelet/progress variable approach: 2. application in les of sandia flames d and e," *Combustion and Flame*, vol. 155, pp. 90–107, October 2008.

[77] K. Seshadri and N. Peters, "Asymptotic structure and extinction of methane-air diffusion flames," *Combustion and Flame*, vol. 73, pp. 23–44, 1988.

[78] T. A. Pant, C. Huang, C. Han, S. V. Sardeshmukh, W. E. Anderson, and H. Wang, "Flamelet modeling studies of a continuously variable resonance combustor," in *54th AIAA Aerospace Sciences Meeting*. San Diego,CA: AIAA, January 2016.

[79] B. Fiorina, O. Gicquel, L. Vervisch, S. Carpentier, and N. Darabiha, "Approximating the chemical structure of partially premixed and diffusion counterflow flames using fpi flamelet tabulation," *Combustion and Flame*, vol. 140, pp. 147–160, 2005.

[80] F. Nicoud and T. Poinsot, "Thermoacoustic instabilities: Should the rayleigh criterion be extended to include entropy changes," *Combustion and Flame*, vol. 142, pp. 153–159, 2005.

[81] P. P. Popov, W. A. Sirignano, and A. Sideris, "Propellant injector influence on liquid-propellant rocket engine instability," *Journal of Propulsion and Power*, vol. 31, pp. 320–331, 2014.

Appendix A

RANS vs DDES

As previously mentioned in chapter 2, the importance of the turbulence model is further examined here. Figure A.1 compares the instantaneous temperature results of the 14C (most unstable) case using the two turbulence models. The CFPV approach are used in both cases. The full combustion chamber is plotted. An axial-to-radial aspect ratio of 3:1 is used.

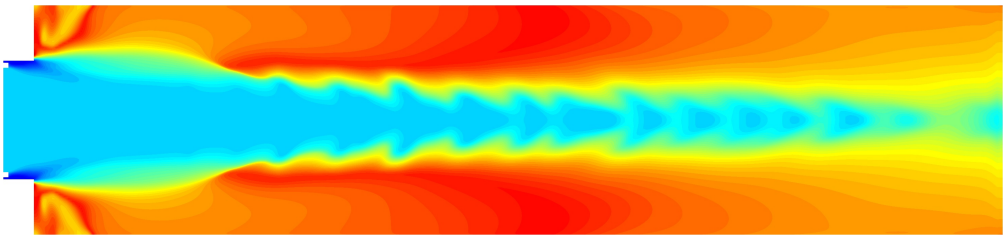

(a) RANS result.

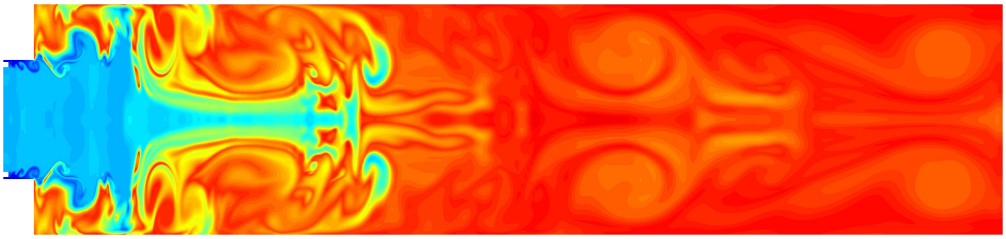

(b) DDES result.

Figure A.1: Instantaneous temperature fields using two different turbulence models.

Because the turbulent production term in the k transport equation is a function of the mean-strain rate, its magnitude becomes significantly high in the shear mixing layer around the back step. Therefore, the RANS model generally overproduces turbulent kinetic energy, and subsequently the turbulent viscosity. The inherent problem arises from the incorrect assumption that all scales of the unsteady motion can be captured by the RANS model. The large turbulent viscosity dampens any unsteady motion of the fluids, particularly vortex shedding and acoustic waves propagation. Therefore, there are significantly fewer vortex structures immediately downstream of the back step in the RANS result compared to the DDES result, as shown in figure A.1. This leads to underprediction of the pressure oscillation amplitudes in the RANS simulation compared to the DDES simulation, as seen in figure A.2.

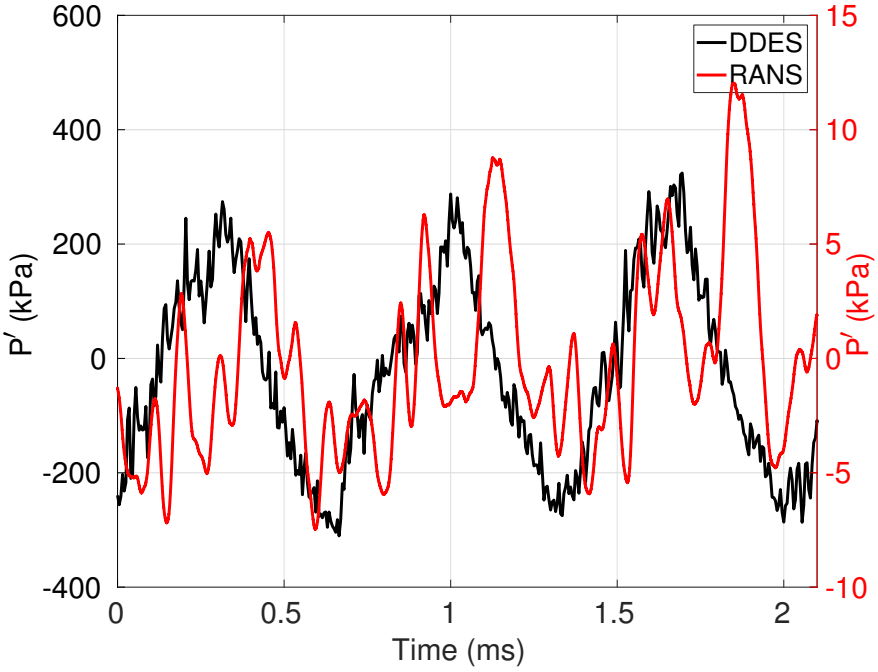

Figure A.2: Pressure signals on the combustion chamber wall at $x = 37\ cm$. The y-axis scales between the two simulations are different.